NAVAL POSTGRADUATE SCHOOL

MONTEREY, CALIFORNIA

THESIS

A SYSTEMATIC CATHODE STUDY—ACTIVATION OF A THERMIONIC CATHODE, AND MEASURING CESIUM EVAPORATION FROM A DISPENSER PHOTOCATHODE

by

Justin Jimenez

June 2010

Thesis Co-Advisors:	John W. Lewellen John R. Harris

Approved for public release; distribution is unlimited

THIS PAGE INTENTIONALLY LEFT BLANK

REPORT DOCUMENTATION PAGE	*Form Approved OMB No. 0704-0188*

Public reporting burden for this collection of information is estimated to average 1 hour per response, including the time for reviewing instruction, searching existing data sources, gathering and maintaining the data needed, and completing and reviewing the collection of information. Send comments regarding this burden estimate or any other aspect of this collection of information, including suggestions for reducing this burden, to Washington headquarters Services, Directorate for Information Operations and Reports, 1215 Jefferson Davis Highway, Suite 1204, Arlington, VA 22202-4302, and to the Office of Management and Budget, Paperwork Reduction Project (0704-0188) Washington DC 20503.

1. AGENCY USE ONLY *(Leave blank)*	**2. REPORT DATE** June 2010	**3. REPORT TYPE AND DATES COVERED** Master's Thesis

4. TITLE AND SUBTITLE A Systematic Cathode Study—Activation of a Thermionic Cathode, and Measuring Cesium Evaporation from a Dispenser Photocathode	**5. FUNDING NUMBERS**
6. AUTHOR(S) Justin C. Jimenez	
7. PERFORMING ORGANIZATION NAME(S) AND ADDRESS(ES) Naval Postgraduate School Monterey, CA 93943-5000	**8. PERFORMING ORGANIZATION REPORT NUMBER**
9. SPONSORING /MONITORING AGENCY NAME(S) AND ADDRESS(ES) N/A	**10. SPONSORING/MONITORING AGENCY REPORT NUMBER**

11. SUPPLEMENTARY NOTES The views expressed in this thesis are those of the author and do not reflect the official policy or position of the Department of Defense or the U.S. Government. IRB Protocol number____________

12a. DISTRIBUTION / AVAILABILITY STATEMENT Approved for public release; distribution is unlimited	**12b. DISTRIBUTION CODE**

13. ABSTRACT (maximum 200 words)

The Free Electron Laser (FEL) is one of the Navy's 'future weapons' undergoing research and testing for implementation on naval vessels. The Naval Postgraduate School is joining in the Navy's Free Electron Laser effort by constructing a scaled-down version of the naval system—the NPS FEL. Our first research goal is to better understand the current thermionic cathode used in the NPS FEL system, the Eimac Y-845. This thesis will explore the outgassing of these cathodes as well as chart heater filament voltage vs. temperature, an important factor for understanding the operational regime the cathode will be in (primarily photoemission, or thermionic, or both).

Additionally, we aim to examine a new type of Cesium Reservoir Dispenser Photocathode currently being built by the University of Maryland. Dispenser photocathodes are a promising technology in that they may have much longer lifetimes than other types of high quantum efficiency photocathodes. The concern with this new style of cathode relates to cesium release into the photoinjector cavity. We aim to ascertain the rates of cesium emission that users may encounter when utilizing these cathodes. This data will help determine if operational cesium dispenser photocathodes have low enough cesium emission for in-gun testing and use.

14. SUBJECT TERMS Free Electron Laser, Thermionic, Dispenser, Cathode, Outgassing, Cessium evaporation	**15. NUMBER OF PAGES** 145
	16. PRICE CODE

17. SECURITY CLASSIFICATION OF REPORT Unclassified	**18. SECURITY CLASSIFICATION OF THIS PAGE** Unclassified	**19. SECURITY CLASSIFICATION OF ABSTRACT** Unclassified	**20. LIMITATION OF ABSTRACT** UU

NSN 7540-01-280-5500

Standard Form 298 (Rev. 2-89)
Prescribed by ANSI Std. 239-18

THIS PAGE INTENTIONALLY LEFT BLANK

Approved for public release; distribution is unlimited

A SYSTEMATIC CATHODE STUDY—ACTIVATION OF A THERMIONIC CATHODE, AND MEASURING CESIUM EVAPORATION FROM A DISPENSER PHOTOCATHODE

Justin C. Jimenez
Lieutenant, United States Navy
B.S., United States Naval Academy, 2004

Submitted in partial fulfillment of the
requirements for the degree of

MASTER OF SCIENCE IN APPLIED PHYSICS

from the

NAVAL POSTGRADUATE SCHOOL
June 2010

Author: Justin C. Jimenez

Approved by: John W. Lewellen, PhD
Thesis Co-Advisor

John R. Harris, PhD
Thesis Co-Advisor

Andres Larraza
Chairman, Department of Physics

THIS PAGE INTENTIONALLY LEFT BLANK

ABSTRACT

The Free Electron Laser (FEL) is one of the Navy’s ‘future weapons’ undergoing research and testing for implementation on naval vessels. The Naval Postgraduate School is joining in the Navy's Free Electron Laser effort by constructing a scaled-down version of the naval system—the NPS FEL. Our first research goal is to better understand the current thermionic cathode used in the NPS FEL system, the Eimac Y-845. This thesis will explore the outgassing of these cathodes as well as chart heater filament voltage vs. temperature, an important factor for understanding the operational regime the cathode will be in (primarily photoemission, or thermionic, or both).

Additionally, we aim to examine a new type of Cesium Reservoir Dispenser Photocathode currently being built by the University of Maryland. Dispenser photocathodes are a promising technology in that they may have much longer lifetimes than other types of high quantum efficiency photocathodes. The concern with this new style of cathode relates to cesium release into the photoinjector cavity. We aim to ascertain the rates of cesium emission that users may encounter when utilizing these cathodes. This data will help determine if operational cesium dispenser photocathodes have low enough cesium emission for in-gun testing and use.

THIS PAGE INTENTIONALLY LEFT BLANK

TABLE OF CONTENTS

THIS PAGE INTENTIONALLY LEFT BLANK

LIST OF FIGURES

LIST OF TABLES

THIS PAGE INTENTIONALLY LEFT BLANK

LIST OF ABBREVIATIONS AND SYMBOLS

AMU	Atomic Mass Unit
Å	Ångstrom (10^{-10} m)
BAG	Bayard-Alpert Gauge
Bi	Bismuth
CCG	Cold Cathode Gauge
conflat	The standard UHV flange-to-flange interface
CPI	Communications and Power Industry, Incorporated
Cs	Cesium
E_F	Fermi Energy
EDS	Energy Dispersive X-Ray Spectroscopy
FEL	Free Electron Laser
IG	Ion Gauge
INP	Innovative Naval Prototype
IP	Ion Pump
LINAC	Linear Accelerator
eV	electron Volt
l	mean free path
m	meter
mm	millimeter (10^{-3} meters)
nC	nano-Coulomb (10^{-9} Coulombs)
NPS	Naval Postgraduate School
OFHC	Oxygen Free High Thermal Conductivity
ONR	Office of Naval Research
μg	microgram (10^{-6} grams)
Ω	Ohm
	Work Function
PVD	Physical Vapor Deposition
RF	Radio Frequency
RGA	Residual Gas Analyzer

QCM	Quartz Crystal Deposition Monitor
SEM	Scanning Electron Microscope
SRF	Superconducting Radio Frequency
T	Torr
Ti	Titanium
UHV	Ultra High Vacuum ($<10^{-7}$ Torr)
UM	University of Maryland
QCM	Quartz Crystal Deposition Monitor
V	Volt
VAC	Voltage-Alternating Current

ACKNOWLEDGMENTS

I would first like to thank Jennifer, my patient and grace-filled wife, who endured many a lonesome evening while I hid in the experimental dungeon of SP-044. Additionally, I thank my professors for constantly reassuring me that it is okay to spend money when conducting research.

THIS PAGE INTENTIONALLY LEFT BLANK

I. OVERVIEW OF THE FREE ELECTRON LASER

A. FREE ELECTRON LASER ORIGINS

It seems fitting to explain the origins and development of the Free Electron Laser (FEL) before discussing the details of such. This device operates on the principle that an accelerating charged particle will emit electromagnetic waves [1]. Radar, which was an established technology since the First World War, is a basic example of this principle in operation. The first visual observation of electrons (accelerated by a magnetic field) producing light occurred in 1947 by General Electric engineers working with a 70MeV synchrotron [2]. In the 1950s, H. Motz successfully engineered an experiment where he produced millimeter wavelength radiation by passing electrons through a series of magnets with alternating polarities. He later produced visible, but incoherent, light using a more powerful system. A laser, by definition, emits coherent light, and so this device was technically not a laser. In 1977, John Madey of Stanford University hurdled the theoretical and experimental obstacles in order to demonstrate the first true free electron laser [3]. Since that time, FELs have matured as a technology, providing radiation spanning the electromagnetic spectrum (from infrared to hard x-ray) to researchers around the world [4].

B. FREE ELECTRON LASER COMPONENTS

FELs fall into one of two categories based upon their design: oscillator or amplifier. As seen in Figure 1, the two designs share many of the same components. The following subsections discuss the various components of the FEL and reference this figure.

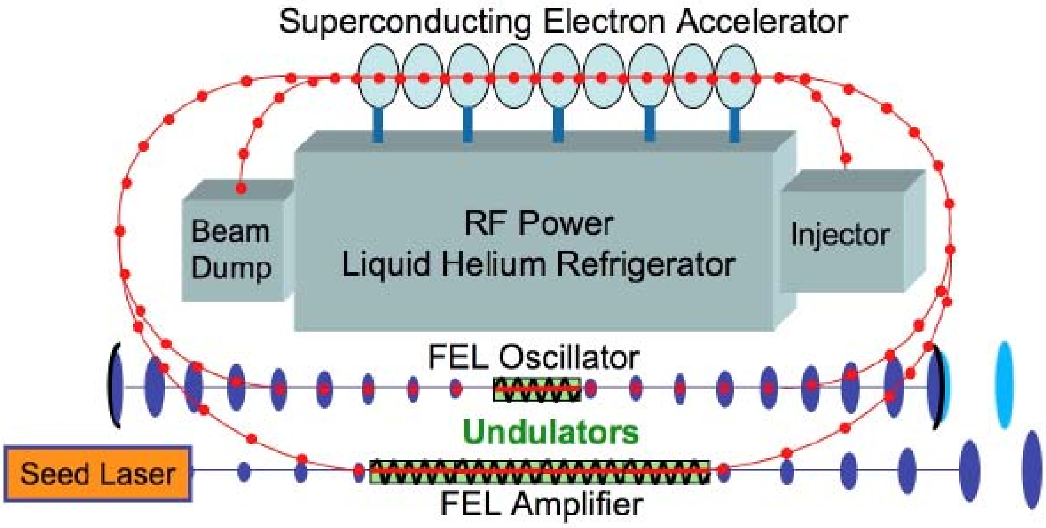

Figure 1. Basic Free Electron Laser (From: [5])

The difference between the two designs depends on the manner in which the optical beam is generated. FEL oscillators use an optical resonator cavity where the optical beam pulses couple to, and are magnified by, the electron beam in order to generate the laser output. FEL amplifiers use an optical pulse generated by a seed laser coupling to the electron beam in order to generate its laser output. A subtype of the FEL amplifier is the Self-Amplified Stimulated Emission (SASE) FEL that creates its own seed light from noise in the individual electron bunches as they pass through the undulator.

1. Injector

The injector is truly the beginning of all things in FELs. The electron beam is produced at a cathode buried within the injector, and the manner in which that is done dictates many performance factors of the laser. No matter how the electrons are produced, the bottom line in FEL operation is that the electron beam quality (emittance) will never get better than what it is at the injector.

2. Accelerator

The accelerator serves two roles. First, it takes the electron beam from the injector and boosts the energy to high levels. The proposed Navy FEL will have an injector that supplies ~5MeV electrons that the accelerator will then boost to 100MeV. Second, some FELs use the accelerator to decelerate the electron beam after it has passed through the undulator—this process is known as ‘energy recovery.’

The ‘generic’ FEL shown in Figure 1 is designed with a superconducting accelerator structure that also performs energy recovery. Most current FELs have neither superconducting accelerators nor the cryogenic systems that accompany such [4].

3. Undulator

Undulators, also known as “wigglers,” are strings of magnets that bend the electron beam back and forth in order to cause lateral acceleration and thusly radiation. This principle is demonstrated in Figure 2.

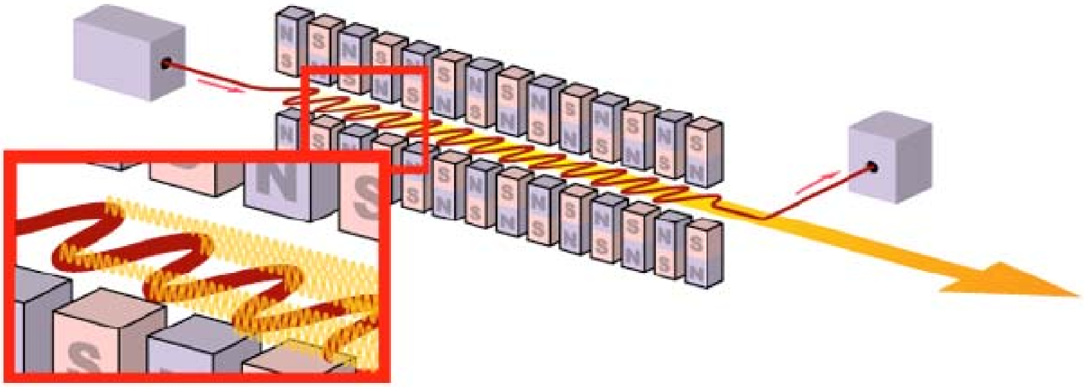

Figure 2. FEL Injector, Wiggler, and Beam Dump (From: [6])

4. Optical Resonator

Not all FELs have optical resonator cavities—FEL amplifiers (and the subset SASE systems)—do away with this component. That being said, the majority of operating FELs around the world are oscillator FELS, meaning that they have resonators [4]. The resonator cavity is, in principle, the same as for any other laser. The light generated by the electrons bounces back and forth between two mirrors, amplifying in intensity as each electron bunch passes through. Additionally, as the light from each bunch bounces between the mirrors it couples to later electron bunches, providing a feedback mechanism that leads to coherent radiation—the essence of a laser. One of the attractive qualities of the FEL is that the resonator cavity is a void space held at vacuum. Other lasers have a physical medium of some sort within the resonator cavity that can complicate matters when it comes to heat dissipation, especially at high powers.

5. Beam Dump

Seen in both Figures 1 and 2, the beam dump is the ‘catcher’s mitt’ for spent electrons. After the electron beam passes through the undulator, it still contains a significant amount of energy. If improperly directed, this energy can easily strike internal components of the FEL causing catastrophic system damage and excess radiation. The beam dump is specially designed to absorb the remaining beam energy in a safe and controlled fashion.

C. MOTIVATION FOR NAVAL FREE ELECTRON LASER RESEARCH

1. The Initial Driver

What does the U.S. Navy want with a Free Electron Laser? As stated by the Office of Naval Research (ONR):

> The capability of having speed-of-light delivery for a wide range of missions and threats is a key element of future shipboard layered defense… This revolutionary technology allows for multiple payoffs for the warfighter. The ability to control the strength of the beam provides for graduated lethality, and the use of light vice an explosive munition, provides for lower per-engagement and life cycle costs. Not worrying about propulsion and working at the speed of light allows for precise engagement and the resulting low collateral damage. Speed-of-light engagement also allows for a rapid reaction to moving and/or swarming time critical targets. [7]

The Naval Postgraduate School has conducted FEL research since 1989 [8]. Recently, the group constructed a research facility at the nearby Navy golf course to support hands-on FEL research pertaining to the Innovative Naval Prototype (INP) effort that started in FY2010. While NPS is not planning on housing a weapons-class Free Electron Laser, we hope to contribute by researching specific topics of interest that will impact the INP development effort.

2. Cathode Research in Support of the NPS FEL

The research contained in this thesis consists of two separate investigations. The first experimental foray focused on the Eimac Y-845 thermionic cathode (Figure 3), as this is the cathode currently in the injector of the NPS FEL beamline. The factors examined in this body of work pertain to the physical hurdles of preparing a cathode for operation (activation) and cleaning a cathode after being contaminated (processing).


Eimac Y-845 Thermionic Cathode by SpectraMat Inc.

Experimental Dispenser Photocathode by the University of Maryland

Figure 3. The two cathode types examined in this work

The second journey takes us into the world of photocathodes. Researchers at the University of Maryland have developed a new style of photocathode seen at right in Figure 3. The photocathode pictured here was an early prototype and not an actual test sample for our work. We set about examining aspects of the cathode's physical performance. The results of these tests would help determine whether these cathodes are a safe and practical technology for photo-driven FEL systems.

II. CATHODES—THE BEGINNING OF ALL THINGS

A. CATHODE TYPES

Every free electron laser requires a source of free electrons. By “free,” we mean electrons that have been loosed from their binding affinity with atoms. Cathodes are the devices designed to produce said electrons. In general, it can be said that the quality of a FEL depends upon the quality of the electron beam, and this in turn depends upon the quality of the cathode. Cathodes may produce electrons in any of the following manners:

- Field emission
- Thermionic emission
- Secondary emission
- Photoelectric emission

No matter which type of cathode we talk about, sufficient energy must be imparted to the individual electrons in order to allow them to escape the forces that bind them within the cathode. The different cathode types only differ in how that escape energy is transferred to the free electrons. Field emission cathodes emit electrons by concentrating strong electric fields onto a point, or points. Thermionic emission occurs when the cathode is heated enough such that electrons gain sufficient thermal energy to escape. Secondary emission occurs when high-energy electrons impact the material with sufficient energy to ‘knock’ several other electrons out of the material. Photoelectric emission occurs when photons of sufficient energy impact the cathode and transfer their energy to electrons.

The research presented in this paper concerns itself with two specific cathodes—the EIMAC Y-845 thermionic cathode and the (experimental) University of Maryland dispenser photocathode. We shall develop a few elements of basic cathode theory before discussing the particulars of each experiment.

B. THE TIE THAT BINDS—THE WORK FUNCTION

Though the physical mechanisms used to create electron emission differ between thermionic cathodes and photocathodes, one physical quantity similarly affects the performance of both cathodes—the work function ( ).

The work function is the required amount of energy an electron must gain in order to escape the atomic forces that otherwise hold it in the material of interest. One can think of it as the energy needed for the electron to achieve ‘escape velocity’, and the normal units used to express ϕ are electron-Volts (eV).

C. PHOTOEMISSION THEORY

Experiments carried out circa 1900 demonstrated the stimulated emission of photons from metal when visible or ultraviolet light fell incident on the plate. Experimenters dubbed this phenomenon the photoelectric effect. The essential lessons learned from these experiments are summarized as follows [9]:

1. The electron’s kinetic energy is independent of the incident light’s intensity.
2. The maximum kinetic energy of the generated electrons depends only upon the frequency of the light.
3. The smaller the work function, ϕ, the lower the threshold frequency required to generate photoelectrons. No electrons were generated below this frequency regardless of the light’s intensity.

This discovery had profound implications for quantum physicists, but our interests lay with the applicability of photoemission to Free Electron Lasers. Figure 4 demonstrates photoemission with two different diagrams. The left schematic in the figure shows an energy diagram of the material of choice—tungsten. At a cooled state, the majority of the electron population lives below the Fermi energy. When a photon (purple dot) of sufficient energy strikes the material, it can generate a free electron by giving it sufficient energy to escape the work function barrier.

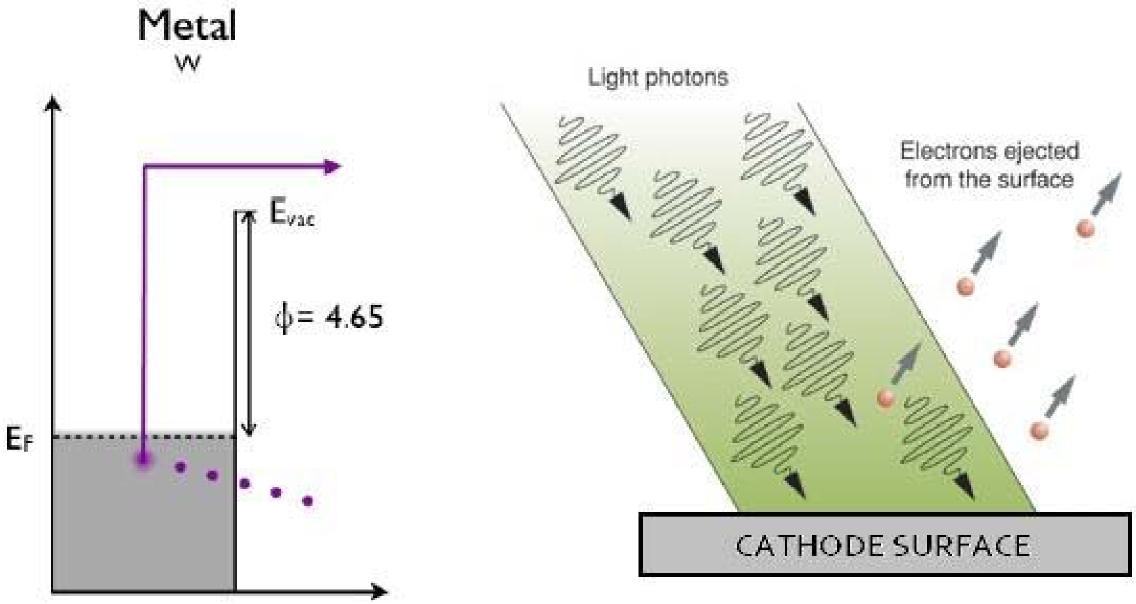

Figure 4. Photoelectric emission from a tungsten cathode surface (From: [10])

The schematic at right in Figure 4 shows a more physically intuitive depiction of this process at work.

D. THERMIONIC EMISSION THEORY

Thermionic emission has, just as it sounds, something to do with temperature. Every solid metal has one or two electrons per atom that are not bound to any particular atom and move freely through the metal in much the same way as free electrons in a vacuum can move. Their energies are not uniform, but rather are governed by a statistical distribution. Every now and then, an electron's kinetic energy will exceed the work function of the material and escape—this effect is enhanced by heating the metal. Thermionic cathodes exploit the benefits of thermal energy to drive electrons off the cathode.

Figure 5 depicts a standard energy diagram of an arbitrary material. The vertical axis depicts the energy of the material's electrons in eV, and the horizontal axis depicts the material depth. The gray column depicts the distribution of electrons at any given energy level. The Fermi energy, $\mathbf{E_F}$, is marked on the vertical axis and signifies the highest energy an electron could have in this material if it were cooled to absolute zero. Since the material is not at absolute zero, the electrons will have excess kinetic energy that allows them to rise above the Fermi energy. This effect is statistically modeled as an electron distribution (the gray bar) due to the large number of electrons in a solid.

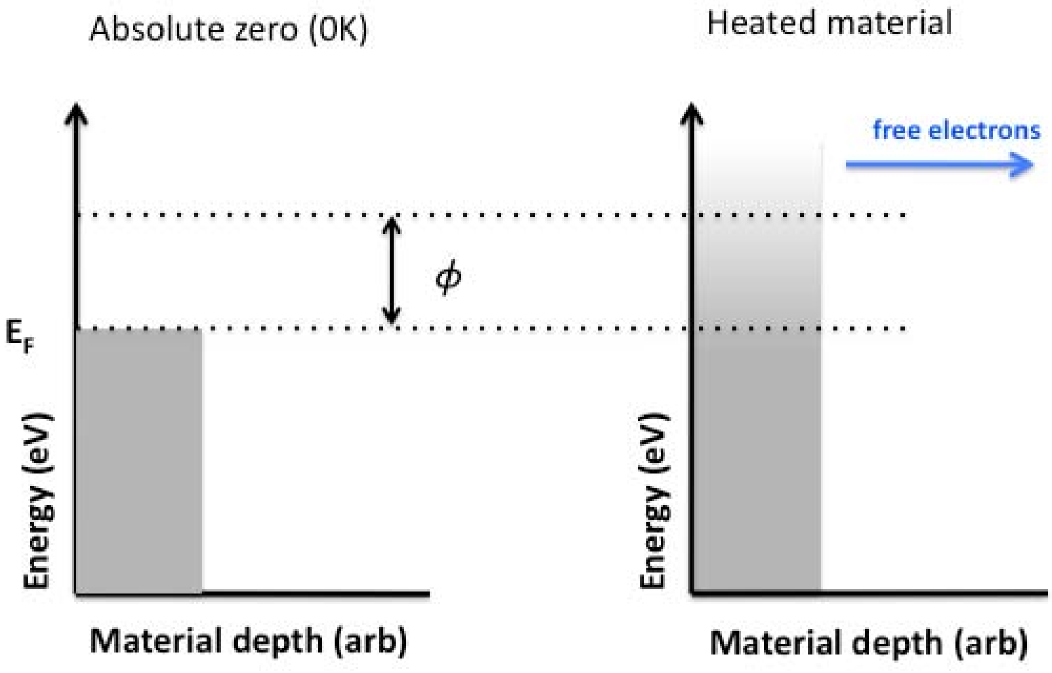

Figure 5. Distribution of electron energies for material at 0 K and for a heated material

As the temperature increases, the distribution of electrons (i.e.—the amount of gray shading) above the Fermi energy increases to a point where electrons start exceeding the work function, ϕ. At this point, they escape the binding forces that hold them in the material and drift away. These 'free' electrons are depicted by the blue arrow at right in Figure 5.

This effect was first noticed by Frederick Gutherie in 1873 (before the official discovery of the electron), and later rediscovered by Thomas Edison in 1880 while working on filaments for his incandescent bulbs [11]. Owen W. Richardson pursued this area of interest, and in 1901 published the following conclusion: the current from a heated wire has an exponential dependence on temperature. He gave the name 'thermionic emission' to this effect and proposed the following equation governing such:

$$J = A_0 T^2 \exp(-\phi/kT) \qquad [1]$$

where J = current density [A/m^2], T = temperature [K], ϕ = material work function, k = Boltzmann's constant, and A_0 = Richardson's constant = 1.20173 x 10^6 [A m^{-2} K^{-2}].

A cursory examination of equation [1] shows a direct dependence on the square of temperature as well as a $-1/T$ dependence in the exponent. What does this look like in practice? Figure 6 shows the stock characterization of a generic tungsten cathode where current density is charted as a function of temperature. As the temperature increases, current density increases at a rate greater than linear.

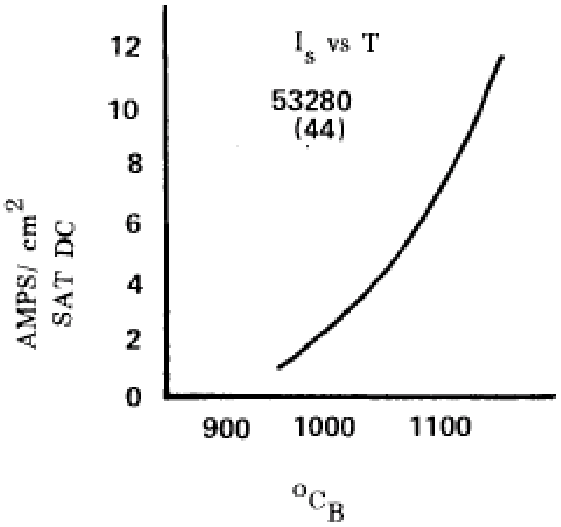

Figure 6. Stock Characterization of Tungsten Thermionic Cathode (From: [12])

The lesson we can draw from this plot is that heat is good, more heat is better, when it comes to thermionic emission. There must, however, be some finite limits to heating a cathode. Obviously, the material itself must be able to withstand the applied heat without deforming, melting, or otherwise evaporating into the vacuum. This inclination towards heat resistant materials makes metal a desirable choice for thermionic cathode construction. Unfortunately, the metals with suitable physical properties for cathode construction usually have high work functions—making them poor electron emitters. Table 1 lists five different metals with their respective work functions in order to illustrate this point.

Metal	Work function, ϕ [Volts]	Melting temp [C]
Cesium	1.8	28.5
Aluminum	3.0	660
Barium	2.5	850
Copper	4.1	1083
Tungsten	4.5	3370

Table 1. List of work functions and melting temps for various metals (From: [13])

Tungsten is the most extensively used metal for thermionic cathodes since it has the highest melting temperature of all metals. Its high work function is offset by the fact that it can be heated hotter than any other metal. Despite having such a high melting temperature, tungsten has several drawbacks. The metal can be difficult to work with, and its crystalline structure makes it difficult to machine. A benefit of this toughness also makes tungsten the most resilient of metals when utilized as an emitter in a high voltage system. When high voltages are applied to emitters, the induced electric field causes ionization of residual gases in the vacuum. The positive ions generated slam into the cathode surface and, over time, will damage it. Tungsten is more suited to withstanding this positive-ion bombardment than any other metal. Additionally, cathodes are subject to reduced emission from contamination by various gases. Tungsten cleans up more readily by heating or bombardment than any other metal. These benefits will be made clearer in Chapter III ,where we will discuss mechanisms of cathode damage [13].

E. CATHODE DESIGN

1. Work Function Enhancement

One way to improve the operating efficiency of a cathode is by reducing the energy required for individual electrons to escape the cathode surface. This practice is otherwise known as ‘work-function enhancement.’

An item of interest for the Navy FEL in particular, and FEL physics in general, is how to reduce the work function of a cathode in order to generate more electrons. The Naval FEL will require a cathode that can source a 1-amp average current. Additionally, the cathode must be able to produce electron bunches with picosecond response times [14]. This design requirement for a high-current, high-quality electron source exceeds the current state of the technology. Achieving this design goal is essential in the Navy’s pursuit of a weapons-class FEL. Enhancement of cathode work function is avenue of progress towards this goal.

In the early 1930s, Irving Langmuir and John Rogers realized that work functions could be modified through a happy experimental accident. In heated-filament experiments, they found that one could get higher emission than that from a pure metal by depositing an atomic film of a metal with a lower work function over the original material. This discovery was not a planned event. The two originally had problems with their tungsten filaments crystallizing and breaking. Being experimentalists, they added thorium in an effort to reduce this crystallization behavior. These new thoriated-tungsten filaments exhibited very high emission when compared with pure tungsten filaments:

> What apparently happens is that a certain amount of thorium in the metal diffuses to the surface, where it emits much as thorium would, with the advantage that the thorium can be heated above its own melting temperature and that the work function is reduced by the redistribution of charges in the tungsten and surface layer of thorium. [13]

To further illustrate this phenomenon, Langmuir and Rogers charted cathode emission versus percent thorium coverage, as seen in Figure 7.

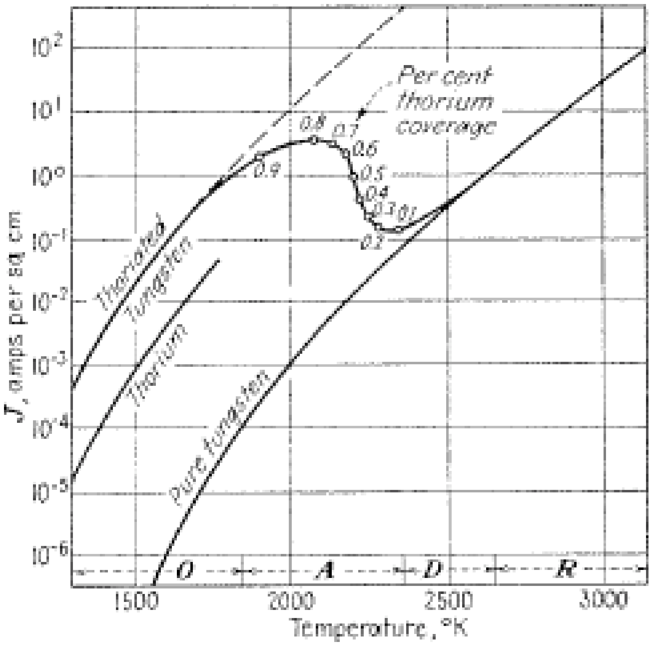

Figure 7. Effects of coating a tungsten cathode with thorium (From: [13])

The horizontal axis shows the cathode temperature and the vertical axis shows current density for three different scenarios: a pure tungsten emitter, pure thorium, and a thorium-coated tungsten emitter. Current densities for the tungsten and thoriated tungsten filament are recorded from sub-1500K to past 3000K. The data for thorium stops at approximately 1750K. This is possibly due to the fact that thorium melts at 2115K, and filaments would be prone to failure several hundred degrees below this point. Regardless, Langmuir and Rogers were surprised to find when they distributed thorium as a monolayer coating on a tungsten surface it bonded with the tungsten thus reducing the evaporation rate by orders of magnitude. This effect allowed hundreds to thousands of hours of operation before the efficiency dropped. Additionally, and perhaps surprisingly, the efficiency of the cathode was greatest at 80% thorium coverage and not 100% coverage. Much research has gone into understanding the theoretical mechanism behind this behavior. One main current of thought is that the low ϕ material bonds to the cathode surface in such a way as to set up a dipole effect, creating ‘bumps’ on the atomic level from which electrons can escape easier than from the cathode surface itself [15].

Additional research by others has shown that thorium is not the only metal that can improve the efficiency of tungsten cathodes. Some other materials used in this manner are osmium, calcium, barium oxide, iridium, and ruthenium—to name a few [19].

2. The Modern Dispenser Thermionic Cathode Is Born

Early cathode designers wanted to take advantage of the work-function lowering properties of other materials by coating tungsten cathodes, but the low-ϕ coating would eventually evaporate—reducing the cathode efficiency. Cathode engineers had to figure out a way to design a cathode such that the low-ϕ material would replenish itself, thus extending the cathode's useful life. Over the years several mechanisms have been used that dispense low-ϕ material onto the cathode surface—these cathodes are subsequently classified as 'dispenser' cathodes.

The panoply of modern thermionic dispenser cathodes all trace their roots back to nickel-based cathodes sprayed with an oxide layer of (Ba Sr) CO_3. The first stage of development consisted of changing the oxide coating to an oxide-bearing cavity behind a porous tungsten plug (circa 1950). These cathodes were difficult to manufacture with consistent performance and were finicky in use. In late 1951, Hughes, Coppola, and Rittner, of the North American Philips Company in New York, found that tungsten powder mixed with barium aluminate could be pressed into cathodes and performed markedly better than all previous designs. Over the years, different researchers around the world would refine and expand the various chemical recipes that went into pressed tungsten cathodes. Not all these efforts were the result of insightful application of theory—some of it was accidental, or sheer guesswork at best—the links between material composition and cathode performance were not always understood. By 1970, the barium scandate cathode became the third major style of dispenser cathode in the industry. It consists of a porous tungsten matrix mixed with either barium scandate ($BaO: 2Sc_2O_3$) or barium calcium aluminum scandate [16].

Figure 8 shows the generic layouts of two popular thermionic dispenser cathodes on the market today. The cathode on the left is an impregnation style cathode. The low-

ϕ material is evenly mixed with tungsten powder and subsequently heated/pressed into its final shape. A heating element behind the cathode body provides the heat necessary for thermionic emission as well as evolving the low-ϕ material to the surface. Since the cathode is formed from a tungsten powder, and is purposely pressed so that it still contains pores throughout its structure, the low-ϕ material (barium oxide in this case) can migrate to the surface. As the low-ϕ material near the surface depletes, it must be replenished by material further inside the cathode structure. This increases the diffusion distance, decreases the diffusion gradient, and slowly diminishes the cathode's efficiency [17], [18].

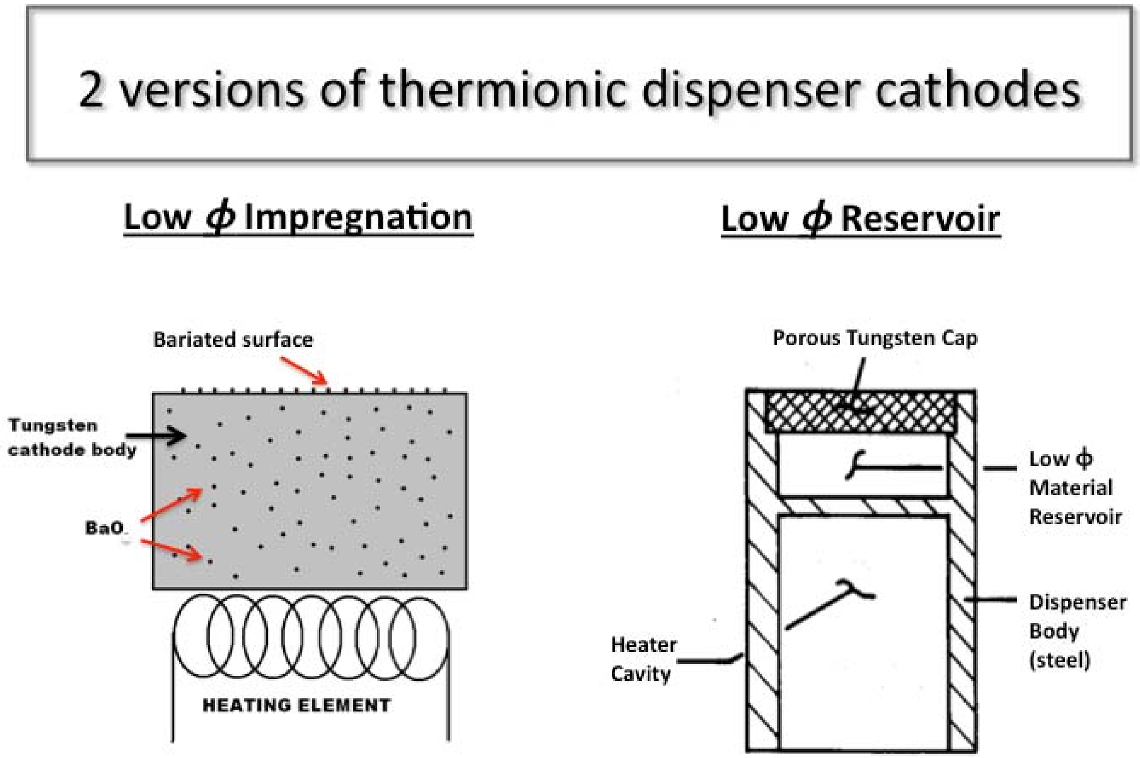

Figure 8. Two forms of dispenser cathodes (right picture modified from: [16])

Much work has gone into fine-tuning how all the physical elements of these dispenser cathodes come together. Some practitioners mix the tungsten and low-ϕ material in powder form, and then press/heat the mixture to form the cathode structure. Others create the tungsten cathode first, and then impregnate it with a low-ϕ compound afterwards. Regardless of which version we talk about, these cathodes provide good emission currents with reasonably low evaporation rates of the low-ϕ material.

The schematic on the right shows a reservoir style dispenser cathode. For the same volume, this style cathode can hold a much higher concentration of low-ϕ material in the reservoir than a similar size impregnation style cathode. The principle of diffusion is similar for this cathode with the exception that the low-ϕ material has a constant distance to diffuse (from reservoir to surface) and can maintain a steadier diffusion gradient. Along with the increased quantity of low-ϕ material, this lends itself to a longer useful lifetime.

3. Cathode Efficiency

a. Thermionic Emitters

The measure of efficiency differs markedly when talking about thermionic cathodes or photocathodes. Measurement of thermionic cathode performance requires a current-voltage characterization—i.e., how much current do I get at a given voltage? The ultimate units of measurement for thermionic cathodes are measures of current-per-area [A/cm^2]. As a gauge of overall performance, sixty years of research and development have produced cathodes capable of sourcing upwards of 16 A/cm^2 [19].

b. Photoemitters

When it comes to photocathodes, quantum efficiency (QE) is measured as the fraction of incident photons that produce a photo-emitted electron:

$$\text{QE} = \frac{\text{Electrons Emitted}}{\text{Photons Incident}} \qquad [2]$$

Surface characteristics, electrical properties, and temperature are a few contributing factors that affect QE. While this work will not directly explore these factors they are worth mentioning.

F. CATHODE ACTIVATION

Let us switch tracks from the theoretical to practical. Most cathodes must undergo a specific series of steps, known as activation or processing, before they are ready for use. Why so? First, regardless of the stringent standards used during the manufacturing process cathodes will inevitably pick up some form of contamination. Second, cathodes have either intentional or unintentional defects due to manufacturing [20]. Third, the sheer act of handling a cathode during shipping and installation can allow contaminants to settle on the surface. Lastly, cathodes such as thermionic dispenser cathodes or field emitter arrays are designed such that a specific sequence of steps necessary for optimal operation cannot be executed prior to final installation in a vacuum environment [21], [22]. For example, the low-ϕ material in many thermionic dispenser cathodes is bound in a molecular compound for ease of handling during the manufacturing process. Heating dissociates these compounds, thus releasing the low-ϕ material. This paper will use the term ‘activation’ when referring to the first time a cathode undergoes the specific steps requisite to prepare it for operation.

In addition to activation, some cathodes can also be reprocessed/rejuvenated if contamination or other physical effects have diminished its performance. The steps for cathode rejuvenation are generally similar (or identical) to the steps required for initial activation. In this case, we will refer to the process as ‘reprocessing’ or ‘rejuvenation.’

III. KEEPING A CLEAN HOUSE—HOW CATHODES AND ENTIRE FEL SYSTEMS DIE

A. THERMIONIC CATHODE LIFETIME VERSUS TEMPERATURE

For thermionic cathodes, the operating temperature is the main controllable factor that affects lifetime. SpectraMat Inc. has published a general performance characterization for thermionic dispenser cathodes as seen in Figure 9. The graph on the left shows current density as a function of temperature. The figure on the right shows cathode lifetime versus temperature—note the vertical logarithmic scale.

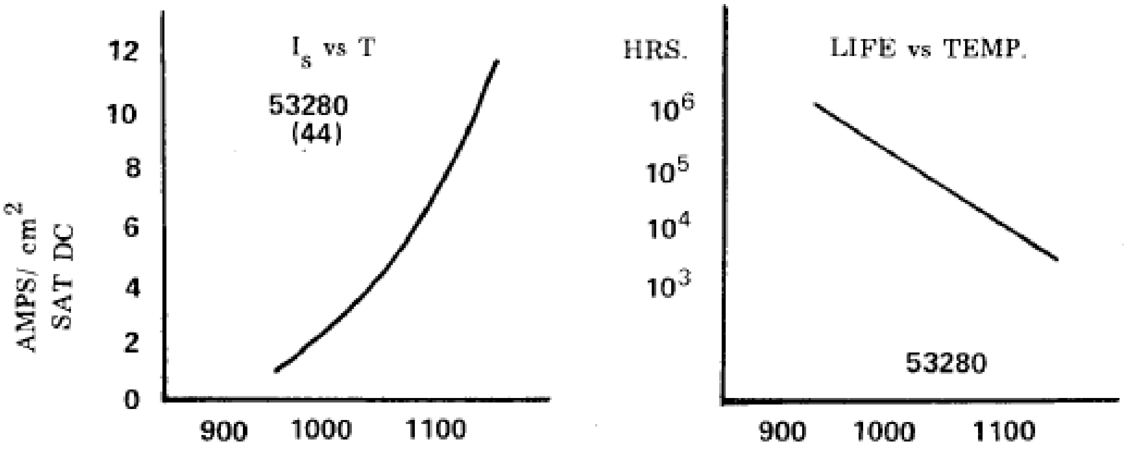

Figure 9. Generic Thermionic Dispenser Cathode Characterization (From: [12])

So the writing is on the wall—if we operate a cathode in order to provide a high current density we will significantly drive down its useful lifetime. While cathodes can be replaced, the process takes time and manpower. Ultimately, the decision as to how hard a cathode is driven is as much an operations and management issue as it is an engineering issue.

B. 31 FLAVORS—LIFETIMES OF VARIOUS PHOTOCATHODES

Photocathodes come in a variety of flavors from metals to semiconductors. Figure 10 shows one data set correlating useful lifetime with efficiency for a number of cathodes. Lifetime is scaled logarithmically on the horizontal axis. Quantum efficiency is charted logarithmically on the vertical axis for two different wavelengths of light—the physics of which is not of concern to the present work.

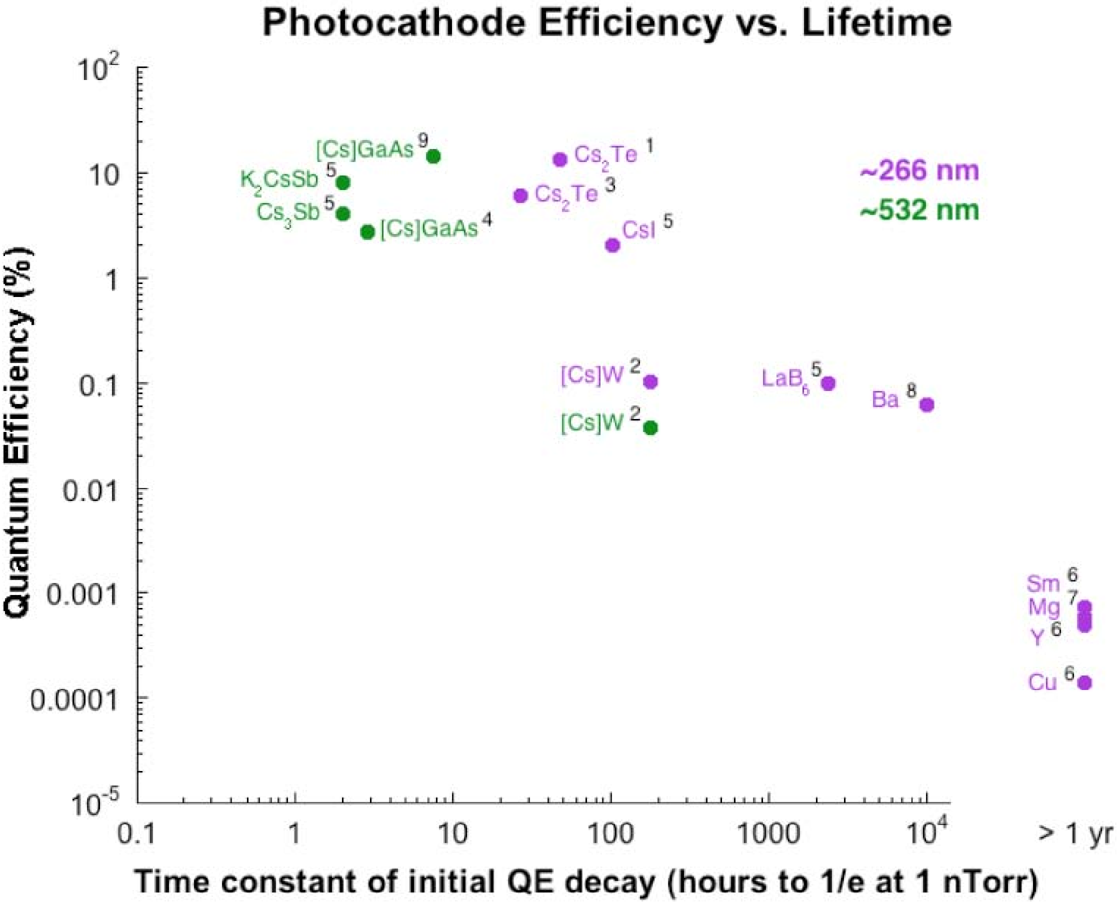

Figure 10. Cathode quantum efficiency versus lifetime (From: [20])

In general, solid metal cathodes are robust and have lifetimes in the 1000s of hours, as seen in at far right in Figure 10 [23]. The drawback to metal cathodes is, as seen from the chart, that they generally have a very low QE (when operated as a photocathode). Semiconductor cathodes and monolayer-coated cathodes live at the other end of the performance spectrum. They have remarkable QE when compared with metal, but they are sensitive to a variety of physical processes that give them shorter useful lifetimes.

C. CATHODE DEGRADATION

We will discuss two primary means by which cathode performance is degraded—physical damage and poisoning (contamination). We will also discuss how certain components of FEL systems are damaged, and how cathode performance could contribute to this damage.

1. Damage Mechanism #1—Physical Destruction

Perhaps the most obvious way in which a cathode can be rendered unusable is by physical damage. This damage generally occurs via ion bombardment and multipacting. Ion damage occurs when emitted electrons impact, and thus ionize, gas particles near the cathode surface. These ions accelerate towards the negatively biased cathode and strike it—physically damaging the surface. The top part of Figure 11 depicts this process taking place on a generic cathode surface.

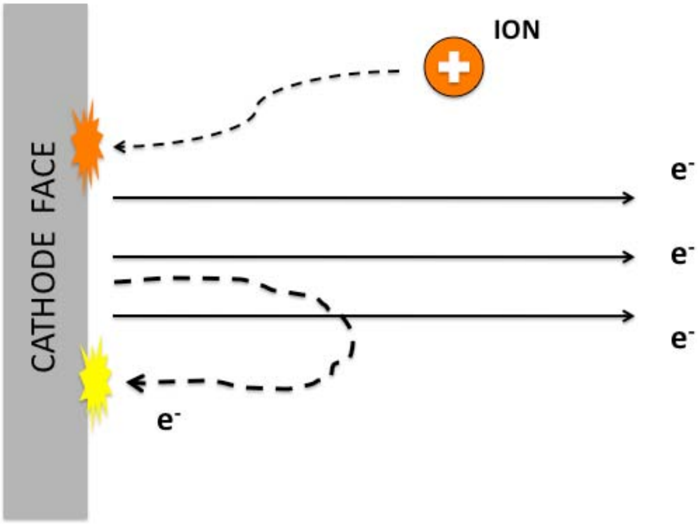

Figure 11. Ion Bombardment and Multipacting

As will be covered in Chapter IV, this is exactly the process by which a residual gas analyzer works (RGA). The important distinction to be made is that this behavior is desirous in an RGA, but not on a cathode surface.

The other damage effect, as seen at bottom in Figure 11 is known as ‘multipacting.’ Multipacting occurs in RF electron injectors when an electron escapes the cathode surface at a moment when the fluctuating RF accelerating field drives it back towards the cathode. If this happens, the electron may strike the cathode with sufficient energy to damage the surface [24].

The extent to which physical damage is a problem depends on the kind of cathode one is concerned with. Solid metal cathodes, being a bulk material, withstand the damage better than cathodes coated with thin films of low-ϕ material. Of all metals, tungsten is the hardest, and thus most resilient to impact damage [13]. Other cathodes may have thin films designed to improve efficiency. These films quickly degrade with repeated ion collisions and cause a drop in cathode performance [25].

The sheer act of particles covering a portion of the cathode surface can also reduce emission. Silicon and carbon are two examples of contaminants that can do such. Vacuum component containing any manner of silicates can shed fine silica particles that could land on, and melt to, a hot cathode surface. Carbon can come in the form of solid particulate contamination generated by another vacuum component, or can arrive via contaminant gases [26][27].

2. Damage Mechanism #2—Chemical Interactions

Cathode damage can also occur through chemical interactions with unwanted contaminants—an effect known as ‘poisoning.’ Cathode poisoning depends on the choice of materials used as well as the composition of residual gases in the vacuum. Poisoning can occur by exposure to various reactive gases such as: oxygen, water vapor, benzene, chlorine, nitric oxide, carbon dioxide, and silicon. Walter H. Kohl’s book, *Handbook of Materials and Techniques for Vacuum Devices*, contains useful information on cathodes and poisoning agents [26][28]. Additionally, Nexsen and Turner have published a paper in the Journal of Applied Physics showing the effects of common residual gases on cathode performance [25]. Their study found that, of common vacuum contaminants, residual water vapor was the most damaging to their osmium-coated thermionic dispenser cathode. Other gases they used to poison the cathode were: oxygen, carbon monoxide, carbon dioxide, Freon, and turbopump oil vapor. All these gases had a detrimental effect with Freon being the worst offender of the group. On the bright side, the research team was able to rejuvenate the cathode after each poisoning, thus demonstrating that cathodes can be rejuvenated even after severe performance degradation.

How exactly do these gases poison a cathode? First, contaminant gases react with surface coatings of various cathodes thereby producing ‘poisons’ that displace the original surface coating and increase the work function of the surface [29]. Second, the thermionic cathode is hot enough to provide the necessary energy required to prompt many chemical reactions. Contaminants that contain oxygen can easily react with the cathode surface in such a way that a high-ϕ oxide layer forms over the cathode surface. Since gaseous oxygen and water vapor are two of the most common contaminants, they are significant contributors to this effect [30].

3. Metal Poisoning Effects

Metals can become vacuum contaminants if their vapor pressure is high enough that they evaporate into the system. Materials that should be avoided either in their entirety or in the vicinity of high heat include silver, alloys such as brass and zinc, and non-OFHC copper [30]. Walter H. Kohl has compiled a great deal of information on vacuum contaminants, and Figure 12 shows two plots taken from his book, Handbook of Materials and Techniques for Vacuum Devices [31]. The left plot shows the vapor pressure of common metals as a function of temperature. Of all the metals shown, zinc is the most prone to cause vacuum contamination—notice its vapor pressure of 1 Torr at approximately 500°C.

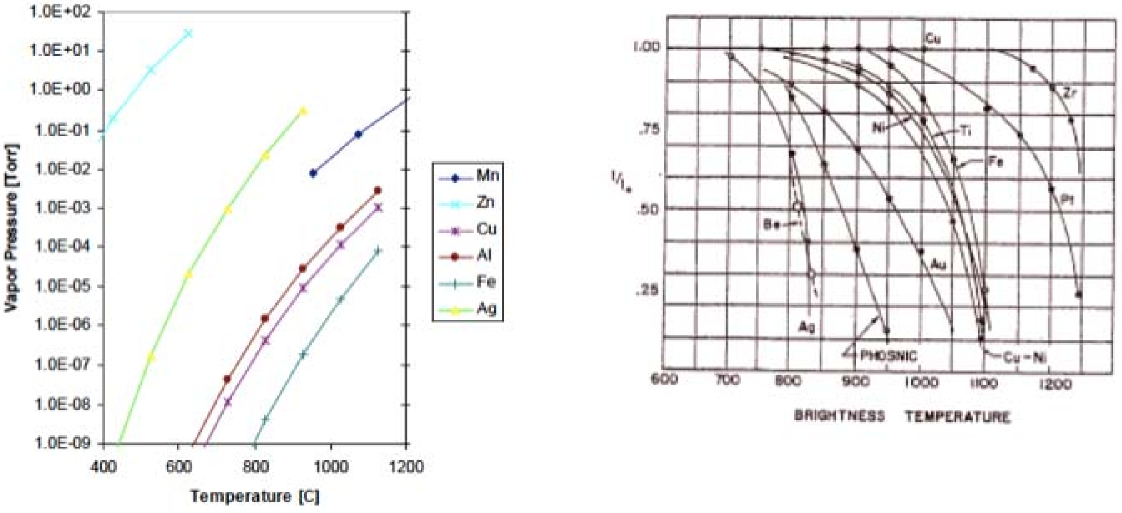

Figure 12. Data on Metal Contaminants (From: [26])

The right plot in Figure 12 shows the fractional dropoff in current from a cathode exposed to various metal contaminants at a range of temperatures from 600–1300°C. Some of these metals are commonly used general hardware such as bolts and washers. As such, care must be taken to use only vacuum approved components when constructing assemblies that will go inside a vacuum system.

4. Poor Vacuum

All contamination effects previously mentioned are either directly or indirectly tied to vacuum pressure. Higher pressures imply higher concentrations of contaminants. As a result, different cathodes will require different levels of vacuum in order to ensure suitable operational lifetimes.

Dispenser cathodes are generally most susceptible to damage caused by poor vacuum during activation or rejuvenation. While specifics may differ from one cathode to another, these processes generally consists of some heating profile that takes the cathode to higher temperatures than required for normal operation. At higher temperatures, the cathode materials can more easily react with vacuum contaminants than at low temperatures. In addition, the thermal activity of the activation/rejuvenation cycle tends to evolve contaminants into the vacuum from the cathode.

If the vacuum is not actively maintained the pressure will rise until the contaminant concentration exceeds acceptable levels. For this reason it is vital to have adequate pumping capacity in the cathode activation chamber, whether that be a dedicated activation chamber or in situ.

5. Moisture

We have already mentioned water vapor as a contaminant, but where does it come from? Sometimes water vapor comes from within the cathode itself. How so? Asking for an impurity free metal would be akin to asking one to assume a spherical chicken—perhaps ideal for a chalkboard, but reality conspires against such ideals.

As discussed in Chapter II, most thermionic cathodes contain performance-altering additives such as aluminum calcite or barium oxide. These impurities either directly or indirectly bring water molecules to the party, generally in the form of hydroxide groups. In layman's terms a hydroxide (hydrated water) is formed when water molecules take up residence in the housing structure of a crystal lattice—molecular squatters in a sense. More formally, a hydroxide is a compound with H_2O molecules loosely associated with it. The water molecules are not part of the molecular formula, and as such the compound is not altered greatly by the removal of said molecules [32]. The danger of blindly heating a cathode hotter than Hades is that each water molecule will do battle against the constraining forces of the surrounding metal. If the reader is an experienced camper they would recognize a parallel application to building campfire rings—one is advised to never make a campfire ring out of river rocks since the rapid heating can cause vaporization of hidden water pockets leading to a violent explosion. In the end the water will win while the cathode (and the researcher) loose.

According to Spectra-Mat, the manufacturer of cathodes & related components, the following statement applies to the current conversation:

> Moisture has the potential of permanently poisoning the cathode. If a cathode is ramped up in temperature at such a rate that the moisture cannot escape, hydroxides…can form which not only reduce emission capabilities but may cause blistering and cracking of the tungsten emitter surface. To prevent this, a cathode must be allowed to [sit] at two temperatures long

> enough to allow complete out-gassing of the hydrated water…this low (400°C) temperature soak is especially important if the cathode has been exposed to air or humidity for an extended period. [33]

D. WHEN GOOD CATHODES GO BAD—ADVERSE EFFECTS ON OTHER FEL COMPONENTS

The Free Electron Laser's safe and efficient operation is contingent upon maintaining a clean system and ultra high vacuums on the order of 10^{-10} Torr [34]. The RF accelerator is the component of concern driving the present research. RF accelerators operate with high electrical field gradients of order magnitude 10MeV/m. Point contaminants pose a significant risk to these accelerator structures because they can act as field emitters (current sources) thereby increasing the heat load at that point. Area contaminants, such as atomic films of unwanted material, can increase resistance for major portions of the accelerator cavity leading to significant overall losses in performance [35]. It is for this reason that manufacturers of RF cavities use chemical etching, electropolishing, and high-pressure water rinses to prepare cavities for operation [36][37][38]. The heating effects mentioned here are all the more serious when dealing with superconducting RF structures. Contaminants such as metal particles and dust on the sub-micrometer size can cause local or general cavity heating leading to a loss of superconductivity [35]. For example, it only takes a 0.5 cm^2 patch of normal-conducting material to degrade the performance of a generic superconducting niobium cavity by over tenfold [39].

Unfortunately, because superconducting technology is a newer aspect in the realm of FEL system design there are many unknowns with regards to their operation. Contamination effects are one area deserving of future research, and an area of interest to the NPS FEL group.

The consequences of system contamination as described above drive our interest in anything that compromises the vacuum in a FEL. So why are we interested in dispenser cathodes when necessarily by definition they dispense material?

First, the basic law of entropy is always working to destroy a vacuum via leaks, outgassing, and evaporation/sublimation processes. In order to maintain a vacuum, the system must be actively pumped. Depending on the pumping mechanism(s) employed, a vacuum can tolerate a certain contamination rate without being otherwise adversely affected. Second, the operation of a FEL system, as any other complex system, is dictated by a cost-benefit matrix that must account for far more variables than the performance of one component. The intent of this paper is not to explore such complexities, but at least acknowledge their existence in order to understand why a facility would choose to use a cathode prone to evolving certain levels of contamination.

In the end, the market speaks for itself. Thermionic dispenser cathodes have been used in various high-end applications for decades, showing that systems can handle certain rates of contamination if properly designed [16][12]. In order to ascertain the viability of the UM dispenser photocathode, we will attempt to quantify its proneness to cesium evaporation. The data collected will help determine if and how processes and system components should be constructed in order to counter any detrimental effects of contamination. We next turn our attention to an experimental investigation of a commercially available thermionic dispenser cathode before returning to the UM dispenser photocathode.

THIS PAGE INTENTIONALLY LEFT BLANK

IV. THE EIMAC CATHODE CAVALCADE

A. EXPERIMENTAL MOTIVATION

The cathode currently used by the NPS FEL group is an Eimac Y-845 thermionic dispenser cathode (Figure 13) manufactured by Communications & Power Industries, Incorporated (CPI). Before extensively using these cathodes in the NPS FEL accelerator structure, we want to gain an understanding of how they behave during the initial activation process as well as during normal operation.

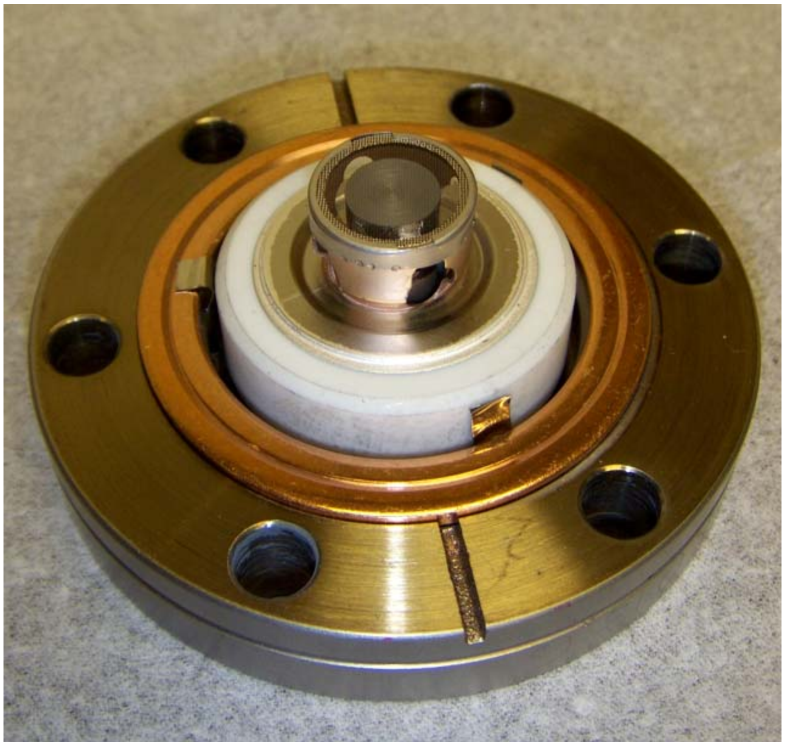

Figure 13. EIMAC Y-845 thermionic dispenser cathode

Specifically, we are interested in the kinds of contaminants that outgas from the cathode as it is prepared for operation via the procedure outlined in Chapter IV, C. Secondarily, we want to chart the heating characteristics of the cathode (power vs. temperature). Seeing as this is a thermionic emitter, it behooves the user to know precisely what temperature their cathode is operating at so that its overall performance can be better gauged. To that end, we constructed a test stand where we could monitor the outgassing of the cathode as well as measure its temperature at various points within its operational range.

We had two Y-845 cathodes available for this test. The first cathode was acquired from Stanford and used in their old LINAC program. Its previous history was unknown, and we used it as a sacrificial sample as we refined our experimental processes. The second cathode was new Y-845 acquired from CPI and would be the main focus of this test.

B. EXPERIMENTAL COMPONENTS AND SETUP

Figure 14 shows the relative orientation of the experimental components in the Eimac Y-845 test stand. The main body of the test chamber consisted of series of three 4-way 2 ¾” conflat crosses onto which the following components were mounted:

a. Eimac Y-845 Thermionic Dispenser Cathode
b. Stanford Research Systems Residual Gas Analyzer (RGA-100)
c. Cold Cathode Gauge (CCG)
d. Hot Cathode Gauge (HCG)
e. 2 Gate Valves (along the main trunk of the test stand)
f. Ion Pump
g. Viewport & Optical Pyrometer
h. Pumping Port

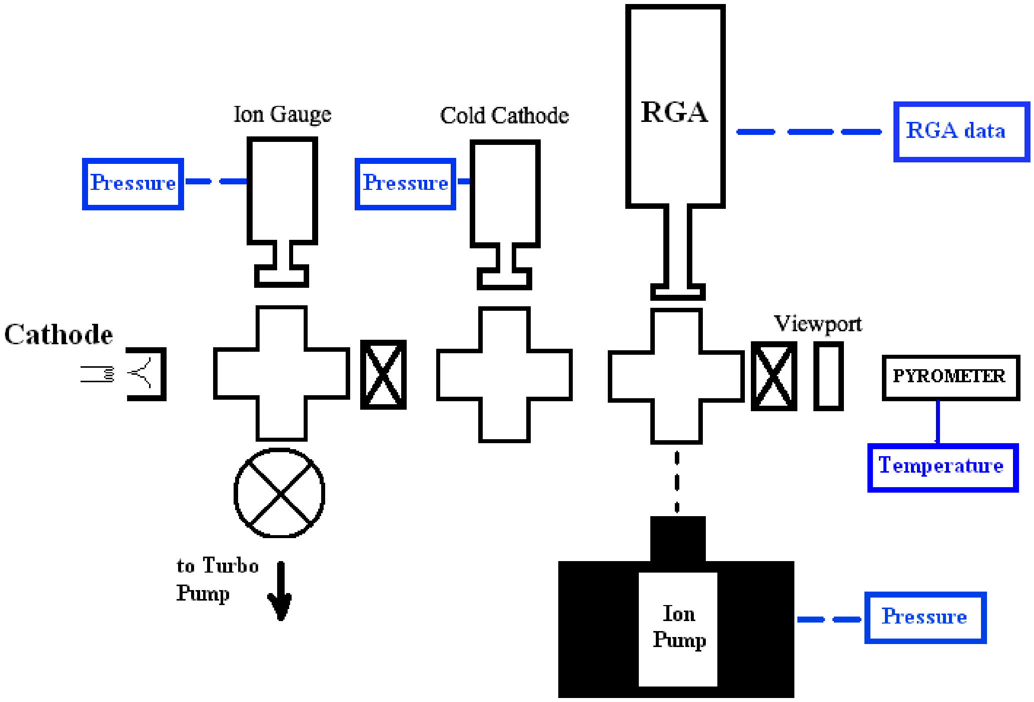

Figure 14. Eimac Cathode Test Stand

In the figure, the cathode is mounted at far left and a quartz crystal viewport at far right. A series of gate valves allowed for isolation of individual system components while maintaining the rest of the system at vacuum. The entire system was small enough to be table-mounted and easily moved by two people.

Before addressing the experimental data, we shall discuss the various instruments and devices employed in this test.

1. The Eimac Thermionic Dispenser Cathode

In designating the cathode as a ‘dispenser’ cathode, CPI means that the cathode body is constructed of a tungsten matrix evenly impregnated with barium oxide, which lowers the work function of the surface. Normal operating ranges for the Y-845 range from 950 °C to 1100 °C. The left picture in Figure 8 (Chapter II) depicts the internal structure of this style cathode. The cathode is designed to run off alternating current and requires no air-cooling, or other such input, in order to achieve basic thermionic emission

[40]. The atmospheric pressure side of the cathode has four concentric cylindrical electrical contact rings, seen in the picture at left in Figure 15 and depicted schematically at right.

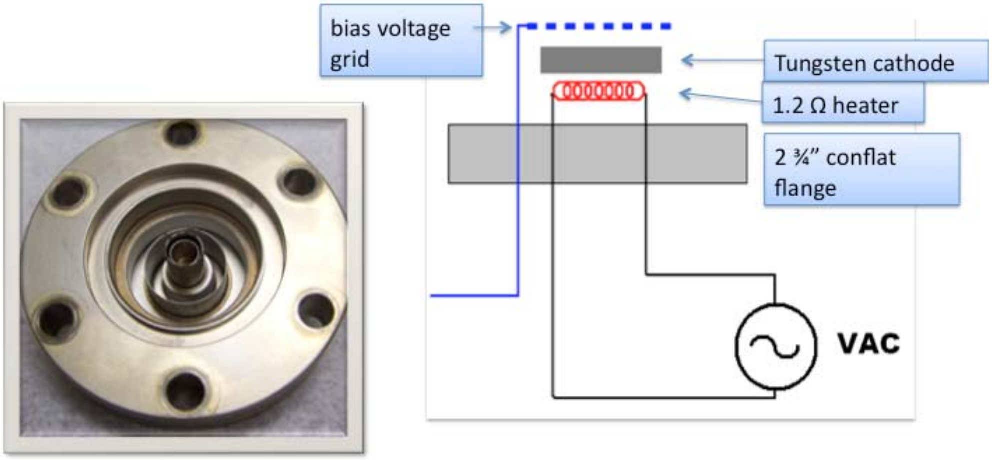

Figure 15. Electrical contacts on the Eimac Y-845 Cathode

The inner two rings connect to the 1.2 Ω (at 20°C) heating element. The next ring out connects with an electrical bias grid. A bias voltage placed on this grid would either allow or suppress electron emission from the cathode face. Electron emission was not our experimental focus, so we ignored this contact. The outermost contact serves as a grounding point for the flange, and is not depicted in the schematic.

2. Residual Gas Analyzer (RGA)

We utilized the Stanford Research Systems RGA-100 to provide mass spectrum data in this test (Figure 16). RGAs are mass spectrometers designed to be directly connected to a vacuum system and analyze the gases inside the vacuum chamber [41]. The instrument operates by ionizing a small fraction of the present gas molecules, separating these ions, and then measuring the ions according to their molecular mass. The “100” designates the SRS RGA as able to scan for particles with molecular masses from 1 to 100 atomic mass units (AMU). Other versions of this instrument can detect particle species up to 300 AMU.

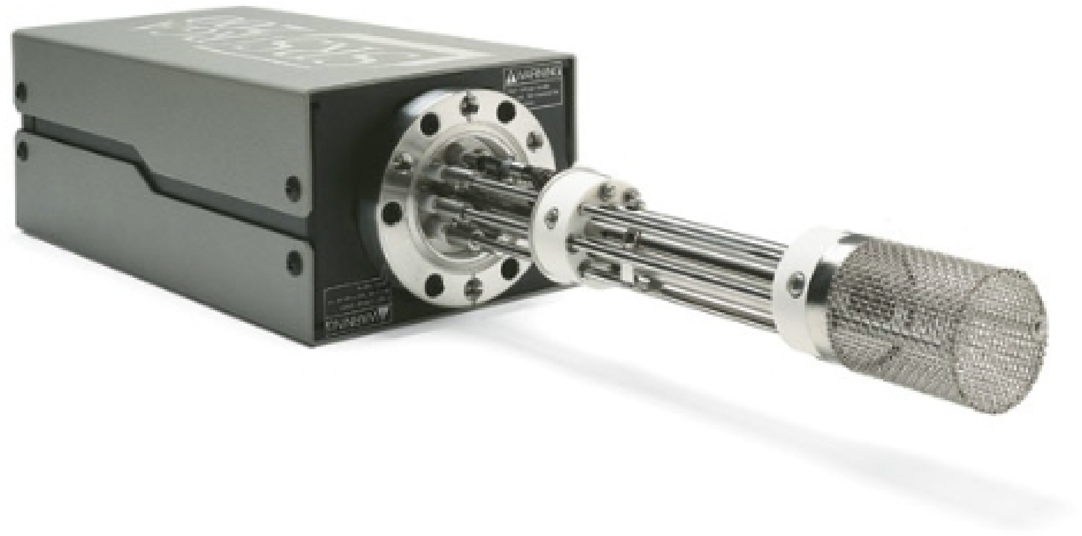

Figure 16. Stanford Research Systems RGA100 (From: [41])

During operation, a hot filament in the ionizer head of the RGA produces a population of positive ions. This ionizer head is the mesh cage seen at far right in Figure 16, and shown schematically in Figure 17.

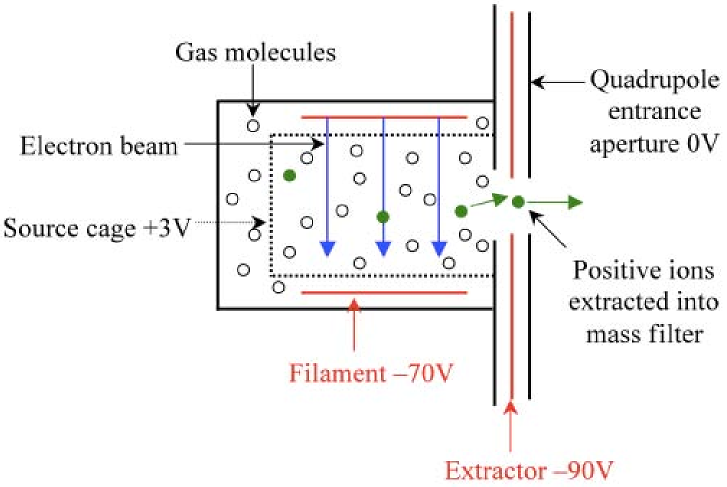

Figure 17. Schematic of RGA ionizer head (From: [42])

The outermost cage is negatively biased in order to drive the electrons into the center of the space where they either strike a gas molecule or are collected by the source cage. When struck by an electron, gas molecules positively ionize and are driven through an aperture seen at right in Figure 17. After passing through the aperture, they find themselves in the quadrupole section of the RGA (Figure 18).

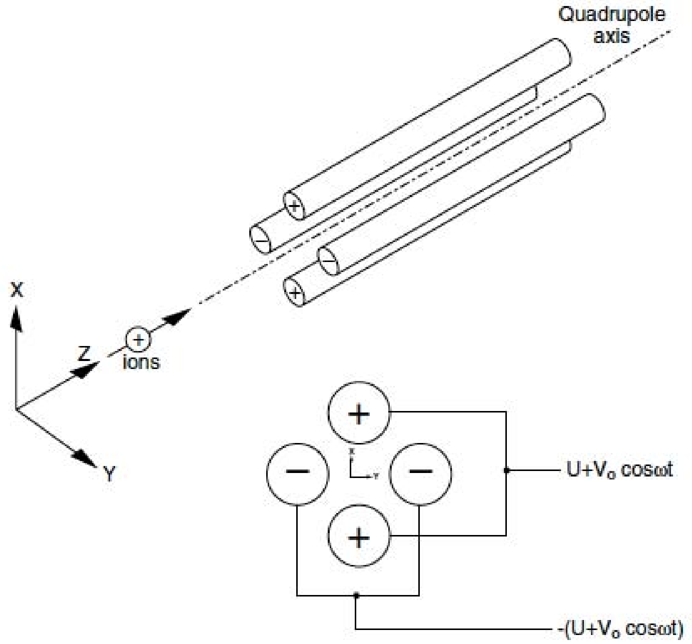

Figure 18. RGA Quadrupole Section (From: [41])

As the ions pass through the quadrupole section, they experience a constantly fluctuating E-field induced by four parallel steel rods. For a given frequency, ω, only ions with a specific charge:mass ratio will evolve down the z-axis of the quadrupole. All other ions will either strike the quadrupole electromagnets or the wall of the chamber that enclose this assembly. The RGA can effectively scan across many different charge:mass ratios by varying the frequency of this E-field. If an ion successfully passes through the quadrupole section, it will strike a metal plate and induce a current as it reclaims the electron it lost during ionization. By running a continuously varying frequency through the quadrupole and tracking the current, the RGA can determine the partial pressure of many charge:mass species and determine the constituent gasses in the vacuum.

One particular problem with the RGA is that it identifies charge-to-mass ratios, not specific atomic masses. How does this play out? Molecular nitrogen, for example, has the same atomic mass as carbon monoxide, and is indistinguishable based on a strong signal at 28 AMU. Another complicating factor of the electron impact type ionization used by this RGA is that more than one type of ion will generally be produced from a single type of gas molecule. For example, if we look at the signature for nitrogen in Figure 19 we see peaks at 28 and 14.

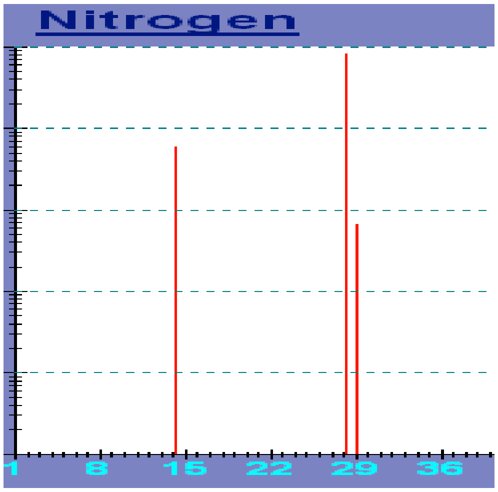

Figure 19. RGA software library's reference spectrum for nitrogen gas (From: [41])

We interpret this spectrum as molecular nitrogen (N_2) ionizing to produce N_2^+ as well as N^+/N_2^{+2} at a ratio of 10:1, based on the logarithmic scaling of the vertical axis. As molecular species get heavier and more complex one can expect an increased number in ion sub-species created. This complicates the spectral signature, and requiring a more robust analysis than the naked eye can achieve. To this end, the RGA software contains an analytical tool that completes the full spectral analysis. Despite this, the software is still fallible, and the final responsibility of identifying constituent gasses still rests with the experimenter [41].

3. Pressure Gauges

Pressure measurement at low pressure ($<10^{-3}$ Torr) is almost exclusively achieved via some form of ionization gauge. The two main gauge types utilized to this end are the hot cathode gauge (HCG), and cold cathode gauge (CCG). Each has their particular advantages and disadvantages, which one must know in order to decide which to use in a particular scenario (if both are not used). Regardless of which gauge we talk about, the end result of measuring vacuum pressure is achieved by measuring a current that is generated by a stream of ions created by the gauge. How the gauge produces this stream of ions is the source of difference between the two gauges.

a. Cold-Cathode Gauge (CCG)

The Cold Cathode Gauges (Figure 20) uses crossed electric and magnetic fields to create a localized circulating cloud of electrons. This electron plasma collides with nearby gas molecules and ionizing them. These ions are collected at a biased filament and the resultant current corresponds to the pressure in the vacuum. Standard operating voltages range from 2-6kV and magnetic fields range from 1-2 kG. Care should be exercised when handle cold cathode gauges due to the intense magnetic field generated by the magnet. The magnet will loose strength if it is allowed to magnetize other objects such as tools or other components of the system. If this occurs, then the gauge must be recalibrated. In addition to this negative aspect of the CCG, they are generally considered less accurate than HCGs and should not be relied upon as the sole source of vacuum measurement for high accuracy applications.

Figure 20. Varian 525 Cold Cathode Gauge

CCGs do have several advantages over HCGs. They generally arrive at stable readings faster than HCGs during rapid pressure fluctuations between 10^{-3} and 10^{-7} Torr. They contain no filament to burn out and they experience much lower levels of outgassing than compared to the HCG. These advantages make the CCG a preferred instrument for applications requiring frequent pumpdowns (such as a cathode test stand).

The typical operating range of a CCG is between 10^{-2} and 10^{-9} Torr. The gauge reaches its upper pressure limit when the current becomes so large that heating from the exposed electrodes, and the resultant sputtering, becomes a threat to the gauge's integrity. This usually takes place around 10^{-4} Torr, but several tricks can coax the useful limit into the 10^{-2} Torr range. The lower pressure limit is a function of the ability for the gauge/controller to collect & measure the current (on the order of picoamps). The particular gauge we used in our experiments had a low-pressure read limit at around 10^{-7} Torr. At pressures below this pressure, the gauge controller (the TerraNova 960) was unable to read the current and gave an error code to this effect.

b. Hot Cathode Gauge (HCG)

The majority of HCGs used are of the Bayard-Alpert design. A Bayard-Alpert gauge (BAG) boils electrons from a hot filament and accelerates them towards a cylindrical grid cage. As electrons traverse the space within the grid, which is fully open to the vacuum chamber, they collide with gas molecules and ionize some of them. The positive ions are drawn toward a fine wire at the center of the grid and produce a current proportional to the gas density at the gauge. The particular BAG we used in our experiments (Figure 21) was a nude-gauge, meaning that the filament and cage were fully exposed and insert into the test chamber.

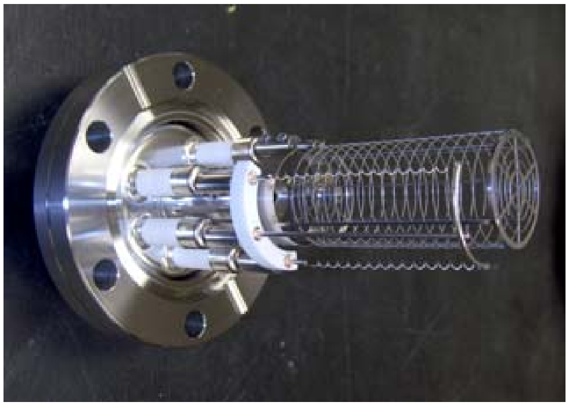

Figure 21. Nude Bayard-Alpert Gauge

This nude style gauge has the advantage of being able to directly measure the pressure of a given chamber without having to correct for vacuum impedance. The downside of this style gauge is that the filaments and cage are susceptible to damage. During the course of these experiments, one ion gauge touched the grounded wall of the vacuum chamber. This caused an overcurrent that destroyed the controller circuitboard card and caused to a two-week experimental delay as we searched for a new card. The alternative to the nude BAG is the glass-enclosed BAG, as seen in Figure 22.

Figure 22. Glass enclosed Bayard-Alpert Gauge

The advantage to this style gauge is that there is no risk of inflicting the kind of damage that led to the aforementioned short circuit with the nude BAG. Two disadvantages of the glass enclosed BAG are:

1) danger of fracture/implosion, leading to vacuum system damage as well as the risks posed to nearby personnel by flying glass, and

2) pressure inaccuracies due to the vacuum impedance caused by the narrow tube joining the gauge to the system.

BAGs have a useful operating range between 10^{-3} and 10^{-10} Torr. They are generally considered more accurate than CCGs due to the strict linear dependence of current to pressure (CCGs have a very non-linear correspondence). On the negative side of things, BAGs have hot filaments that can both outgas as well as change the composition of the gas in the vacuum system. Also, the filaments will eventually burn out after several thousands of hours of use. For this reason, each gauge usually comes with two filaments, a primary and a backup. Along with these potentially troublesome qualities, the BAG does get very hot and will heat nearby surfaces. The unwary experimenter can easily burn his skin by touching these hot surfaces [43].

4. Variac Adjustable Transformer

Though not shown in Figure 14, the EIMAC Cathode Test Stand utilized two Variac Adjustable Transformers to power the cathode heater (Figure 23).

Figure 23. Variac AC power supplies

These power supplies plug directly into 120VAC, and by means of an adjustable dial on the front, outputs the requested AC voltage. These transformers are not precision devices, so when it came to regulating the cathode voltage within 1/100th of a volt we found it necessary to daisy chain two Variacs, with the first providing coarse voltage control, and the second allowing for much finer voltage regulation. Even at that, the output voltage was subject to creeping up or down as the heated filament's resistance changed with temperature.

Note: All references to voltage in this work will imply V_{AC}(rms).

5. Let's Get Pumped…Vacuum Pumped

More than one kind of pump is required to achieve high vacuums, and pumps that operate efficiently at atmospheric pressure cannot achieve any lower than 10^{-3} Torr, a 'rough' vacuum, from whence the name of this type pump is derived. Conversely, pumps that operate at high and ultrahigh vacuums are inefficient or entirely inoperable at atmospheric pressure.

a. Roughing Pump

"Roughing pump" is a generic term for any pump used for the initial pumpdown of a vacuum system. Care must be taken in choosing a roughing pump, as some pump designs have lubricating oil that is exposed to the vacuum. If anything goes wrong, either mechanically or procedurally, oil may shoot back into the vacuum system and cause great harm to the vacuum components [44].

b. Turbomolecular Pump

Turbomolecular pumps ('turbopump' for short) are pumps designed to achieve and maintain vacuum levels upwards of 10^{-8} Torr. These pumps operate on the principle that gas molecules can be given momentum in a given direction by repeated collisions with a moving solid surface. In a turbopump, a series of rotating blades repeated strike gas molecules at the inlet towards the exhaust in order to achieve and maintain high vacuum levels at the inlet [45]. Figure 24 shows a cutaway view (left) and schematic diagram (right) of a basic turbopump without accompanying hardware.

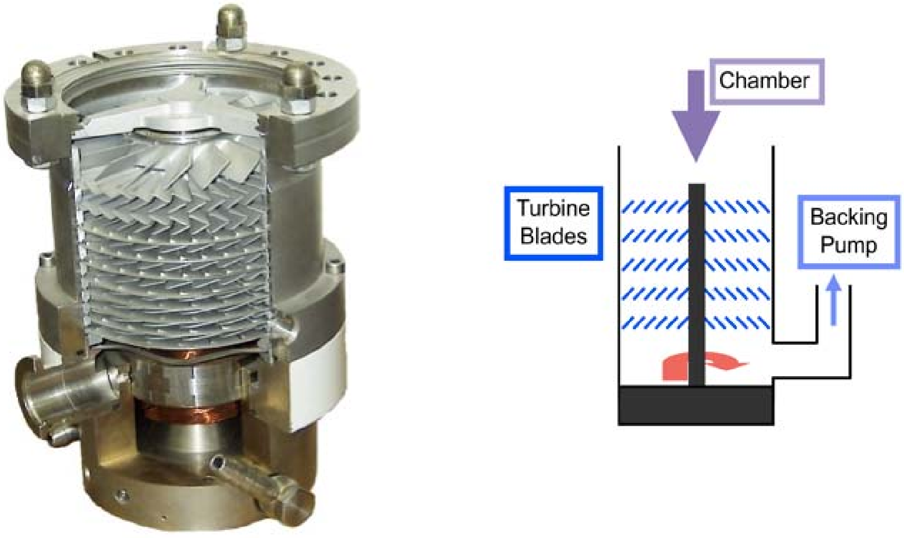

Figure 24. Picture and schematic of turbomolecular pump (From: [46])

The inlet, outlet, and rotor assembly are easily visible in both pictures. In order to achieve the desired vacuum levels at the inlet, the rotor assembly must rotate at speeds upwards of 50,000 rpm. Many modern pumps use magnetic bearings & electronic stabilization of the rotor in order to avoid the problem of using oil lubricated bearings.

Due to the high rotor speeds, delicate construction of the rotor assembly, and the magnetic bearings, turbopumps can easily break if the vacuum is suddenly lost at the inlet. Large pressure spikes can induce large mechanical loads on a spinning rotor that would likely damage the pump. As such, the vacuum at the pump should be maintained during spin-down. An added safety feature on turbopumps is a metal collar surrounding the rotor assembly that are strong enough to absorb the explosive impact of the shredded rotors, similar to the armor jacketing surround jet engines' turbine assemblies.

c. *Ion Pump (IP)*

Ion pumps (Figure 25) are a standard piece of equipment when it comes to ultra high vacuum (UHV) systems. They provide a clean, low-maintenance, and simple means of producing and maintaining ultra high vacuums.

Figure 25. Ion Pump used for EIMAC cathode test stand

Ion pumps come in a variety of configurations, but the essential points of operation are similar despite the minor differences. The basic ion pump is schematically depicted in Figure 26. It operates by creating a high voltage (3–7 kV) differential between the internal anode and the titanium pump wall, the cathode.

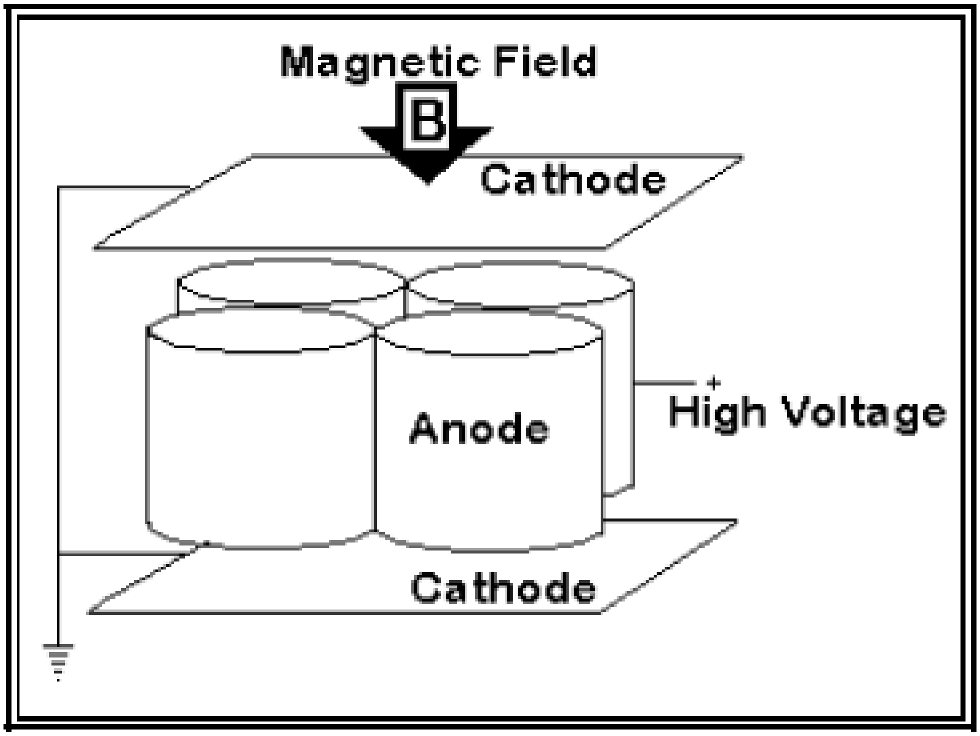

Figure 26. Simple Diode Ion Pump (From: [47])

A magnetic field is supplied via permanent magnets that jacket each side of the main chamber, as seen in Figure 25. Gas molecules entering the pump are ionized by the anode and subsequently removed from the vacuum by a combination of various mechanisms. Small atoms such as hydrogen and helium are directly buried and diffused into the titanium walls of the pump. Subsequent heating, intentional or otherwise, may release these gasses into the system. Heavy noble gasses, being chemically neutral, do not react with the titanium walls, but are rather buried and covered over by subsequent sputtered material. Absorbing large quantities of noble gases can lead to a phenomenon known as ‘argon instability’ by which a bursting pocket of gas causes a cascading reaction of similar pockets to burst. This process is identified by cyclical pressure fluctuations, and is best handled by a professional reconditioning of the pump.

The last pumping mechanism, for chemically active gasses, takes place when the ionized molecules react with the titanium and create a variety of stable low vapor pressure compounds that remain in the pump.

Ion pumps have a finite pumping ability, and care should be taken to create as good a vacuum as possible via turbo pumping before activating the ion pump. Additionally, it is a good practice to bake out ion pumps any time the system has been exposed to atmosphere. A bake up to 150°C with magnets in place, or 450°C with magnets removed, will prompt desorption of adsorbed contaminants. Note the dark burn circle on the side of the pump in Figure 25 caused by the ceramic heater element used during bake-outs [47].

In addition to providing UHV pumping, ion pumps are also able to give a reading of system pressure by measuring the anode current. This current is directly tied to the quantity of gas ionized by the pump and is a secondary indication of system pressure. Caution must be used when relying upon this pressure reading. Pump age, contamination, vacuum impedance, and other factors, can cause ion pump pressures to read higher than actual system pressures.

A historical side note—ion pumps were invented by experimenters who noticed that turning on ion gauges caused pressure drops in sealed systems even when there was no external pumping. The basic principles of operation are the same for both instruments.

6. Optical Pyrometer

All matter emits radiation as a blackbody source. Pyrometry is the practice of measuring a radiant object’s temperature by comparing some element of its radiated spectrum against a radiant source (usually a filament) of known temperature. While this process can be done manually, there are now easily obtainable automated systems that can do this. We employed a pyrometer manufactured by Omega Engineering that utilizes 2-color ratio temperature measurement in order to measure the cathode temperature. Since the intensity ratio of different wavelengths is a physical invariant for a given blackbody temperature, this pyrometer can accurately measure object temperatures regardless of emissivity, relative obscuration by windows, etc… [48].

C. EXPERIMENTAL OUTLINE: ACTIVATION AND RE-PROCESSING

CPI lists the activation process for the Eimac Y-845 cathode as follows [40]:

1 –Bring the shipping vessel up to atmosphere by piercing the vacuum vessel.

2 –Install new seal gasket, install into system, and apply vacuum of 10^{-7} Tor for a minimum of 30 minutes.

3 –Raise filament voltage 0.5 V every five minutes to 8.0 V (1180 °C) & hold at 8.0 V for five minutes. As necessary reduce the power to the cathode if the vacuum ever increases to above 10^{-7} Tor.

4 –Lower voltage to 6.8 V & let cathode stabilize for 30 minutes before shutdown.

CPI, the publisher of these activation procedures, advises the user avoid operating the cathode at pressures above $1\text{x}10^{-7}$ Tor [49]. Gas concentrations above this level can damage the cathode surface via oxidization and ion back bombardment that may permanently degrade the cathode. On the other hand, if the cathode is exposed to air or otherwise mildly contaminated it can be re-processed by executing steps two through four of the activation procedure.

D. EXPERIMENT #1—REPROCESSING AN OLD CATHODE

Before activating our new Eimac cathode, we chose to attempt the same with an old Eimac cathode we had acquired from Stanford. This cathode had been exposed to atmosphere and unknown contaminants for several years. Additionally, we observed noticeable blistering of the cathode surface with the unaided eye, such as mentioned as a potential form of damage in Chapter III. Despite this visible damage, we pressed forward with the processing of this cathode as a means of getting our ‘experimental feet’ wet before activating a new Eimac cathode.

First power was applied to the old Eimac at 1225 on 15 Jan, and the activation cycle was completed at 1218 on 29 Jan—fourteen days from beginning to end. When we first applied power to the old Eimac, it outgassed a great deal of contamination that quickly moved the system pressure up to the prescribed $1\text{x}10^{-7}$ Tor ceiling. All this contamination needed to get pumped out by migrating through almost a half meter of narrow 1 1/3" (inner diameter) vacuum tube, around a corner, through a narrow neck, and down into the ion pump. At this point of the experiment, we encountered the effect known as 'vacuum impedance.'

In its simplest form, vacuum impedance is the observed pressure differentials seen between different parts of an ostensibly equal-pressure system—something particularly noticeable at ultra high vacuums. Pressure is directly tied to the number and energy of molecules 'bouncing around' in the system. Molecules take time to bounce from one part of a vacuum system to another, and physical constraints such as narrow pipes and bends slow down the migration of these molecules and lead to measurable pressure imbalances.

As cathode voltage increased, we saw a corresponding pressure rise as the cathode outgassed adsorbed contaminants. Given the quantity of material outgassing from the cathode, the high vacuum impedance, and the pressure limitation of $1\text{x}10^{-7}$ Tor, we found it necessary to wait upwards of 20 minutes before the pressure dropped to an acceptable level before increasing the voltage by a few hundredths of a volt. All told, we spent over 21 hours bringing the cathode from 0.0 V to 2.9 V. At this point, we received advice on how to decrease the vacuum impedance and reconfigured the test stand, as seen in Figure 27.

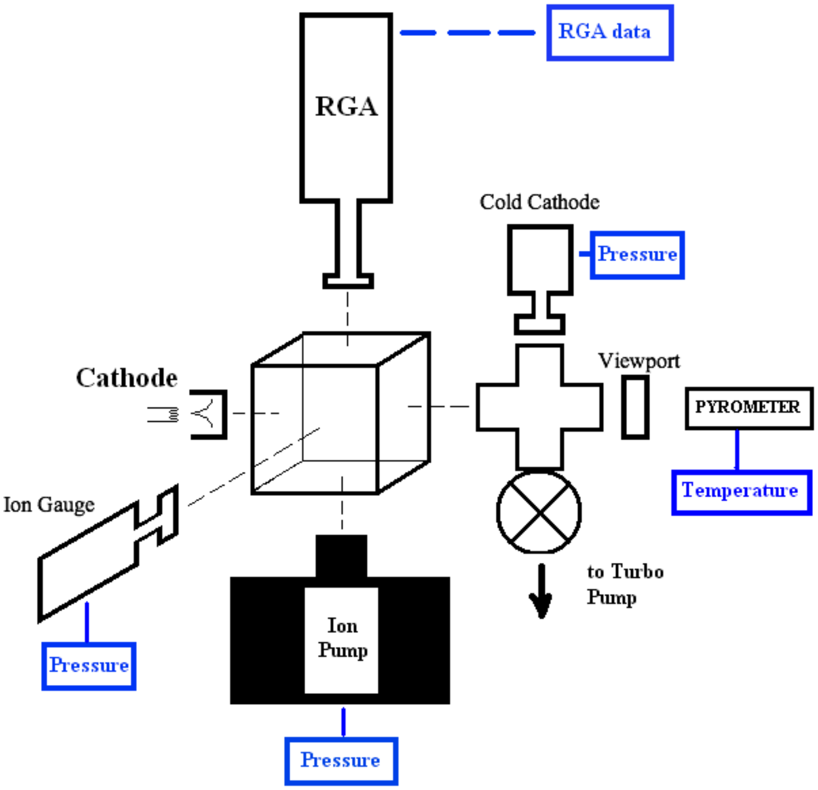

Figure 27. Reconfigured Eimac test stand

This system used a 6-inch, 5-way, cross as the test chamber that sat directly over the ion pump. This effectively eliminated the vacuum impedance between the cathode and ion pump such that the remainder of the test proceeded at a quicker rate than the initial portion thereof. Figure 28 shows the pressure and voltage history from the processing test. The entire process took place over a two-week period that included down time for system reconfiguration (noted at the ~26 hour point). Each experiment day of the activation cycle is indicated at the bottom of the horizontal axis. The five vertical gray bars are 2-hour blocks that visually distinguish one experiment day from the next.

The horizontal axis shows experiment run time in HH:MM format. The left vertical axis shows applied voltage while the right vertical axis shows system pressure measured at the ion pump and the HCG.

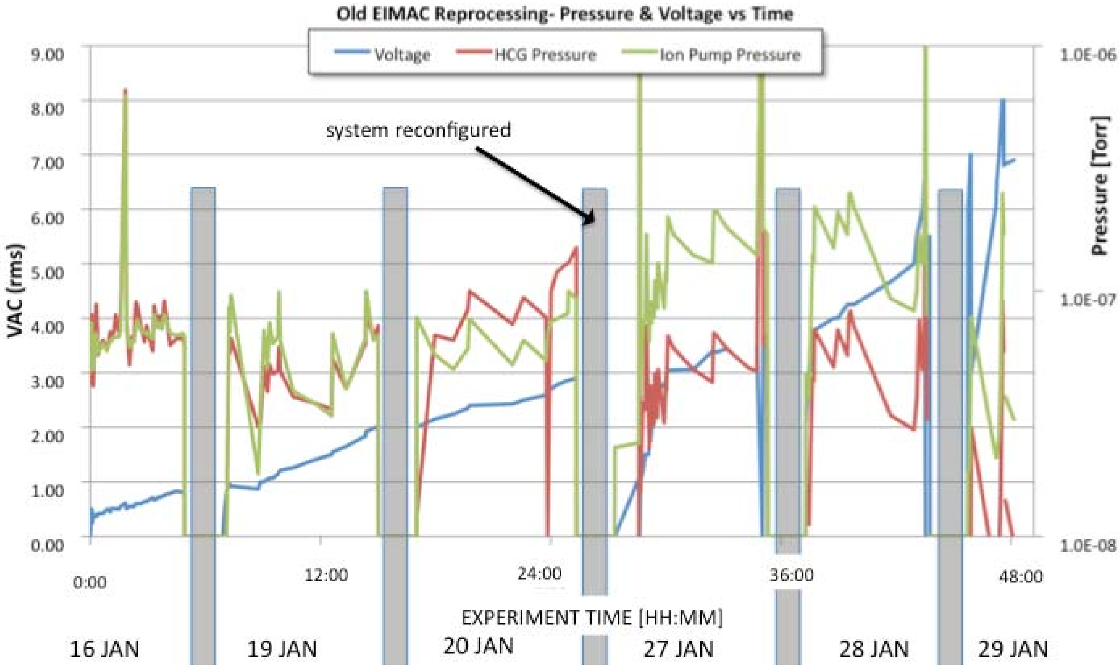

Figure 28. Activation cycle—old Eimac cathode

The steadily increasing blue line charts applied voltage and scales against the left vertical axis. System pressure, both HCG and ion pump, scale against the right vertical axis. All told, the activation cycle for the old Eimac Y-845 lasted 38 hours. Several spikes are visible where the pressure exceeded the 1x10^{-7} Torr limit. The first three spikes were caused by applying too great a filament voltage where the last was caused by a mechanical shock to the experimental apparatus that translated into a pressure spike.

Figure 29 gives a graphical breakdown of the relative partial pressures of select gasses, as measured by the RGA, during the course of the processing cycle. Before interpreting this plot, we must understand three things about the RGA analysis process. First, the partial pressure of one gas is only measured against the other select gasses, and not against the entire sum of gasses in the vacuum. Second, though hydrogen was the primary contributor to vacuum pressure, we have not included it in this graph. In most cases it is the dominant gas in a vacuum due to its extremely low pumping rate. Its inclusion would so compress the relative pressures of other included gasses as to make a chart unsuitable for presenting the data. Third, we must understand there is some error inherent with the RGA software's analysis. Due to the similar spectroscopic signature of some gasses, the relative partial pressures of these species can fluctuate widely between scans based on rather small changes in the input signal [41]. Two gasses for which this is a common occurrence are molecular nitrogen (N_2) and carbon monoxide (CO). For that reason these two gasses are, and will always be, grouped together in RGA data presented in this work.

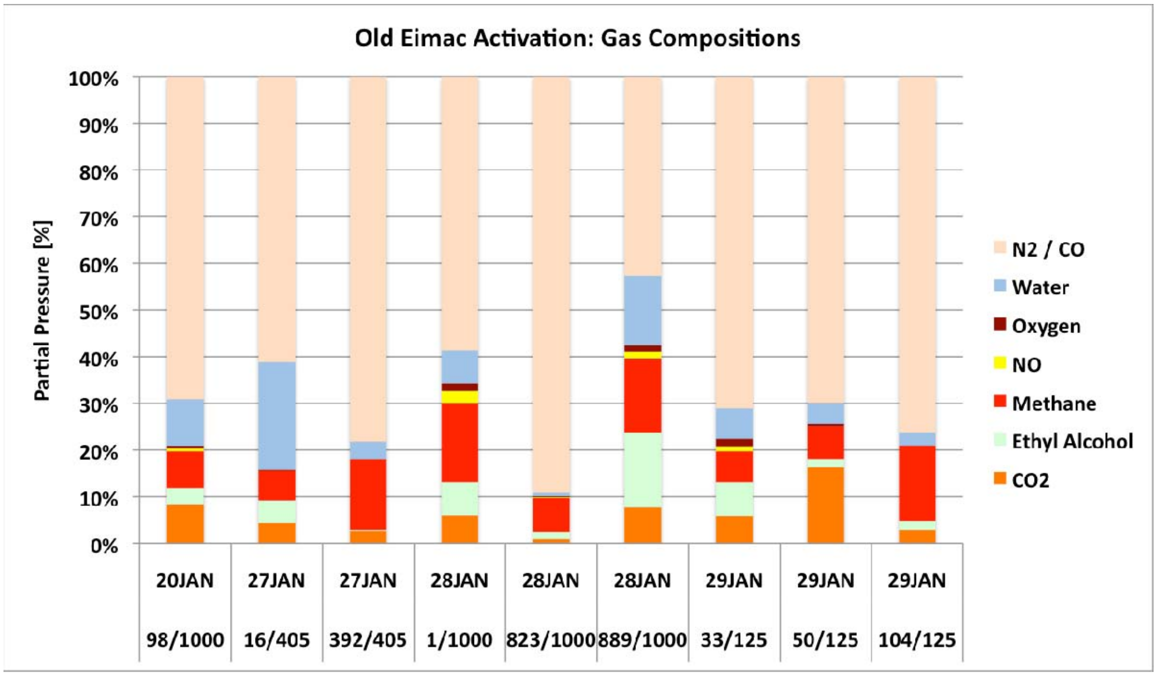

Figure 29. Partial pressures of various gasses—old Eimac processing

The bottom axis breaks out the experimental days, as well as the respective RGA scans from which the data were extracted. The vertical axis shows the relative partial pressures of each gas versus the group of gasses as a whole. An important fact to note is that the percentage partial pressures are not scaled against the total vacuum pressure, which would necessarily consist of other gasses as well.

RGA data are not presented for the first two days of cathode processing. During the first two experimental days, we discovered the importance of properly preparing one's instruments, which for an RGA means a thorough bakeout during pumpdown according to the manufacturer's guidelines. Our failure to bakeout the RGA assembly led to such initial high outgassing levels that the signal was unusable. By the third experimental day (20 Jan) the outgassing had diminished to a level whereby the RGA became a useful tool. During system reconfiguration and pumpdown (between 20 Jan and 27 Jan), we had the opportunity to properly bake the RGA and by doing so drastically improved the quality of data coming from the instrument for the later portion of the test.

While no discernable trend was clear in this data, valuable experience with vacuum system design and diagnosis was gained. Knowledge gained in learning how to obey high vacuum cleanliness procedures, configuring vacuum systems, and the proper handling of lab instruments paid dividends on all future tests.

E. EXPERIMENT #2—ACTIVATING A NEW EIMAC Y-845

After taking multiple days to process the old cathode, the new cathode was very easy to activate in comparison. In order to switch the old cathode with the new, we had to bring the vacuum system up to atmospheric pressure. We used dry oil-free nitrogen (99.99% pure) in order to protect both the cathode and the test chamber from atmospheric contaminants. We also conducted the installation of the new Y-845 cathode under a nitrogen bag to avoid atmospheric contamination.

First power was applied at 0957 on 03 Feb and the cycle was completed at 1223 of the same day. Figure 30 plots HCG pressure, ion pump pressure, and voltage against time.

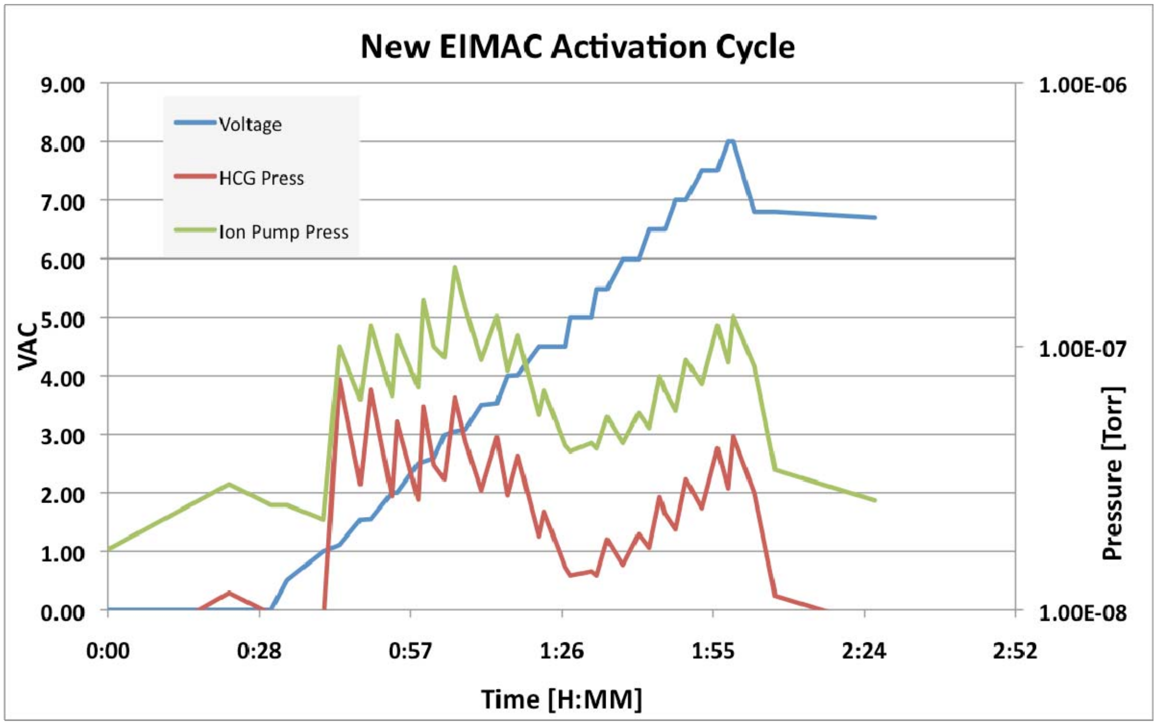

Figure 30. Activation cycle—new Eimac Y-845

Due to the system configuration, the HCG reflects the pressure near the cathode more accurately than the ion pump. This is the pressure we monitored in order to stay below the 1×10^{-7} Torr limit at all times during the activation process.

Figure 31 depicts the partial pressures of select gasses over the course of the activation cycle. As before, hydrogen has been excluded from this plot due to its dominant presence in the vacuum.

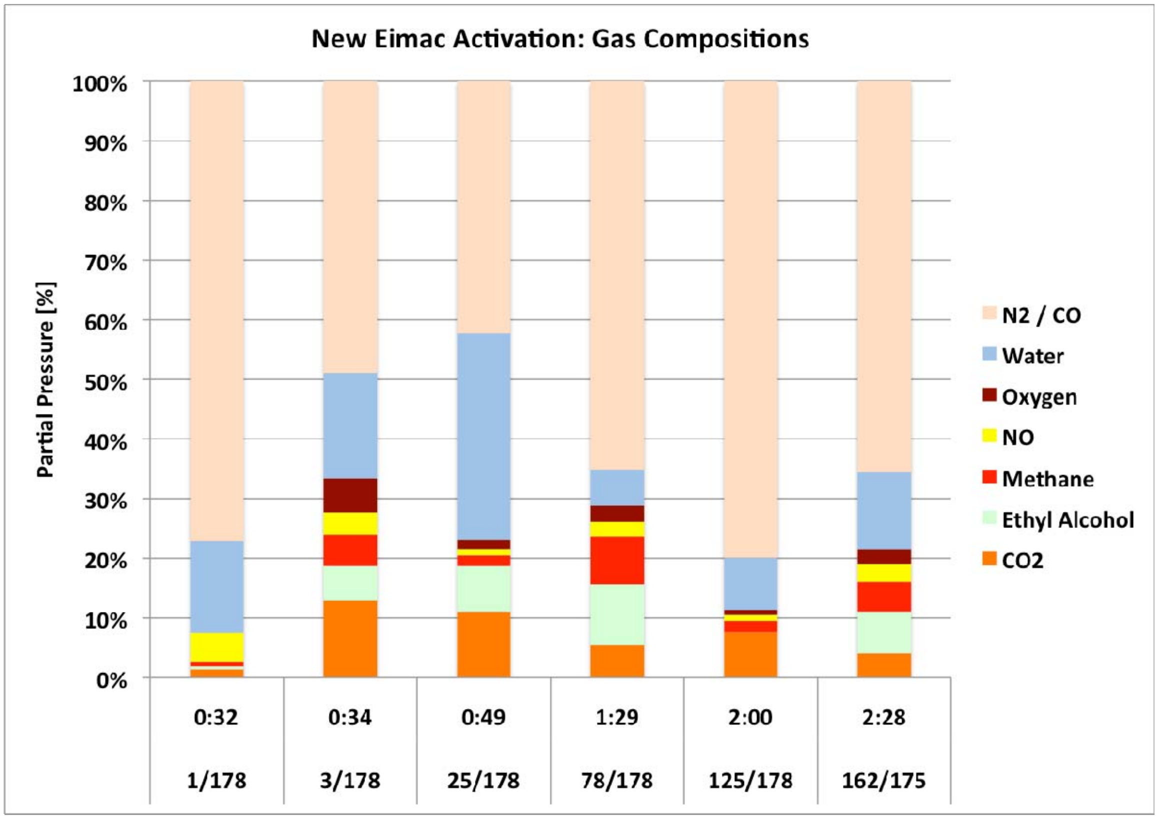

Figure 31. Partial pressures of various gasses (new Eimac activation)

We see both the time of the data sample, as well as the corresponding RGA scan, along the horizontal axis of Figure 31. Scan 1/178 depicts the background vacuum before applying power to the cathode filament. After applying power, we notice a definite increase in certain background gasses such as carbon dioxide, methane, and ethyl alcohol. All of these are unsurprising as carbon dioxide and methane are common gas contaminants, and ethyl alcohol is the lab solvent used in cleaning vacuum components.

We have included Figure 32, which is a raw RGA scan, in order to present the reader with a better understanding of the raw RGA data output from which the previous figure was generated. The vertical axis shows pressure logarithmically in Torr, and the horizontal axis shows the atomic mass species.

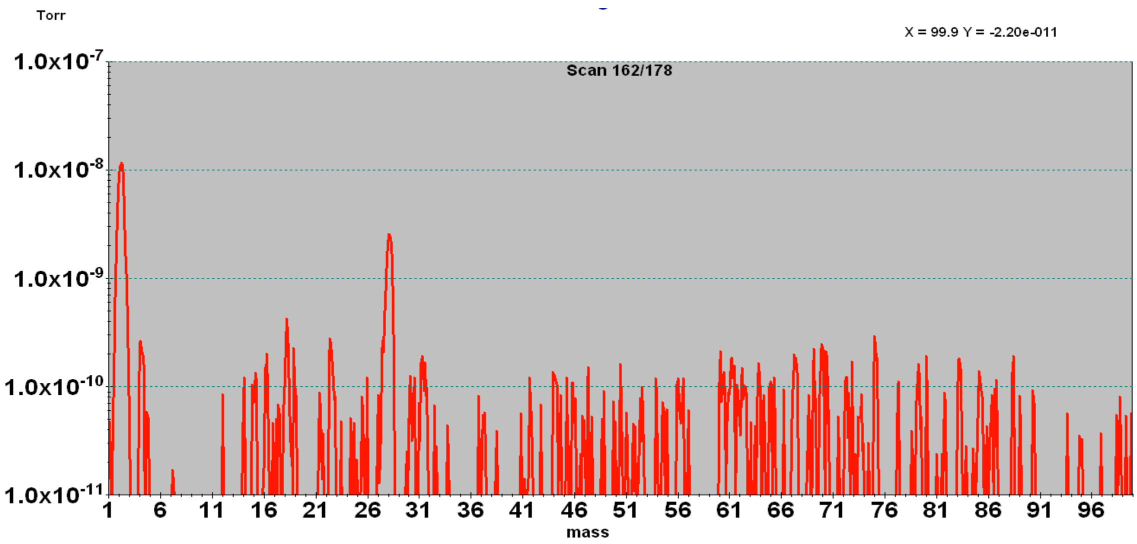

Figure 32. Representative RGA scan (at 6.80 V)

The only significant peaks at this point are at molecular masses 2 and 28, signifying hydrogen, CO, and N_2. The rest of the analysis as seen in Figure 31 should be taken with a grain of salt. The background noise level of the RGA rests in the low 10^{-9} Torr, and minor fluctuations in this noise caused appreciable changes in the relative partial pressures of other gasses from scan to scan [41].

F. POWER VERSUS TEMPERATURE

One item of interest to our effort was a characterization of power applied versus cathode temperature. Not only did we want to know the Temperature vs. Power characteristics for individual cathodes, but we also wanted to check that the thermal performance was consistent between cathodes. Figure 33 shows power applied on the horizontal axis and the corresponding temperature on the vertical axis for both the old and new Eimac cathodes. Additionally, the theoretical maximum temperature is shown according to the Stefan-Boltzmann law that relates the power radiated from an object to the object's temperature. In the following equation:

$$P_{\text{radiated}} = A\varepsilon\sigma(T^4 - T^4_{\text{amb}}) \qquad [3]$$

A = object's area, ε = emissivity = 0.7[1][50], σ = Stefan-Boltzmann constant, T = object's temperature, and T_{amb}= ambient temperature = 300K.

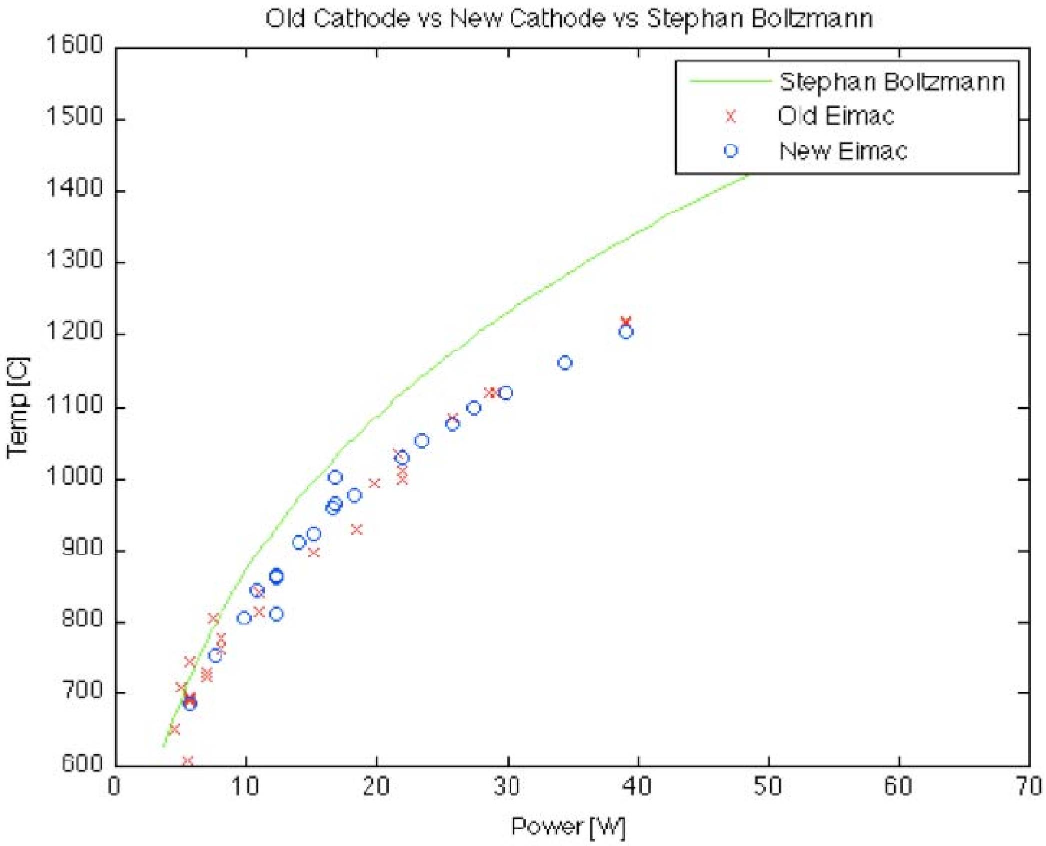

Figure 33. Temperature vs. Power, Eimac Y-845

The disparity between both cathodes and Stephan-Boltzmann radiation was caused by conductive heat dissipating through the cathode assembly.

G. CONCLUSIONS

1. We processed one old Eimac Y-845 cathode with an unknown degree of contamination. The cathode had so much contamination that it took six experimental days to accomplish this task. In order to ascertain the final results of the processing procedure we would have to subject the cathode to

---

[1] The emissivity of tungsten depends on many physical factors, including temperature. After looking at various data I chose to use a value of 0.7.

electron emission testing. This is beyond the scope of our present research but not technically difficult to do, given the proper experimental setup.

2. The activation of the new Y-845 occurred on schedule with CPI Corporation's published instructions. No notable contamination occurred during this activation.
3. Both cathodes have similar thermal performance. Without a larger test sample, we cannot make sweeping generalizations concerning Y-845 cathodes. This would be impractical for our group to do, as we only require only one or two cathodes at any one time depending on current experimental goals.
4. Activation and thermal characterization of future cathodes can easily be accomplished with the test stand layout depicted in Figure 27.

Figure 34. Eimac Y-845 at maximum voltage (8 V)

THIS PAGE INTENTIONALLY LEFT BLANK

V. THE DISPENSER PHOTOCATHODE CAVALCADE

A. MOTIVATION AND PURPOSE

One problem with photocathodes, as previously mentioned, is the challenge of getting both a high QE and a long lifetime. The photocathodes with the highest QEs generally have some kind of atomic monolayer coating, such as cesium, that lowers the work function but also deteriorates quickly. What can we learn from thermionic cathodes that may help solve this dilemma?

The technology that helped create the thermionic dispenser cathode is very mature, having been developed over the last six-plus decades [13]. We have already seen, with the EIMAC tests, a demonstration of barium-oxide dispenser cathodes at work. One of the disadvantages of the oxide-impregnation style cathodes, such as the Eimac, is that the diffusion rate of low work function material diminishes over time [17]. This decrease in diffusion is caused by the dropping concentration gradient over the cathodes' lifetime. In order to increase the overall supply of low work function materials, one can construct a cathode with a reservoir such as the barium carbonate cathode seen in Figure 35.

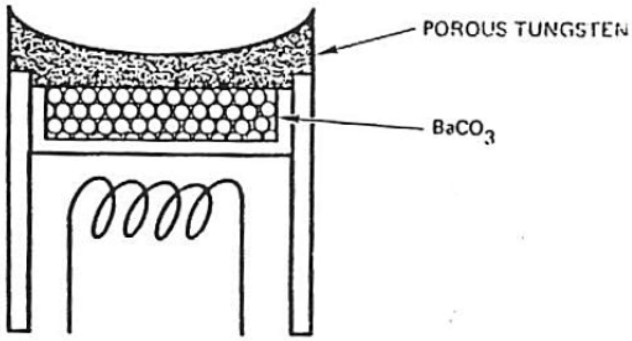

Figure 35. L-type reservoir dispenser cathode (From: [19])

A dispenser of this fashion can maintain a steadier diffusion gradient through the porous tungsten for a longer period of time since a much larger supply of material can be held in the reservoir versus what can be impregnated within the tungsten itself. These reservoir dispenser cathodes have been used since the 1950s and can achieve work functions as low as 1.8 eV[51]. Up to this point, these cathodes have been used as thermionic emitters. We are working with a team from the University of Maryland (UM) that is exploring reservoir dispensers in photocathode applications. Ideally, we want to create a cathode with a low work function surface that can be easily regenerated to extend lifetime far beyond current designs.

While creating a rejuvenable photocathode is of value to the particle accelerator community at large, the United States Navy has an additional motivation for investigating this technology. The Navy FEL is envisioned as having a superconducting RF injector. While superconducting accelerators have been in operation for 20+ years, this author only knows of three facilities (at most) that have successfully operated a SRF injector [5], [52], [53]. Needless to say, there are unknown factors about the operation and performance of such devices [54]. One big unknown is the effect of monolayer cesium contamination on SRF cavity performance. This author knows of no studies, theoretical or experimental, that explore this subject. Since the UM dispenser photocathode will emit cesium into the injector structure, it is of utmost importance to gauge its effect on SRF cavity operation. The goal of this experiment is to characterize the evaporation rate of cesium from the UM dispenser photocathode as a function of temperature for various heating regimes. Armed with this information, future research can focus on operational constraints and limitations with using a dispenser photocathode in SRF cavities [20].

B. PHYSICAL DESCRIPTION—UM DISPENSER PHOTOCATHODE

Figure 36 shows a schematic design of the generic University of Maryland dispenser photocathode. It is constructed with a stainless steel cylinder wall, nickel-brazed sintered tungsten disk that fits just inside one end of the cylinder, and a laser-welded steel cap on the back side. The sintered tungsten cathode face is brazed onto the cylinder before the cesium source is added. Once the cesium source is added, the bottom cap is laser welded onto the cathode. The decision to laser weld the back cap on is due to the desire to keep the temperature of the cesium source as low as possible during this final manufacturing step. If the temperature rises above 120°C there is considerable risk of releasing cesium while exposed to atmospheric conditions thereby ruining the cathode.

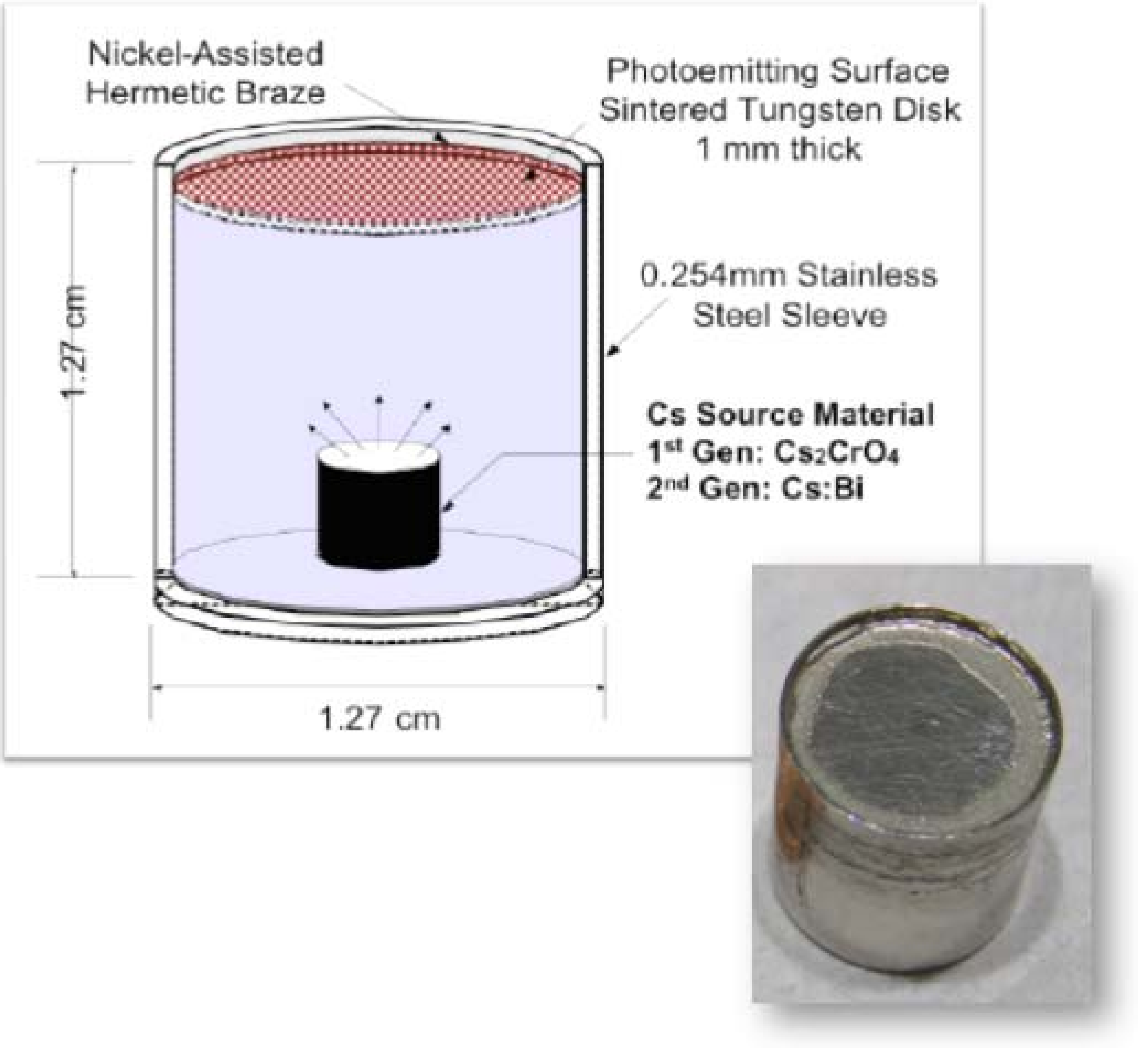

Figure 36. UM Dispenser Photocathode Schematic and Photo (From: [20])

The picture at bottom right of Figure 36 shows a 1st generation dispenser photocathode with a titanium:cesium chromate source. The hermetic braze is visible as the uneven ring around the cathode face. With the current status of the project, the primary region of concern on the cathode face is the central portion where the laser strikes. More recent versions of the dispenser have cleaner brazes such as will be necessary for future "production" models.

1. Sintered Tungsten Face

The sintered tungsten disk that forms the photoemissive surface of the cathode serves several functions. First, it provides a flat surface against which a laser will strike to promote electron emission. Second, it meters the flow of cesium from the internal reservoir to the surface. Third, it provides a base onto which the cesium will bond and form a low work function surface.

The porosity of the tungsten cathode surface must have certain design constraints. A tungsten face that is too porous would allow excessive diffusion of cesium as well as prove unsuitable for photoemission due to its roughness.[2] Too dense a surface would hinder consistent diffusion of cesium through the surface. To this end, the sintered tungsten's density has been bounded between 60% and 70%. Another important factor affecting cesium diffusion is the thickness of the tungsten disk. This design prefers thin disks to thick. Thin disks have more migration paths through the structure, allowing for more even cesium diffusion across the cathode surface. Additionally, thin disks allow for more rapid cesium diffusion through the structure at a given temperature [17]. Both of these effects are desirable in a cathode intended for regular rejuvenation. The University of Maryland has explored both 1-mm and 0.5-mm thick surfaces in previous tests. The current design uses a 1-mm tungsten disk due to manufacturing difficulties with the 0.5-mm tungsten disk.

2. Cesium Source Materials

a. Titanium:Cesium Chromate Dispenser

The first generation UM dispenser cathodes contained a bi-metallic compound made of titanium powder and cesium chromate (Ti:$CrCs_2O_4$) mixed at a 5:1 ratio and hand pressed into small pellets. At a temperature of 425°C the chromate reacts with titanium leaving free cesium in the dispenser cavity. After this initial activation, it only takes gentle heating to promote the migration of cesium through the tungsten disc

---

[2] Rough surfaces cause scattering of both the incident laser beam as well as scattering of the emitted electrons.

and to the surface. Reliability issues with this style dispenser prompted the group at UM to search for a more reliable cesium source. However, one dispenser was still available for our tests, so we took the opportunity to conduct cesium evaporation tests with it.

b. Alvatec Cartridge Dispenser

The search for a more reliable cesium source led the UM team to the Austria based Alvatec Corporation. Alvatec specializes in high tech metallurgy, and has manufactured several cesium ‘cartridge’ sources for the UM group. The cartridges are 8 mm x 10 mm stainless steel containers in which are placed 800 milligrams of the company’s highest concentration proprietary cesium-bismuth (Cs:Bi) intermetallic compound (65% cesium by weight)[20]. While the side and bottom are constructed from steel, the fourth side of the cartridge is made of indium, a soft metal with a melting point of 157°C. Figure 37 depicts a cartridge next to a penny for scale. The indium cap is seen at top with a slightly duller texture than the steel sides and bottom.

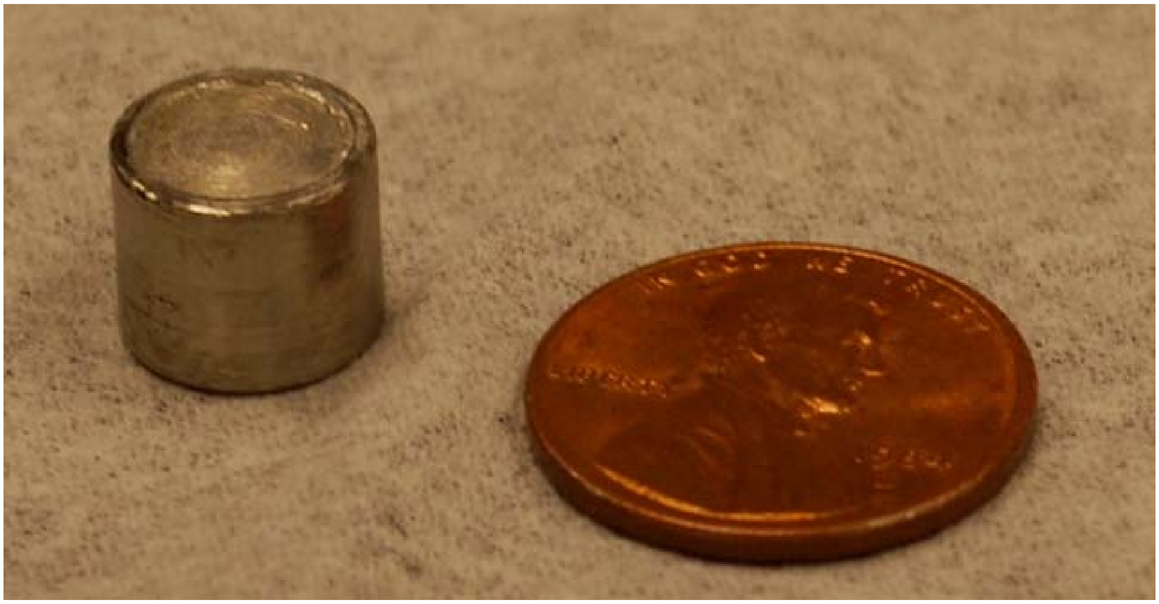

Figure 37. Alvatec cartridge, with penny for scale

Since cesium is a highly reactive element, Alvatec manufactures and seals the cartridges in an argon gas atmosphere. Argon, a noble gas, displaces reactive gasses and protects the cesium from oxidization that would otherwise ruin the cartridge. The cartridge is designed to activate via a two-step process. Heating the cartridge past 157°C melts the indium seal, thus exposing the Cs:Bi compound. Further heating of the cartridge (+300°C) causes the cesium to sublimate from the intermetallic compound and diffuse into the reservoir cavity. In addition to the Ti:Cs Chromate dispenser cathode, we also conducted cesium evaporation tests on one Cs:Bi dispenser cathode.

C. THE EXPERIMENTAL JOURNEY

As stated in section A, our experimental destination is the examination of the UM dispenser photocathode. Section B.2 details the internal composition of our two test cathodes. Before testing the dispenser cathodes for cesium evaporation, we found it necessary to conduct several preliminary tests. Some of these tests were anticipated while others were not. The following sections (V.D-V.G) will take us through these different 'pre-experiments' leading up to the actual testing of the dispensers in sections V.H and V.I.

This series of tests used many of the same instruments used in the EIMAC tests. Since we previously discussed these components in Chapter II, we will not do so again. Two components in this test are new—a deposition monitor and heater assembly.

1. Inficon Deposition Monitor

The first new instrument is a quartz crystal deposition monitor (QCM) manufactured by the Inficon Corporation. Inficon manufactures deposition monitors for vacuum process applications where the precise application of material on the atomic level must be monitored. We chose the BAK-100 bakeable deposition monitor (Figure 38) for this experiment as the primary means of monitoring the evaporation of cesium from the various samples we tested.

Figure 38. Inficon BAK-100 Deposition Monitor (From: [55])

The actual deposition sensor is the gold circle at far right in Figure 38. The top and bottom lines leading in from the left are for water-cooling and the central line is for electrical connections. The deposition sensor is a gold-plated quartz chip that vibrates at a given frequency between 5 and 6 MHz. As material is deposited on the crystal surface the frequency of vibration decreases according to the thickness, density, and shear modulus of the deposited material. The water-cooling lines maintain the crystal at a constant temperature. Changing temperatures will also alter the crystal frequency and introduce errors—section V.G will explore this effect in detail. At its best, this sensor has a resolution on the order of Angstroms, enabling it to detect monolayers of cesium (cesium atoms have a diameter of ~5Å).

2. Heater Assembly

Our group wanted a heating element that we could accurately control to within +/- 10°C in order to accurately test the thermal characteristics of the dispenser cathodes. We chose to buy our heater assembly from HeatWave Labs Inc. (Figure 39) because of their experience in manufacturing these kinds of components.

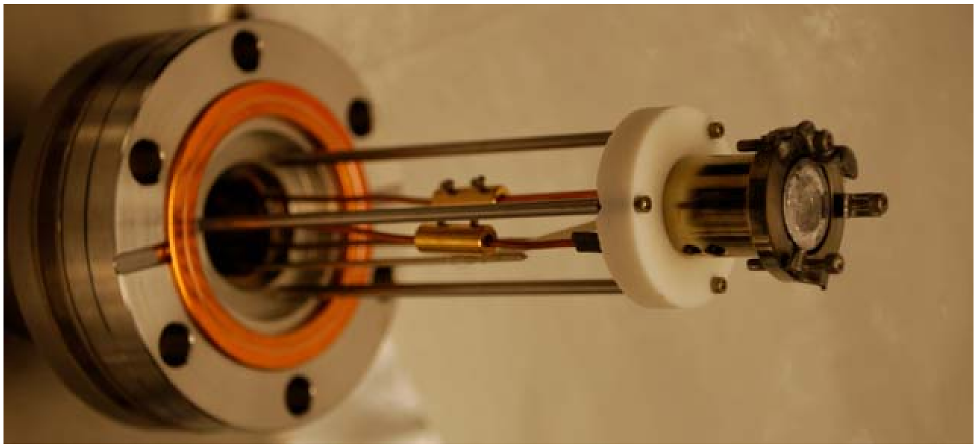

Figure 39. HeatWave Labs' heater assembly

Figure 39 shows the vacuum side of the heater with the base at left and the heater face at far right showing sample holder clips and screws in place. The back (air side) of the heater has two power connections and a type-K thermocouple connection.

D. FIRST STEPS—HEATER CALIBRATION

1. Motivation

One of the driving reasons for buying a commercially available product was to ensure that the thermocouple would give an accurate readout of the heater face temperature. When we received the Heatwave Labs unit we conducted a simple test by heating it until the heater face glowed and then compared the thermocouple temperature to the optical pyrometer temperature. During these tests, we recorded temperature differences where the pyrometer read on the order of 100°C higher than the internal thermocouple. There was an obvious disparity between the measured temperature and the heater face temperature. The logical conclusion at this point was to run a robust calibration test in order to accurately calibrate the heater's internal thermocouple temperature to the actual face temperature.

2. Experimental Setup

In order to conduct the heater calibration, we mounted the heater in a vacuum chamber with an additional thermocouple mounted to the front face. Figure 40 schematically depicts the experimental setup.

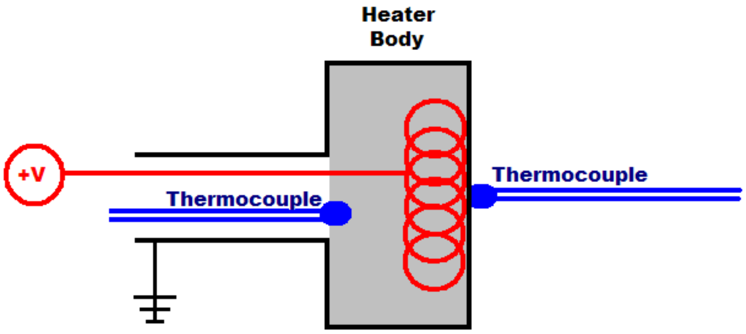

Figure 40. Heater calibration setup

The thermocouple at left is the thermocouple internal to the heater assembly, and the one providing all temperature data in future tests. The thermocouple at right accurately read the heater face temperature. The heating filament is grounded to the heater body at one end (bottom left) and connected to the supply voltage at the other end (far left). In order to avoid circuit-grounding issues we floated the face-thermocouple circuit by connecting it to a battery operated thermocouple reader.

The left picture in Figure 41 shows the actual test stand setup. The heater is mounted at front left, the face-mounted thermocouple enters the chamber from the top, a viewport is on the back side, and both the pressure gauge and turbopump port are seen at far right.

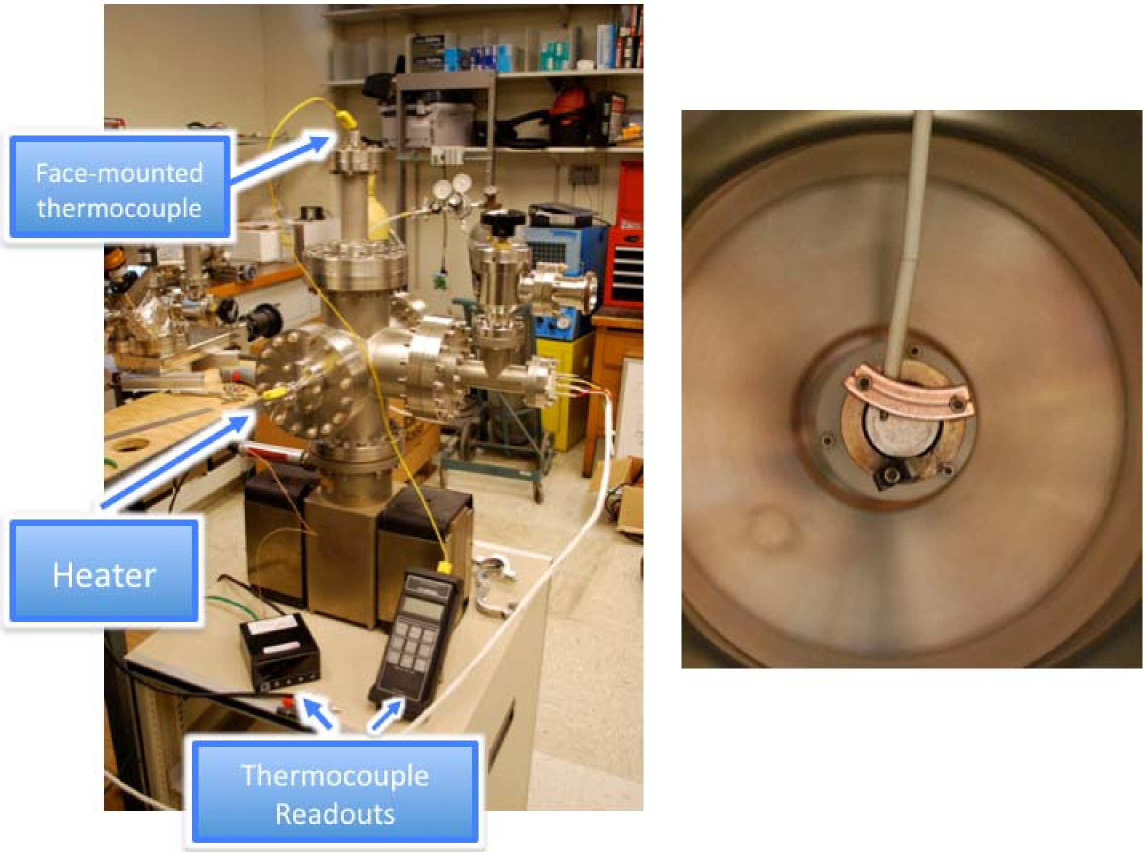

Figure 41. Photos of the heater calibration test stand

The right picture in Figure 41 shows an inside view of the chamber. The heater face is dead center with a type-K thermocouple descending from above and held against the heater face with a modified section of used conflat gasket.

The essential element of this test was to ensure good thermal contact between the thermocouple and the heater face. Convective heat transfer does not occur in vacuum, and blackbody radiation does not efficiently transfer heat at the lower temperatures we were concerned with. With conductive heating as the only appreciable mechanism to heat the face-mounted thermocouple, it was imperative to tightly secure the thermocouple onto the heater face with direct pressure.

3. Data

We ran two tests with the heater. In the first test, we applied power (via daisy-chained Variacs) in two steps and observed the temperature and time response of the heater. Figure 42 depicts this data where time references the horizontal axis and the two thermocouple temperatures reference the vertical axis.

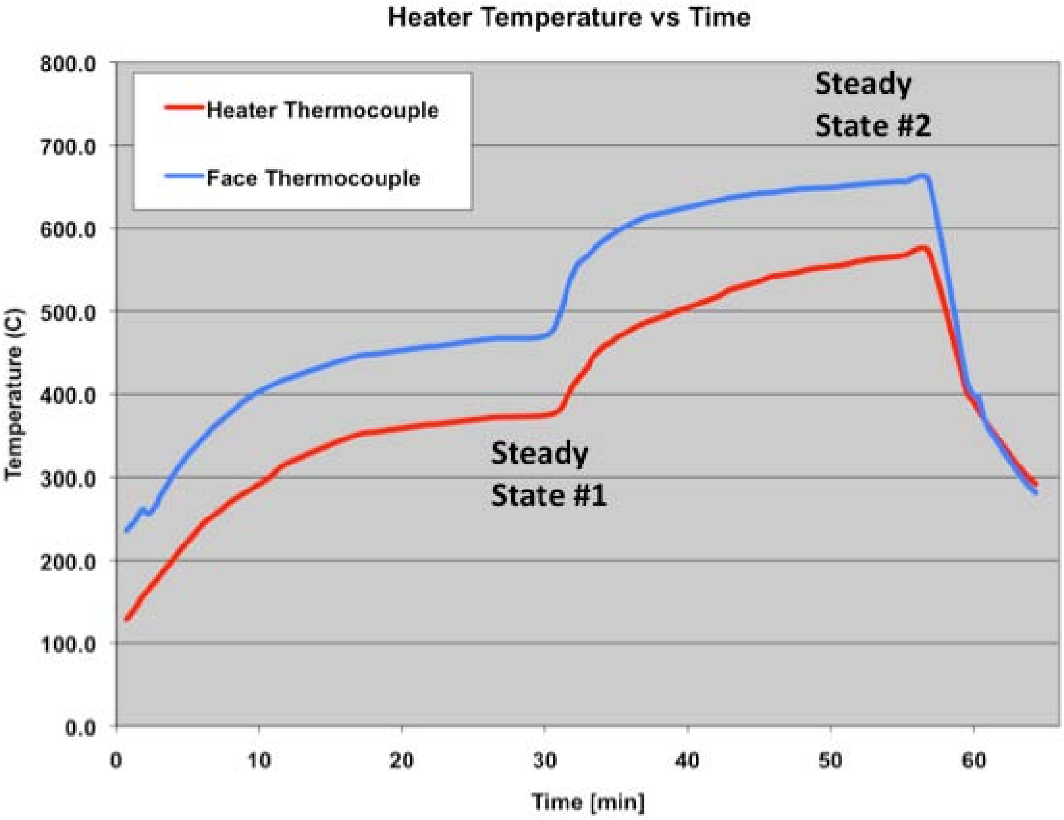

Figure 42. Heater calibration—two temperatures

The plot clearly shows a temperature difference of nearly 100°C at both steady state #1 and #2. In fact, the only time the two temperatures equaled each other was after the power was shut off—this due to the heater face being able to cool more quickly than the internal thermocouple. In order to collect a few more data points we ran a second test with a wider range of steady-state temperatures. Figure 43 shows the collected data from this second test with time on the horizontal axis and temperature on the vertical axis.

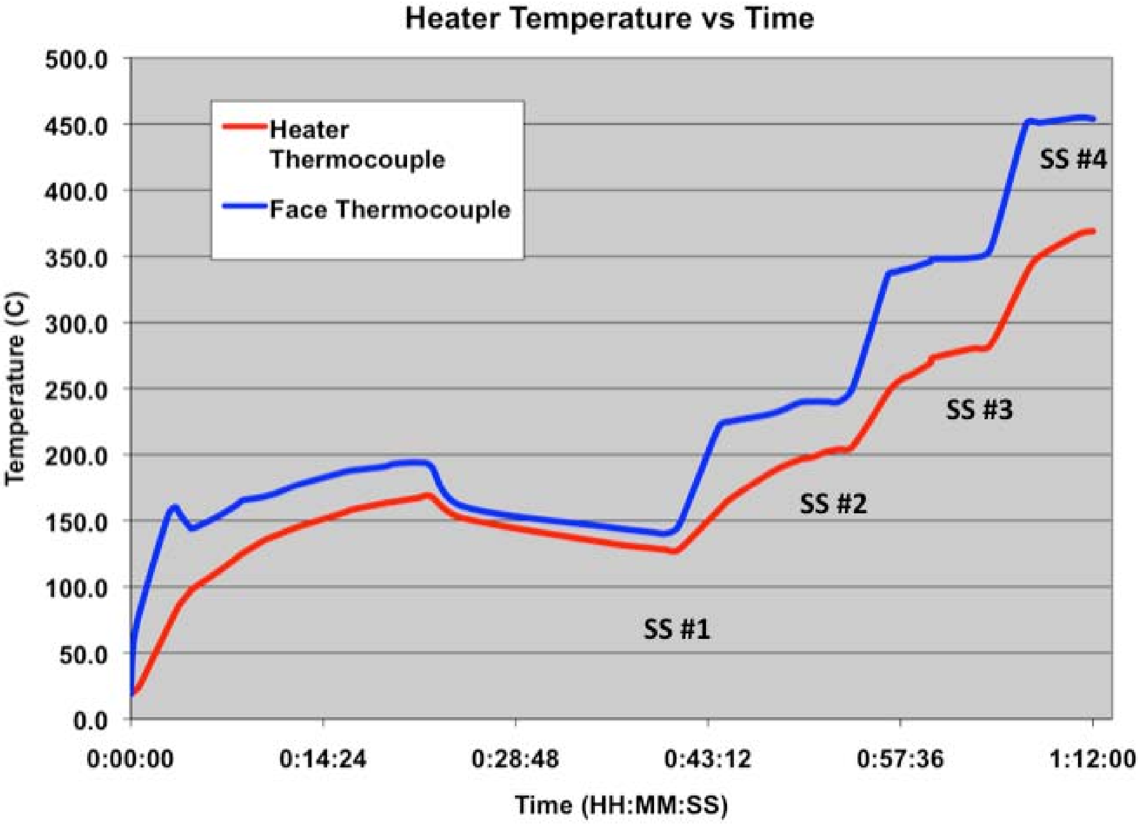

Figure 43. Gathering more data points for thermocouple correlation

Figure 44 takes the steady state points from each heating profile and plots the heater face temperature as a function of internal thermocouple temperature.

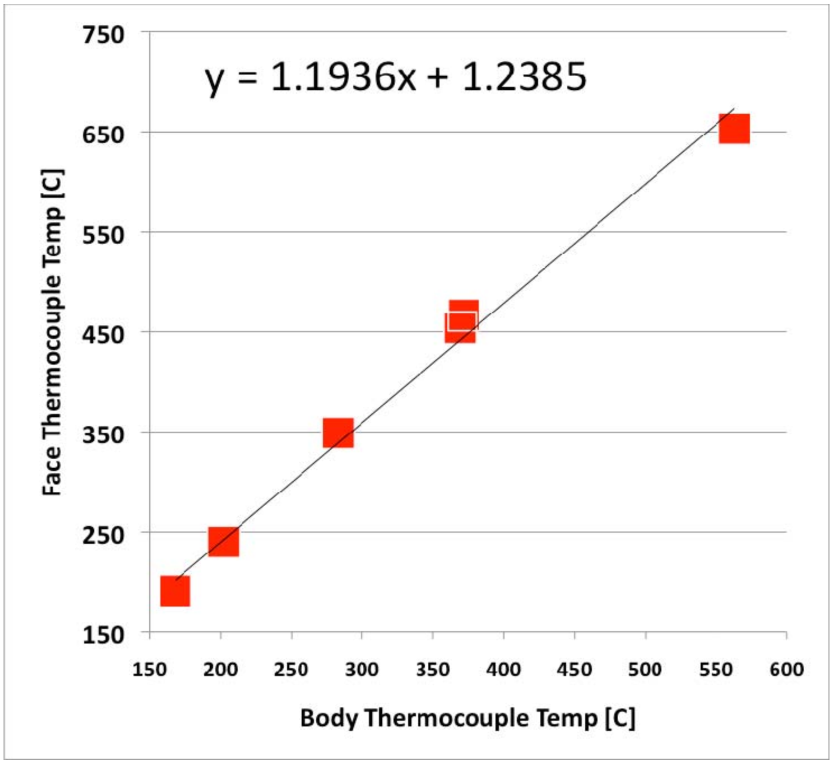

Figure 44. Correlation between indicated (body) temp and actual heater face temp

To first order, a linear fit correlates the two thermocouple readouts against each other.

4. Heater Calibration: Conclusions

We have determined an accurate correlation between the heater mount's internal thermocouple temperature and the face temperature. All other temperature data shown in this work will be calibrated to indicate heater face temperature as opposed to measured temperature. We chose to present the temperature data in this manner because other heater/thermocouple assemblies will have different temperature correlations based on their specific construction. The heater face seems a natural point of reference to which others pursuing follow-on research can easily calibrate their equipment.

E. ALVATEC CARTRIDGE EXPERIMENT

1. Motivation

As discussed in Chapter V, section B.2.b, the latest generation of dispenser photocathodes contain Alvatec cartridge cesium sources. Up to this point in the dispenser photocathode development program, nobody had observed the activation process of an Alvatec cartridge unconstrained by the dispenser cathode body. We chose to run this test first with the following goals:

a. Confirm that we could detect argon gas upon melting of the indium seal.

b. Confirm/test our ability to detect cesium deposition with the Inficon deposition monitor (QCM).

c. Test our ability to detect doubly ionized cesium with the RGA. Though cesium weighs 133AMU and is outside the direct measurement range of the RGA, doubly-ionized cesium (Cs^{+2}) should be detectable as a signal near 67AMU.

2. Experimental Layout

Figure 45 shows the relative orientation of the experimental components in the Alvatec cartridge test stand. The main body of the test chamber consisted of two, 6-way, 2-¾” conflat crosses onto which the following components were mounted:

a. SRS RGA-100

b. Quartz Crystal Deposition Monitor on a linear actuator

c. Gate valve leading to the heater/cathode assembly

d. Heater/cathode assembly. This section had its own pump port to allow its removal without having to vent the entire system to atmosphere.

e. Hot Cathode Ion Gauge (HCG)

f. Bleed-up valve (not shown in order to reduce image clutter)

g. Ion Pump

h. Viewport

i. Pumping Port

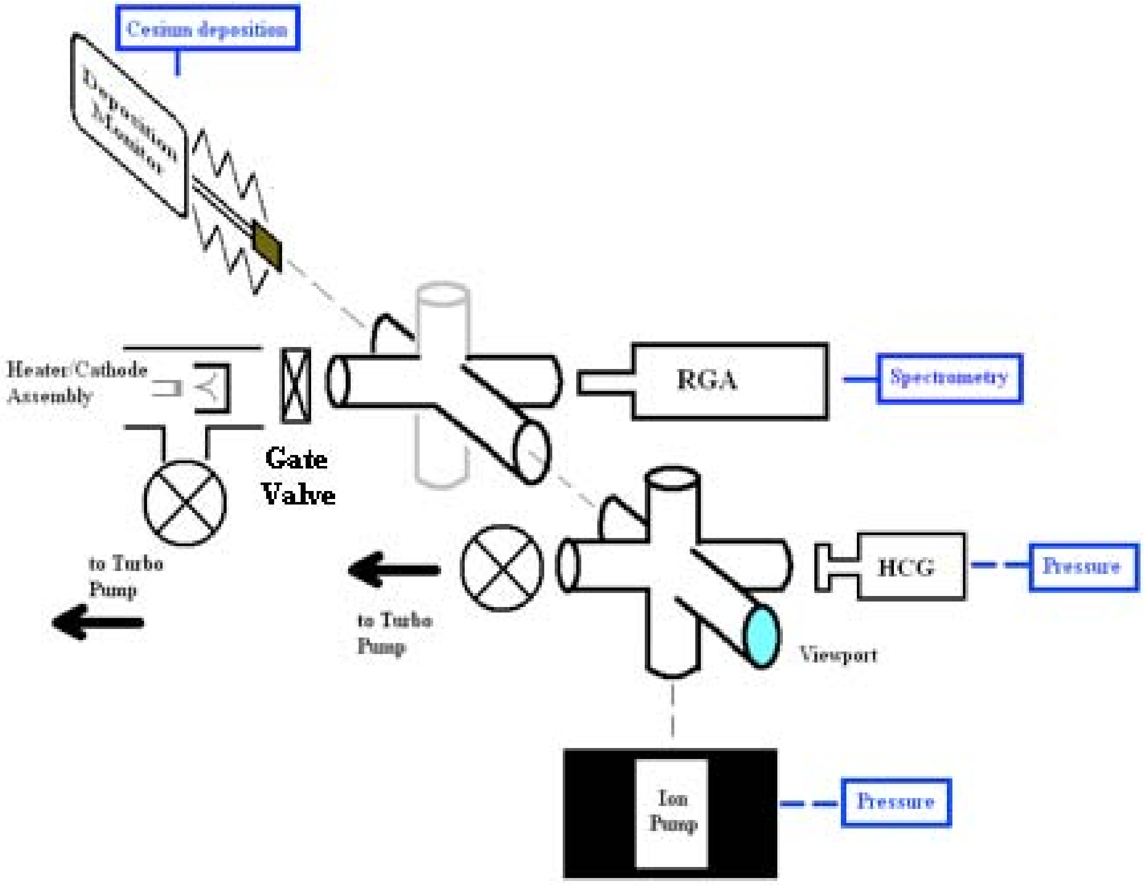

Figure 45. Alvatec Cartridge Test Stand Layout

3. Data

We activated the first Alvatec cartridge on 24 March 2010. With concerns about exposing the ion pump to argon gas, we ran the entirety of the test under active turbopumping. The test started by gently heating the cartridge to 180°C. The goal at this point was to see if we could detect the release of argon gas with the RGA thereby signaling the melting of the indium seal. Figure 46 depicts the experiment history with temperature and pressure plotted versus time.

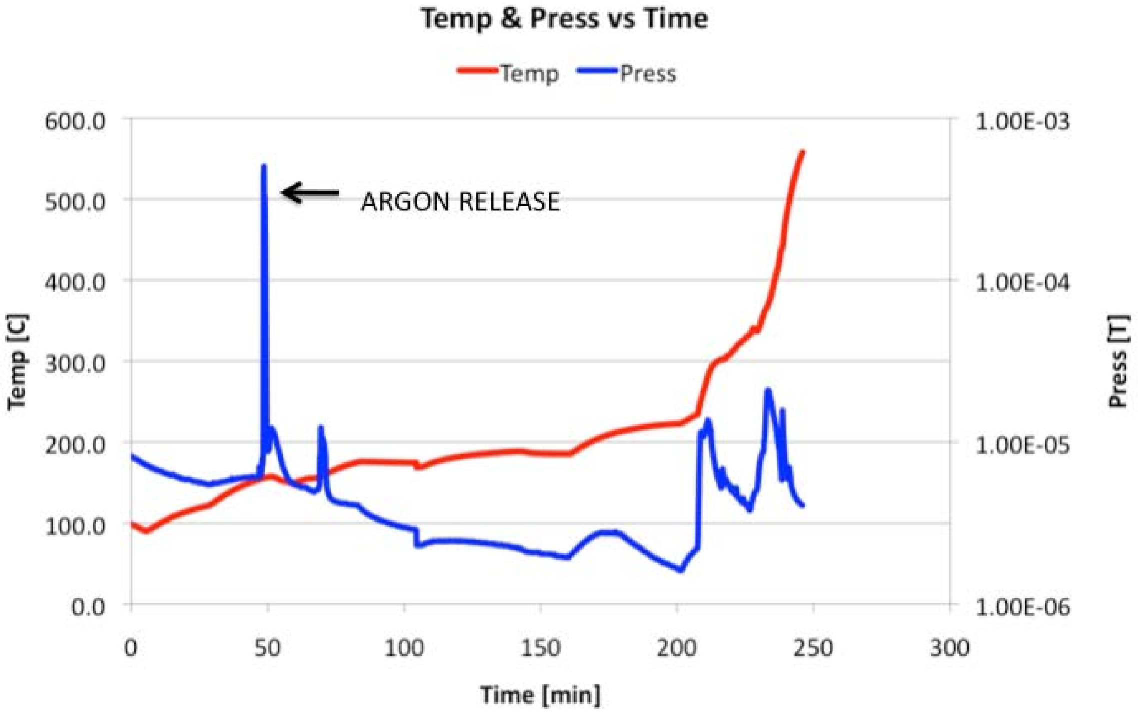

Figure 46. First Alvatec cartridge activation

The first major pressure spike occurs at 50 minutes and 160°C. The RGA scan showed that argon was the main constituent of this spike, thus confirming the melting of the indium seal. After the indium seal melted, we noted a general decrease in total vacuum pressure below what the turbopump could maintain. These two facts, the argon spike and pressure drop, helped confirm the release of cesium since cesium acts as a 'getter' when in a vacuum. Getter pumping is a long established vacuum pumping process by which a reactive metal (such as cesium) is allowed to react with chemically active gasses to form low vapor pressure compounds. Once reacted, these compounds readily stick to the vacuum chamber wall, thus reducing the overall system pressure [56]. We regularly used this effect throughout the course of our experiments to determine if free cesium was or was not being emitted from the various test samples.

Figure 47 shows the temperature and QCM reading from the beginning to end of the experiment. Temperature references the left axis while QCM thickness references the right axis in angstroms.

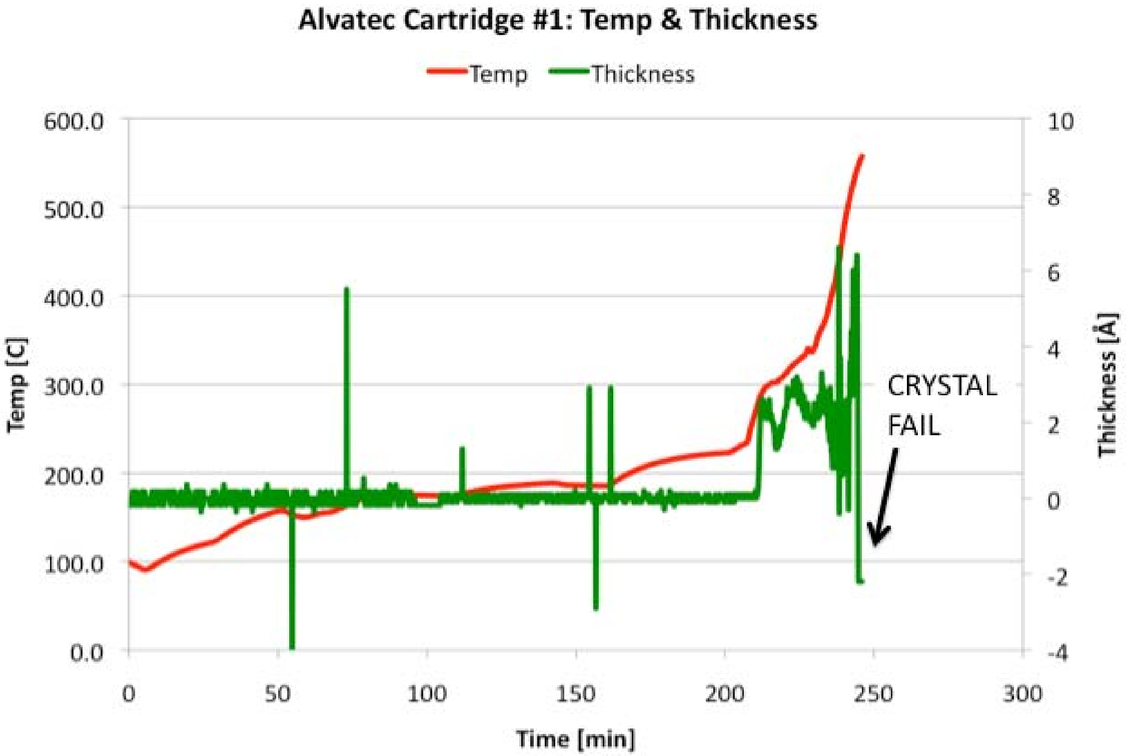

Figure 47. QCM history during activation of 1st Alvatec cartridge

The QCM remained inserted for the entirety of this test. After seeing zero deposition up to 220°C, we rapidly increased the temperature past 500°C. Above 220°C we started recording an output, but the rapid fluctuations made us suspect either the sensor or software was not working properly. At 246 minutes, the QCM readout flat-lined at -2Å and the software gave a “CRYSTAL FAIL” indication. We ceased the experiment at 248 minutes to investigate the cause of failure. Our post-test analysis suggests these spikes were caused by bursts of Cs:Bi compound from the Alvatec cartridge. Figure 48 shows two photos taken in our post-test inspection.

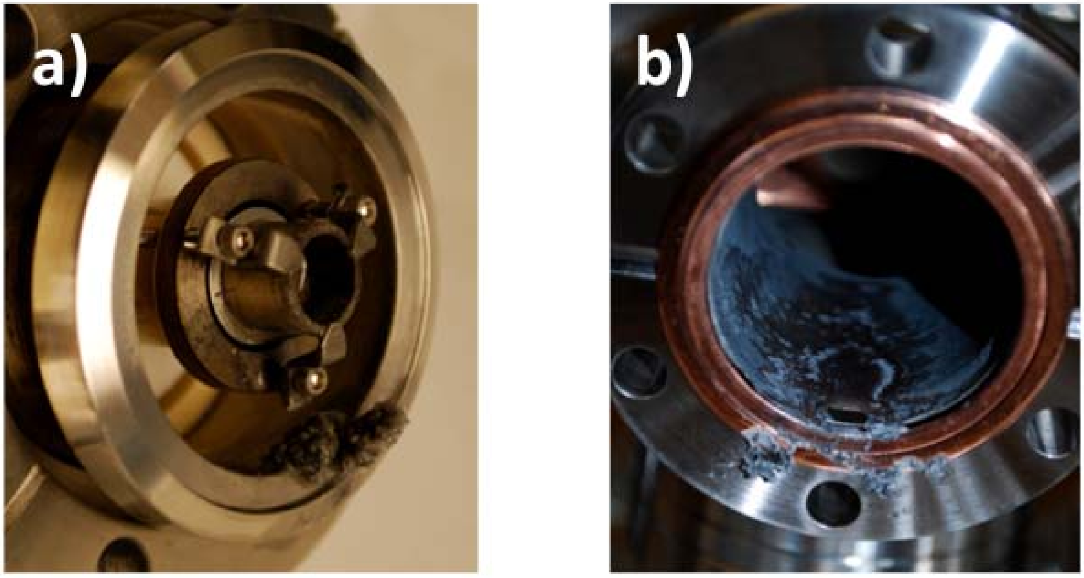

Figure 48. The heater and cartridge area after the 1st Alvatec cartridge activation

Figure 48a) shows the Alvatec cartridge and heater assembly. We observed that the cartridge was mostly emptied of Cs:Bi compound. A solidified puddle of material can be seen below the heater mount on the edge of the pipe flange. This deposit was ostensibly melted indium, but also contained bits of bismuth and oxidized cesium. The melted indium also soldered the Alvatec cartridge to the heater assembly. Thankfully, indium is a soft metal. A concerted effort utilizing scalpels and a soldering iron eventually freed the two components from each other. Figure 48b) shows the opposing flange to which the heater assembly was mounted. That entire section of vacuum tube required extensive cleaning with alcohol and Kimwipes to remove the encrusted debris.

Figure 49 shows two pictures of the QCM assembly after the test. Picture (a) on the left shows the QCM once removed from the vacuum system. The crystal in this photo is coated with a black sooty substance—the crystal started the test as a smooth matte gold surface.

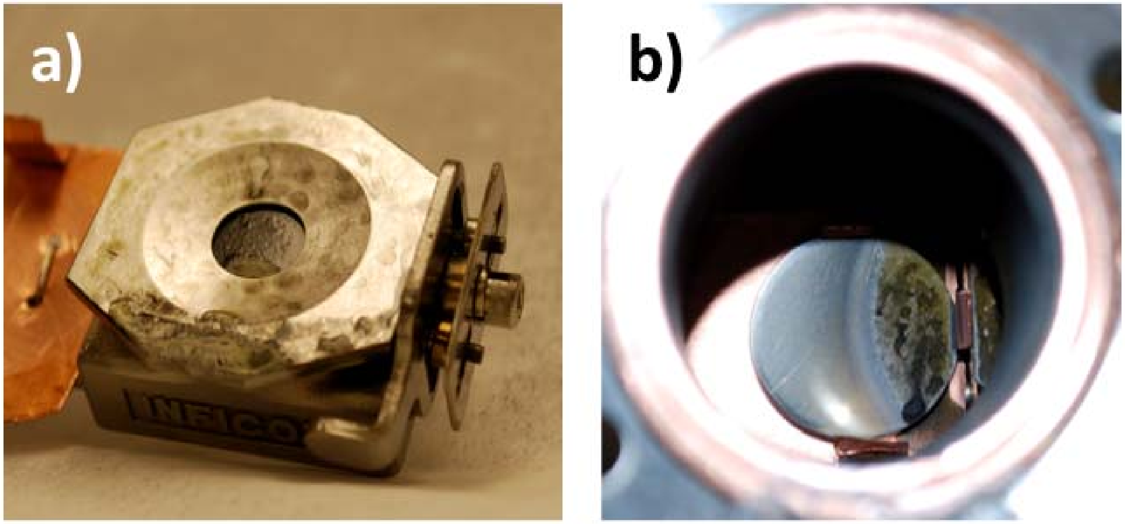

Figure 49. QCM after 1st Alvatec cartridge activation

Picture (b), on the right, shows a view inside the test chamber before removing the QCM assembly. The QCM sensor is shifted to the right from its position during the test and thus not visible in this picture. The round metal surface seen at center is a niobium coin we intended to use as a sample for later spectroscopic examination. The outcome of this test rendered the sample unsuitable for spectroscopy, but the picture is still interesting in its own right. During this first test, the coin was half shadowed by the vacuum pipe wall, and that shadow is evident by the crescent pattern of deposited material that boiled off the Alvatec cartridge and onto the sample.

In our post-test analysis, we discovered that we had installed the QCM crystal backwards—leading to our inability to record a useful output from the sensor. We rectified that error by correctly orienting the fresh replacement crystal. We installed the second Alvatec cartridge and started the same heating sequence as before.

After cleaning the vacuum components and replacing the used QCM crystal with a new crystal, we subjected the second Alvatec cartridge to similar, but less aggressive, heating profile. Figure 50 shows the temperature and pressure history of this test.

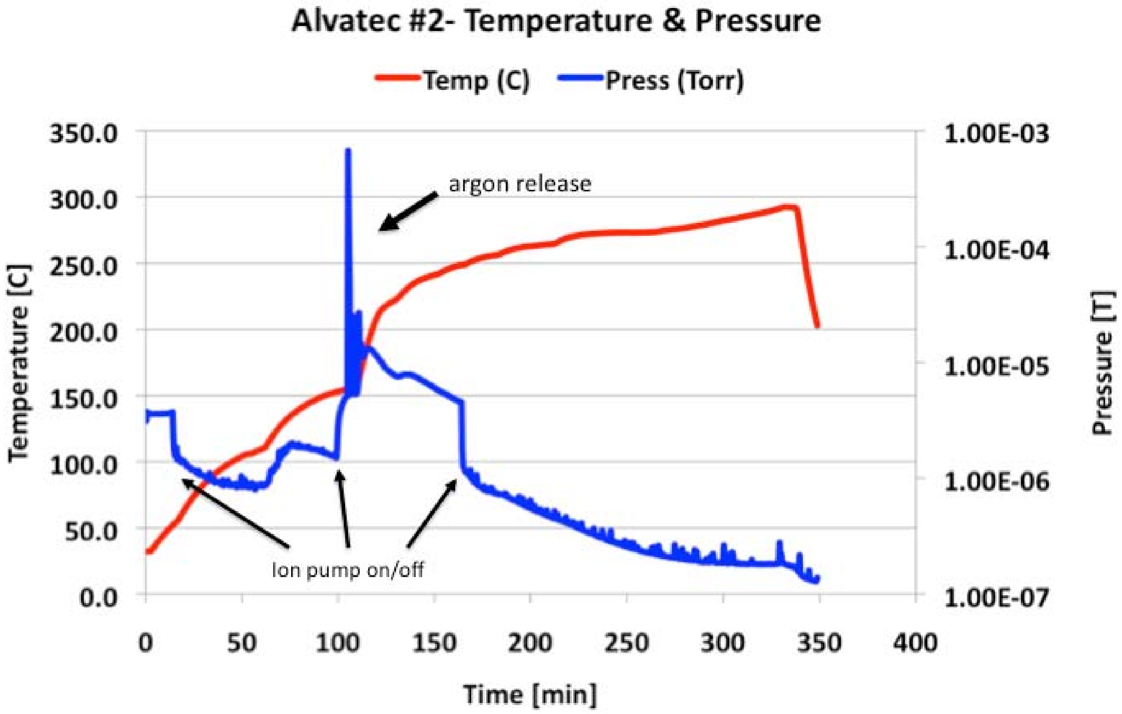

Figure 50. Alvatec 2 activation temperature and pressure profile

After recording an argon spike (activation) at 152°C, we heated the sample more gradually to 292°C over the next 240 minutes (4 hours). During this test we also elected to activate the ion pump in an attempt to improve the vacuum. The points where the ion pump was turned on and off are noted in the figure and account for the respective drops and rises in pressure.

At 270 minutes, we retracted the QCM and created an open line-of-sight between the RGA head and the Alvatec cartridge. Figure 51 shows the RGA scan prior to and immediately following QCM retraction.

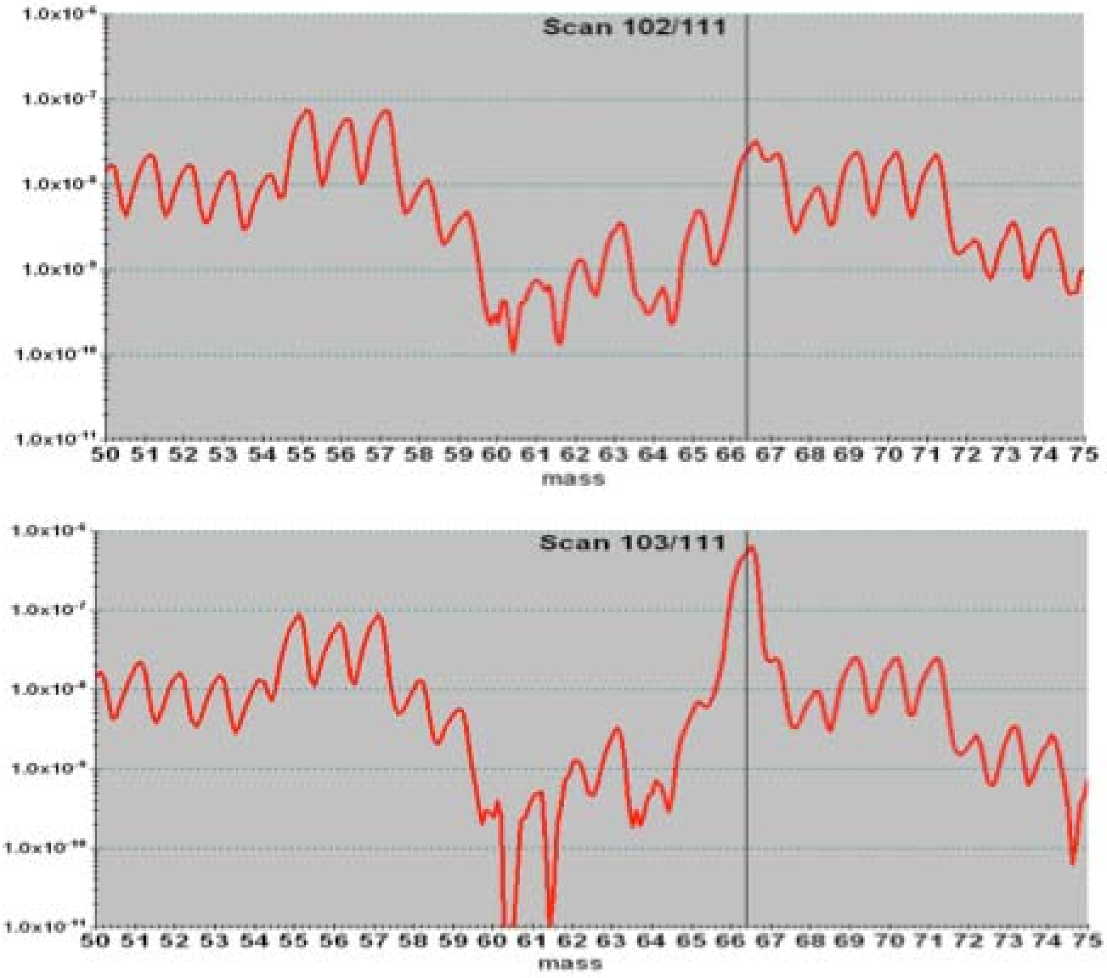

Figure 51. RGA scans showing double ionization of cesium

Both RGA scans show pressure plotted against the vertical axis (1×10^{-11} up to 1×10^{-6} Torr) and molecular masses 50 to 75. The RGA shows molecular mass 66.5 rising from 3×10^{-8} Torr in scan 102 to 6×10^{-7} Torr in scan 103. This is the indication of Cs^{+2} we anticipated. This spike subsequently subsided when we returned the QCM to its original position between the test sample and RGA head.

Figure 52 shows the QCM data history during the test. The test continued until 350 elapsed time at which point the LabView QCM interface registered another 'CRYSTAL FAIL,' as noted in the figure.

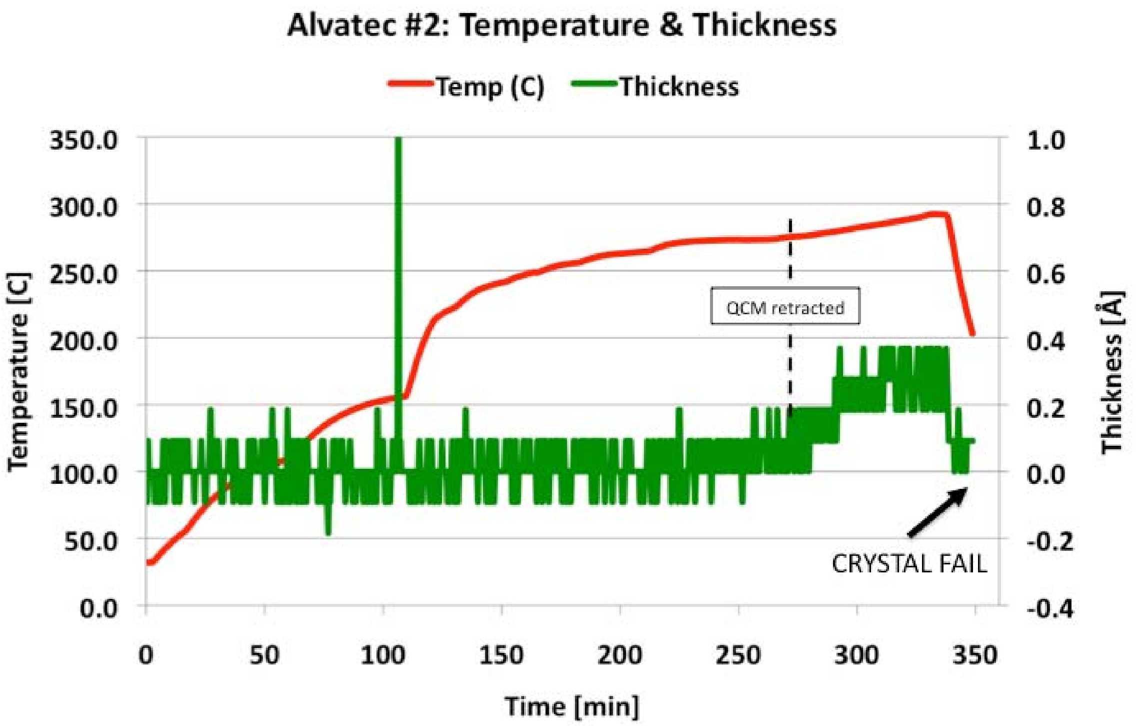

Figure 52. QCM output during second Alvatec heating test

Unlike the first Alvatec cartridge test, we recorded no significant signal of any kind (maximum 0.4±0.1 Å) before crystal failure. After rectifying the hardware issue discovered after the first Alvatec cartridge test, we suspected issues still remained with our software interface between the computer and the QCM. Further testing, as outlined in section F, would clarify the matter.

4. Alvatec Cartridge Activation—Conclusions

Activation of these two Alvatec cartridges provided us with the following insights:

a. We could reliably detect cartridge activation via the release of argon gas. This activation occurred near 157°C on both tests—verifying the proper calibration of the heater.

b. LabView was not interfacing properly with the QCM. Before progressing with the testing of a cesium dispenser cathode, we would have to diagnose this issue and confirm that we could accurately record particle deposition.

c. The RGA is capable of detecting doubly ionized cesium when given an open line-of-sight with the source. When otherwise obscured, the cesium did not make it to the RGA head, but would rather deposit on the vacuum chamber wall.

F. DEPOSITION MONITOR TROUBLESHOOTING—ALUMINUM DEPOSITION TEST

1. Motivation

History gives us evidence that even the earliest researchers faced difficulties implementing new devices.

Figure 53. Early physicists troubleshooting their equipment

Difficulties collecting deposition data in the Alvatec experiment, interface difficulties between the QCM and LabView, and the realization that the dispenser cathodes’ behavior was an unknown drove us to find a means of verifying the proper operation of the QCM data collection interface by collecting data from a known deposition source before attempting to do so from an unknown source.

To that end, we chose to run a deposition test using aluminum as our evaporative source. Aluminum is a commonly used material in physical vapor deposition processes. It is inexpensive, safe to handle, and melts at a reasonably achievable 660°C. Before discussing the experiment, we will briefly touch on a bit of PVD theory.

2. Physical Vapor Deposition—A Brief Introduction

Physical vapor deposition (PVD) is a general term used to describe any number of methods used to deposit thin films of material on an object by the vaporization and subsequent condensation of one material onto another. This practice is commonly used in the manufacture of semiconductors, aluminized films for plastic food bags, and plated tools among other things.

One of the necessary steps in PVD is to create a vacuum such that the particles evaporating from the source have a high chance of making it to their intended target. In physics, we refer to the mean free path, *l*, as the distance one small particle travels before colliding with another small particle (evaporated source material and gas molecules in the present case). We need to estimate *l* for particles and gas molecules in order to verify that we have a sufficiently good vacuum to practice PVD. If the vacuum is too poor, evaporated particles will get deflected by collisions with gas molecules and not arrive at their intended destination.

We shall use the method outlined by D.L Smith in his book, *Thin-Film Deposition: Principles and Practice*, to calculate *l* for aluminum. Imagine a molecular particle generated for vapor deposition passing perpendicular (into the page) through an array of interfering gas molecules as seen in Figure 54(b). The collision diameter is the diameter at which the source particle either is, or is not, deflected by an interfering molecule. A simple means of accounting for the size of both the source particle and blocking molecule is to define the collision diameter as *2a*, as seen in the figure. For a given gas concentration, the total collision area, σ_m, per cm^2 and per cm of distance travelled is the sum total of area projected by the gas molecules with collision diameter 2a. This is an approximation because σ_m also depends on the kinetic energy of the particles involved, but the approximation is sufficient for the situation at hand.

Figure 54. Geometry used in derivation of Equation 4 (From [57])

After a few more steps, we arrive at the following equation for the mean free path of aluminum atoms in a vacuum:

$$l_{AL} = 1/(\sqrt{2}\,\pi\, a^2\, n) \qquad [4]$$

a is the diameter of the particle and n is the concentration of atoms per m^3, as found from the ideal gas law. The diameter of aluminum is ~0.3nm which happens to be the nominal size of most gas molecules [58][57]. Figure 55 shows the mean free path of aluminum calculated for vacuums ranging from 10^{-2} Torr down to 10^{-6} Torr.

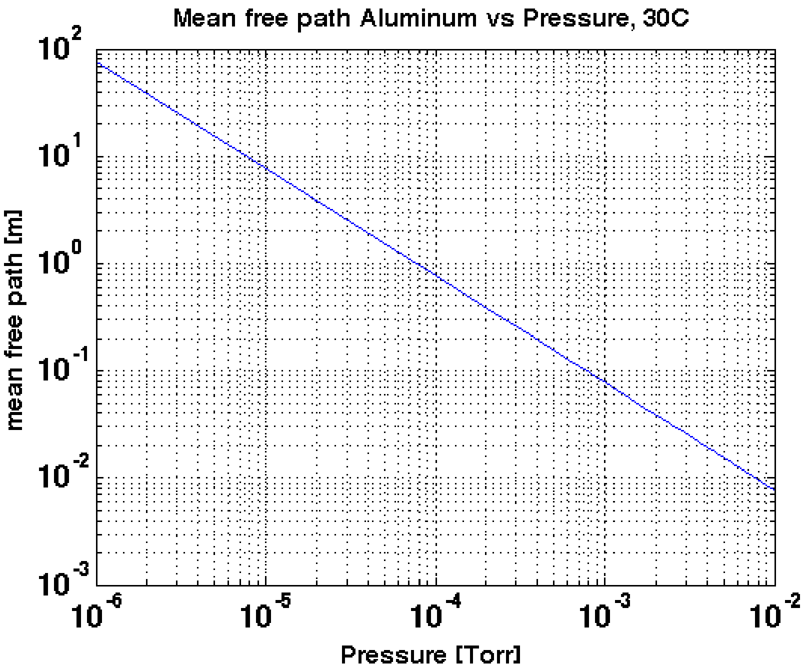

Figure 55. Charting the mean free path of aluminum at various pressures

The distance between our heater element and the deposition monitor is nominally 12cm and the temperature will be far in excess of 30°C (which increases *l*), we can conclude that a vacuum less than 5x10^{-4} Torr should be more than sufficient to allow the majority of aluminum particles to travel unimpeded between the source and the QCM.

3. Experimental Setup

The experimental configuration used in this test is shown in Figure 56.

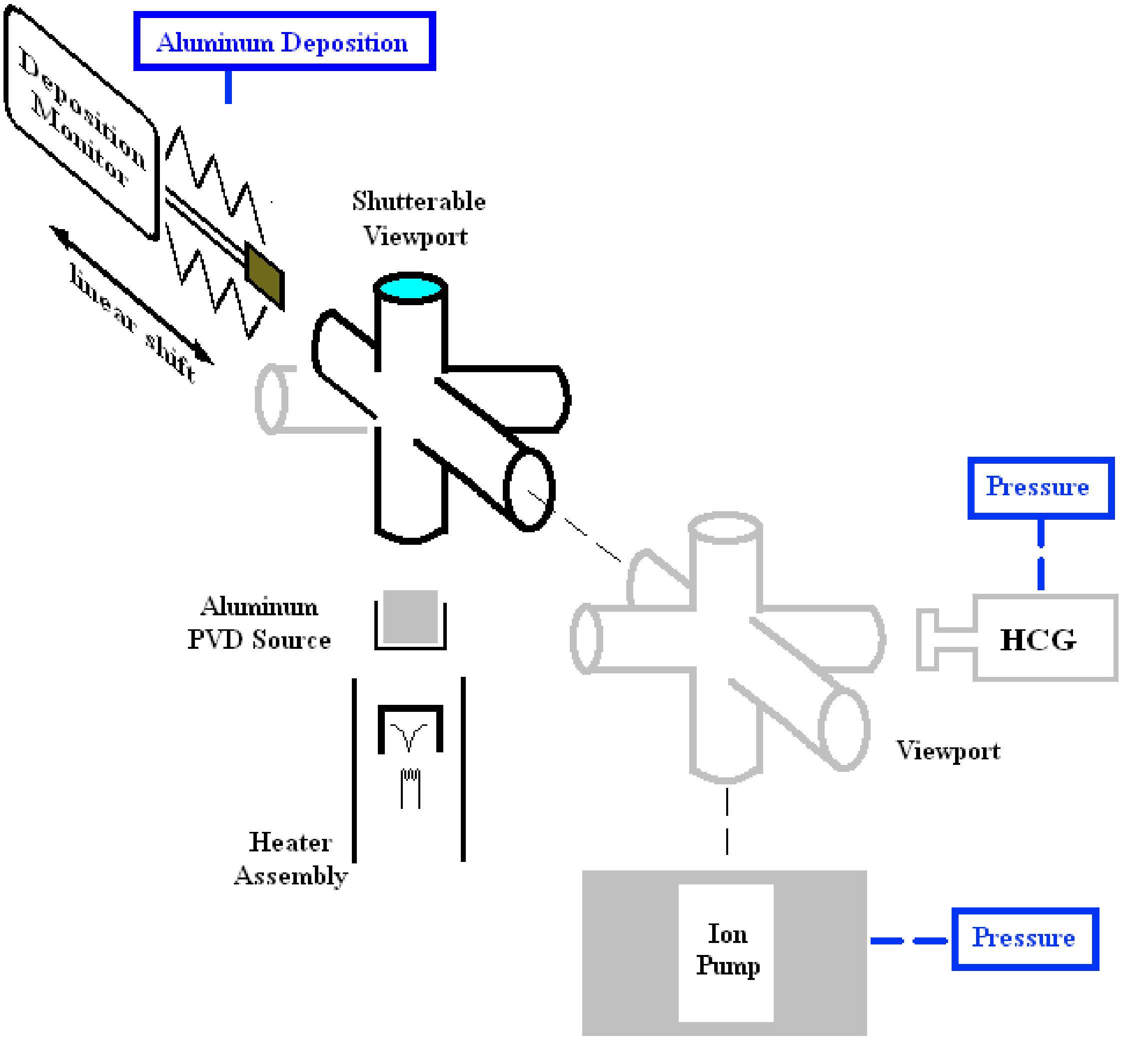

Figure 56. Aluminum vapor deposition test stand configuration

We chose a vertical orientation for the heater assembly and crucible in order to prevent the molten aluminum from flowing out of the crucible. We also wanted to observe the process with our eyes, so we removed the RGA and installed a shutterable viewport. The shutter was necessary to limit the glass' exposure to evaporating aluminum. It is not hard to turn a window into a mirror through PVD, and we wanted to avoid this possibility. Plasmaterials (www.plasmaterials.com) generously supplied us with several aluminum pellets free of charge. These samples were 99.999% pure aluminum, about the size of a pencil eraser, specifically engineered for PVD processes. The last component of the experiment we required was a crucible for containing the melted material. Lacking a proper PVD crucible, we created our own by cleaning the bismuth remnants out of the first Alvatec cartridge.

After the difficulties encountered interfacing the QCM with LabView in the Alvatec experiments, we decided to use the stand-alone software package Inficon provides with its thin film deposition monitors. By doing so, we removed the possibility that a LabView interface error would hinder data collection.

4. Data

We successfully melted the pellet and recorded deposition on the QCM run by the Inficon software package. Figure 57 shows the pellet mounted in its crucible before and after the PVD test.

Figure 57. Aluminum sample before and after vapor deposition

The QCM deposition data and heater temperature history are shown in Figure 58. Heater temperature, in red, references the left vertical axis and QCM thickness, in green, references the right axis.

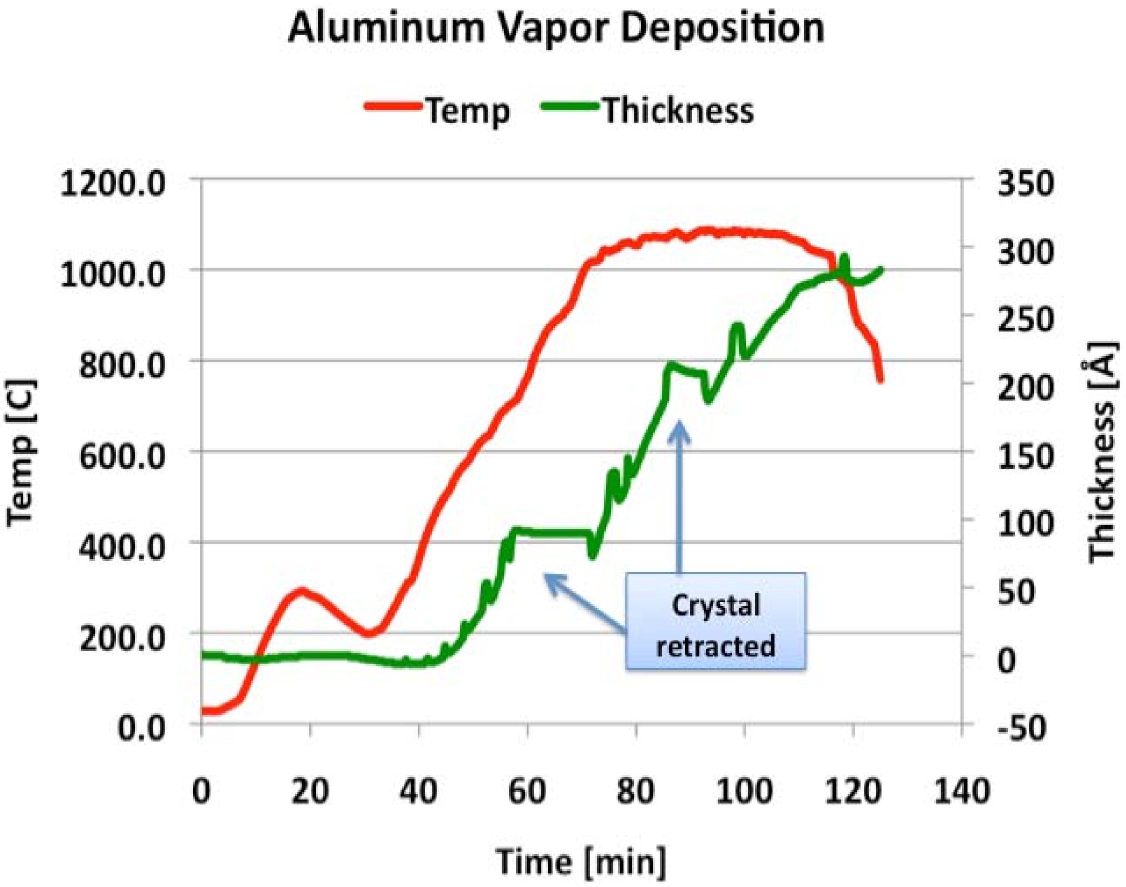

Figure 58. QCM data from the aluminum PVD test

In the plot, we notice an intermittent series of spikes in QCM thickness. These spikes were caused as we retracted the QCM in order to visually observe the heater and sample. These spikes are on the order of 25Å, the same as observed in the rapid thermal unload from the radiant heating test, and smaller by an order of magnitude in comparison to the deposition signal. In order to reduce visual clutter, only the two lengthiest QCM retraction periods are annotated on the figure. Every time we retracted the QCM, we noticed a jump in thickness on the order of 20Å. We also noticed that, for the two lengthy periods of QCM retraction, the thickness reading did not drift more than 5Å from the initial shifted value. Finally, when the QCM was reinserted into the deposition path the thickness reading immediately shifted back to the recorded value prior to retraction. In order to understand this transient behavior more completely, we decided to run a radiant heating test with no deposition source in order to observe just how the radiated heat from the heater module was influencing our data. This test will be discussed in the next section (Chapter V, section G).

Along with learning something of the QCM behavior, perhaps a more interesting observation is that the QCM starts recording deposition at approximately 475°C—below the 660°C melting point of aluminum. This is no error, but rather a reminder of the fact that the heater assembly was contaminated with melted indium from the Alvatec cartridge experiments. We observed indium melted in the crevices of the heater assembly after the first two Alvatec cartridge experiments. During those tests, indium flowed off the cartridge face and into the gap between the heater and the heat shield. This gap is noticeable in Figures 41 and 48. We did not anticipate the later re-emission of indium into the vacuum, but given that aluminum could not possibly be a deposition source until it melted at 660°C this must be the case. Regardless of the source material being aluminum or indium, we achieved our goal of recording vapor deposition with the QCM.

5. Vapor Deposition Experimental Conclusions

a. We successfully recorded vapor deposition on the QCM using the software provided by Inficon. The remainder of our experiments would utilize this software package, while temperature and pressure history were recorded with LabView.

b. There are transients in the QCM data as the crystal is removed from the heater's line of sight. These transient effects must be examined in order to gain a better understanding of the data output.

G. QCM RADIANT HEATING TEST

1. Motivation

We had successfully debugged the QCM hardware and software at this point. However, the deposition test demonstrated a need to understand how radiant heating would alter the QCM output. The literature accompanying the Inficon deposition monitor recommends mounting the sensor between 10 and 12 inches from a deposition source. The reason for this, according to their technical support staff, was that mounting the sensor any closer than 10 inches could cause a crystal malfunction and data output error due to radiant heating effects—this we had observed, and now needed to better understand [59].

The reason for placing the QCM 5 inches from the heater assembly versus the manufacturer recommended 10 inches was motivated by our lack of knowledge concerning the actual evaporation rate of cesium off the dispenser photocathodes. We wanted to give the QCM the greatest chance possible of detecting evaporated cesium. As such, we placed it as close to the dispenser cathode as possible so that it would intercept the greatest solid angle area of evaporating material.

2. Experimental Setup

We used the same experimental configuration for this test as that used in the Alvatec cartridge test (Figure 45). The only difference between this test and the cartridge tests was that we did not load a sample onto the heater face. As stated before, the heater face was positioned line of sight to the QCM at a distance of 5 inches (12 cm).

3. Data

The test essentially consisted of a steady ramp up to 200°C, hold for 10 minutes, and then another ramp up to 520°C with another ~10 minute hold. Figure 59 plots temperature and QCM history against time for this test. Temperature is in red and references the left vertical axis. QCM thickness is plotted in green and references the right axis.

The temperature makes a sharp dip down at 48 minutes caused by a temperamental open-circuit fault in the heater element. After rectifying the fault with a gentle wrench tap to the vacuum pipe, we continued heating until we reached a steady state of 530°C. The QCM was directly line of sight with the heater element for the entire test up to the 67-minute mark. At 67 minutes we caused a rapid thermal unloading of the

QCM by retracting it into the side-pipe of the 6-way cross. The sudden withdrawal from a heat source caused an instant change in the QCM readout, as seen in the figure.

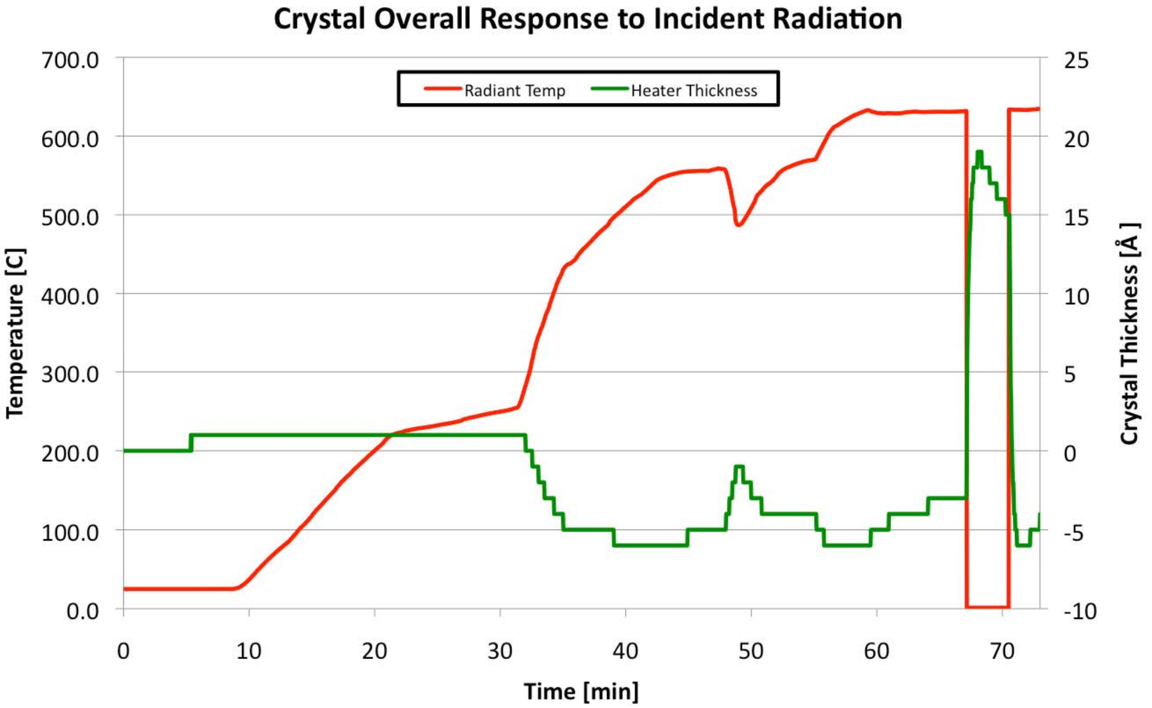

Figure 59. QCM response to radiant heat

What can we learn from this data? We see essentially zero deviation in the QCM reading for heater temperatures up to 230°C. As temperatures increase above 230°C the readout descends to -6Å, but goes no lower even as temperatures increase beyond those intended for all our following experiments. That -6Å deviation holds fairly constant until the heater open-circuit fault that allowed the sensor to cool, at which point there is a slight increase in indicated thickness. The same effect is even more dramatic when we retract (thus rapidly cool) the sensor. Figure 60 expands the time scale around 70 minutes to show the rapid thermal transients in greater detail.

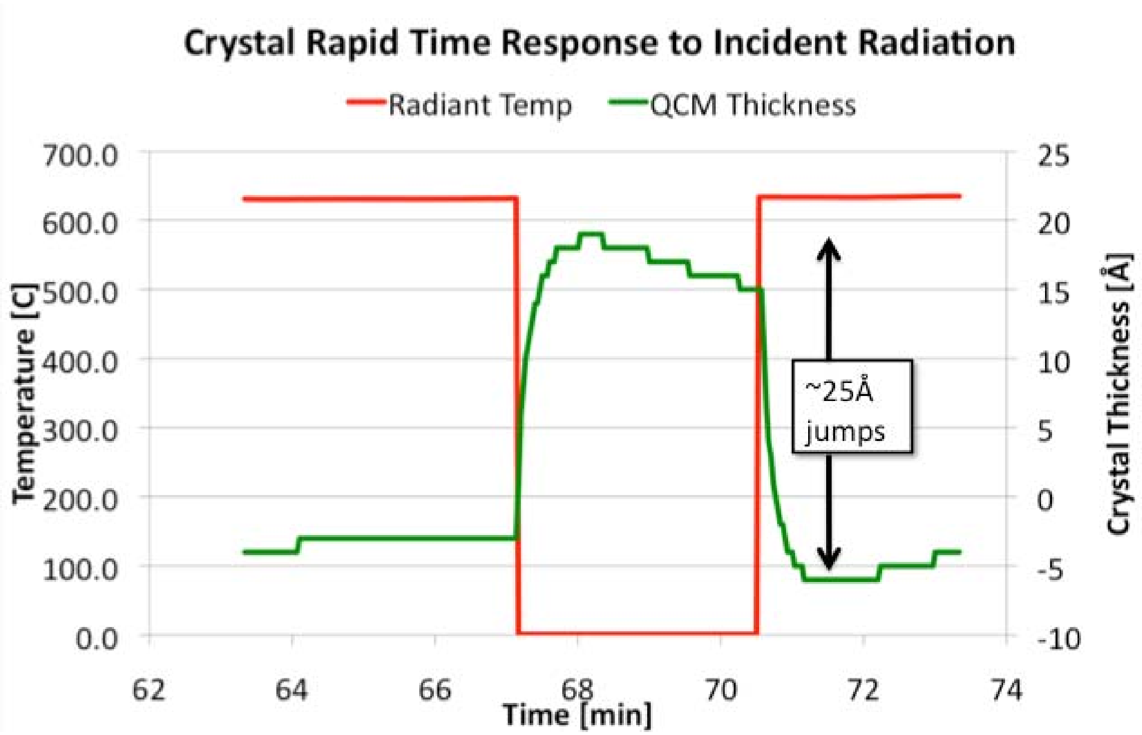

Figure 60. QCM rapid time response to incident radiation

It is interesting to note that there seems to be some kind of decay effect after the rapid jump and subsequent drop in thickness readings. We observed this same effect in the aluminum deposition data as seen originally in Figure 58. The second noted period of QCM retraction from the aluminum deposition test is shown in greater detail in Figure 61. One can easily discern this same manner of decay from the initial deviation value.

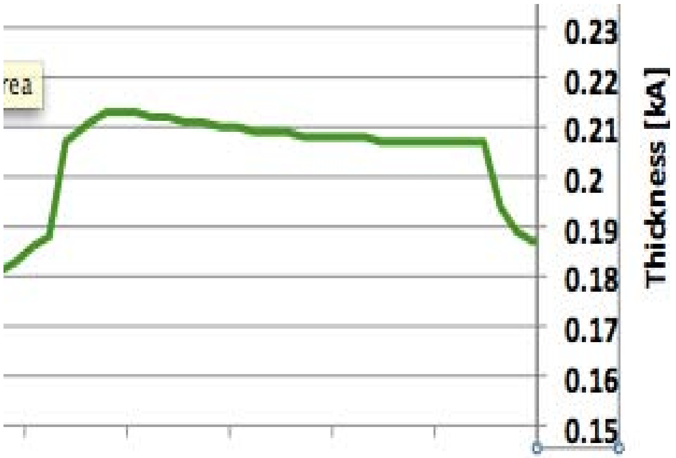

Figure 61. Second QCM retraction period during aluminum deposition test

The figure shows this effect to be minimal, on the order of 5Å. This is approximately one monolayer of cesium—not an appreciable error.

4. Conclusions

In numbered form, this test provides us with the following conclusions:

a. There is a correlation between QCM temperature and thickness reading. In general, the steady state error above 230°C was on the order of -5Å, and did not scale linearly with temperature, or in any other discernable manner, up to 530°C.

b. Thermal unloads cause jumps of approximately 25Å with a nominal 5Å decay thereafter. Re-exposing the QCM to the same radiant heat restored the previous measurement. Therefore, though we should expect to see jumps in thickness during future tests as we move the QCM out of the heater line-of-sight, restoring the QCM to its previous position should return the readout to its previous value, plus or minus 5Å.

c. As long at the QCM temperature is constant, deposition rate data should be accurate, even if the actual thickness is shifted by -5Å.

d. Deposition data from the aluminum deposition test reinforces our understanding about the QCM behavior when removed, then reinserted, into the radiant path of the heater. We can reasonably predict that actual QCM thickness will be somewhere between the recorded value and +6Å from that during periods of thermal stability at temperatures up to 530°C.

H. TITANIUM:CESIUM CHROMATE PHOTOCATHODE CESIUM EVAPORATION TEST

Before diving into the details of the dispenser photocathode experiment, let us quickly summarize our journey so far. First, we characterized the performance of the heater assembly. Second, we confirmed the ability of our RGA to detect argon as well as cesium (if only in a qualitative sense) during the Alvatec cartridge tests. Third, we confirmed the proper operation of the QCM via aluminum/indium vapor deposition. Lastly, we gained a semi-quantitative understanding of the QCM's response to radiant heating.

The ultimate goal of this experiment was to gain an understanding of how the dispenser photocathode may influence the FEL system as a whole by cesium contamination. With the aforementioned tasks completed, we were finally ready to test our first dispenser photocathode with confidence that our experimental equipment and processes were reliable.

1. Experimental Setup

Figure 62 shows the relative orientation of the experimental components in the dispenser photocathode test stand. This configuration is the same as that used for the Alvatec cartridge tests (Figure 45).

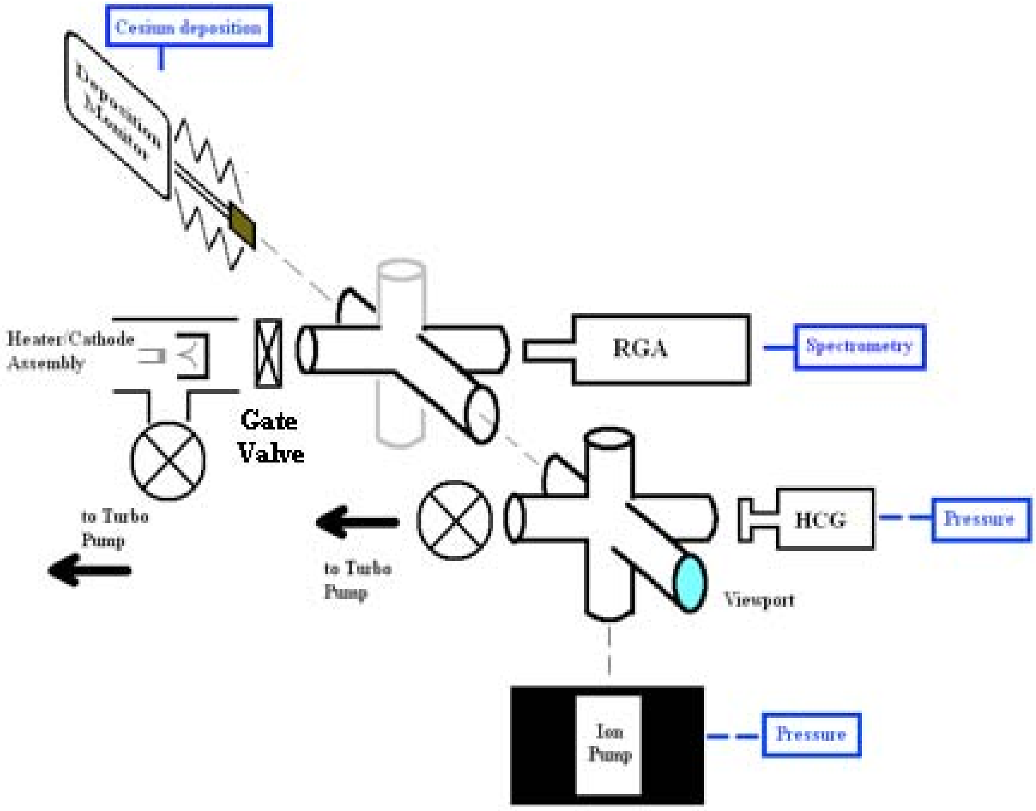

Figure 62. Ti:cesium chromate dispenser photocathode test stand configuration

The first dispenser had a titanium:cesium chromate (Ti:$CrCs_2O_4$) source. The dispenser measured ½” dia. by ½” long and had an activation temperature of approximately 475°C. Having a pressed pellet source meant that it was not argon packed, and previous experiences with these cartridges showed some reliability issues when it came to activation [60]. One way to confirm successful activation would be to monitor the QE of the cathode during the activation process, as done at the University of Maryland [20]. Our experimental setup allowed us three means of detecting cesium release: QCM deposition, RGA double ionization, and post-activation spectroscopic examination of the dispenser’s tungsten surface. These methods provide important complementary information regarding the state of the vacuum environment (cathode and vacuum chamber) that QE monitoring alone cannot provide.

2. Activation of Ti:Cs Chromate Dispenser Photocathode

As in the Alvatec experiments, we chose to actively turbopump during this test. Though not worried about argon gas entering the ion pump, the dispenser and heater assembly outgassed sufficiently that we chose to turbopump rather than exhaust our ion pump. Figure 63 shows the temperature and pressure history of this test. We started the activation process by steadily bringing the cathode up to 400°C. At 300°C we encountered the same heater open circuit fault (as previously mentioned in the QCM radiant heat test) leading to the dip in temperature at that point. We rectified the fault by tapping the base of the heater with a wrench. The wires reconnected and we pressed forward with the test.

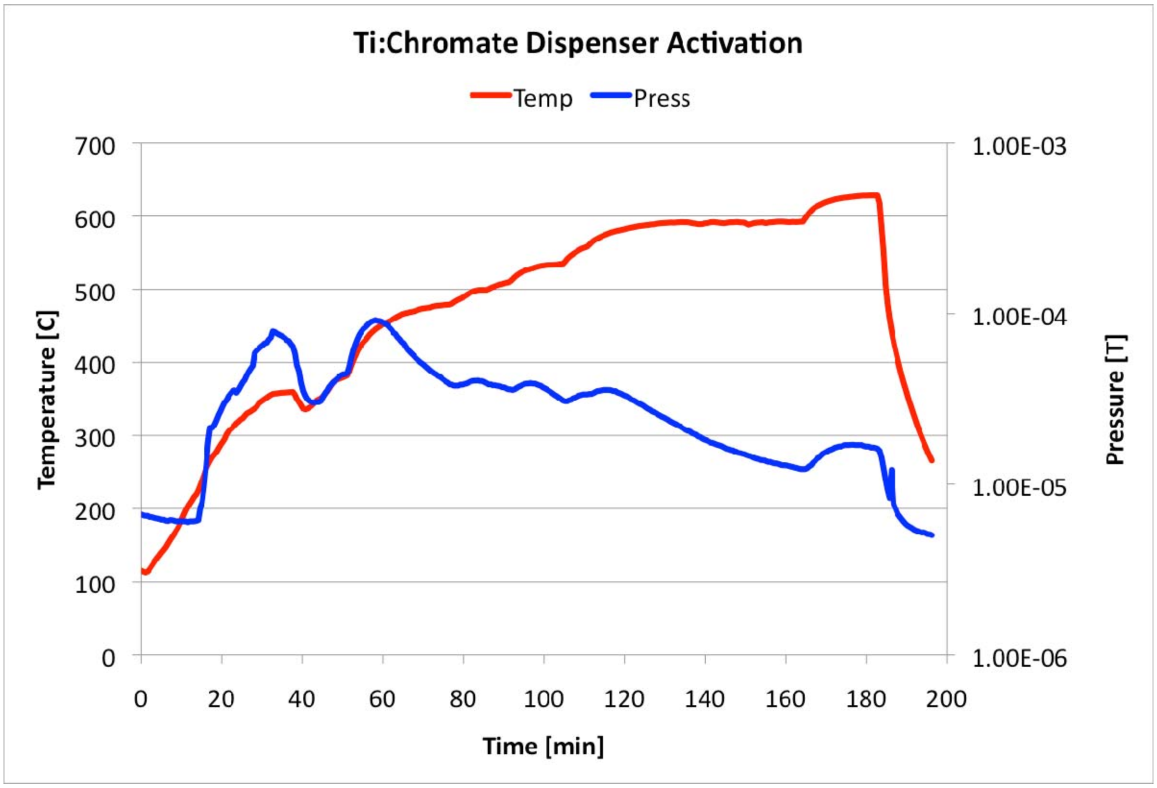

Figure 63. Pressure and temperature—Ti:Cs chromate dispenser activation

Once at 475°C, and noticing no deposition, we increased the temperature up to 595°C hoping to record some cesium deposition by this point. After 45 minutes of no recorded deposition we increased the temperature to 620°C for 15 minutes. After this, and not recording any cesium deposition, we ceased the test, presuming that we had a bad dispenser. Once the dispenser had been removed from the chamber, we realized that a simple measurement error had caused us to improperly position the QCM. The sensor had been occluded by the side-pipe for the entire test thus blocking the sensor from recording any potential deposition.

In the Alvatec cartridge tests, we used the gradual reduction in total vacuum pressure as an indication of cesium release via the getter process mentioned in Chapter V.E.3. In both those tests, the pressure went down at least one order of magnitude[3]; in

---

[3] Pressure dropped from 3 x $10^{-5} \rightarrow 3$ x 10^{-6} Torr during the 1st Alvatec cartridge activation. Pressure dropped from 2 x $10^{-5} \rightarrow 3$ x 10^{-7} Torr during the 2nd Alvatec cartridge activation.

this test, the pressure never decreased below the initial pressure as maintained by the turbopump. So, despite the lack of accurate QCM data or gettering indications, we conclude that no appreciable cesium was released into the vacuum.

Figure 64 shows the relative pressures of various gasses of interest during the test.

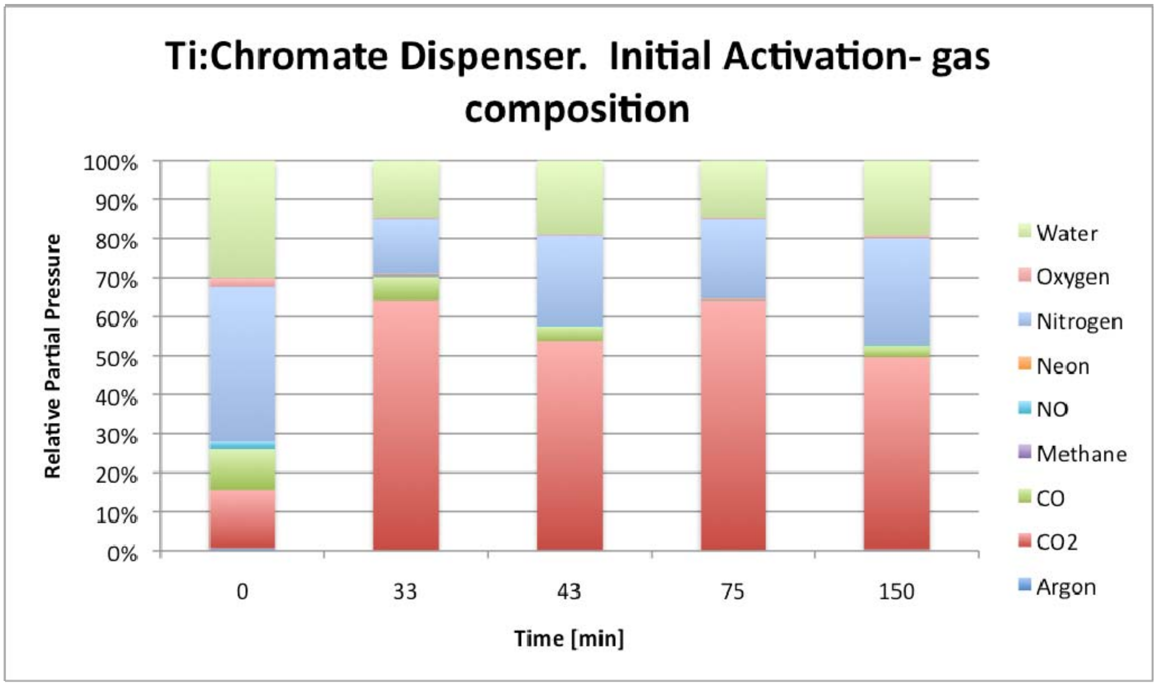

Figure 64. Partial pressures of various gases throughout Ti:Cs chromate test

The significant thing we see from this chart is the increase of CO2 after 30 minutes and 300°C, which is a normal outgassing constituent when dealing with heated objects in a vacuum [61]. What can we learn from the vacuum system data in this test? Unfortunately, not much. Perhaps the most important learning point is that mistakes can be made in even the simplest of experiments.

3. EDS Examination of Ti:Cs Chromate Dispenser Cathode

After finishing the activation cycle of the Ti:Cs Chromate dispenser, we removed the sample and subjected it to analysis using a Scanning Electron Microscope (SEM) with Energy Dispersive X-Ray Spectroscopy (EDS) capability. SEMs are microscopes that utilize the quantum nature of electrons to generate pictures at much higher resolutions than visible light can achieve. EDS is a spectroscopic technique whereby high-energy electrons are focused onto a sample causing collisions that excite atoms in the sample. Each element has a unique atomic structure and emits a specific X-ray signature when it decays from an excited state. These X-rays are collected and analyzed in order to identify the atomic composition of the sample.

EDS examination allowed us to determine if cesium did permeate to the dispenser surface, and to what extent this took place. Figure 65 is the first of a series of SEM images depicting this analysis of the Ti:Cs chromate dispenser.

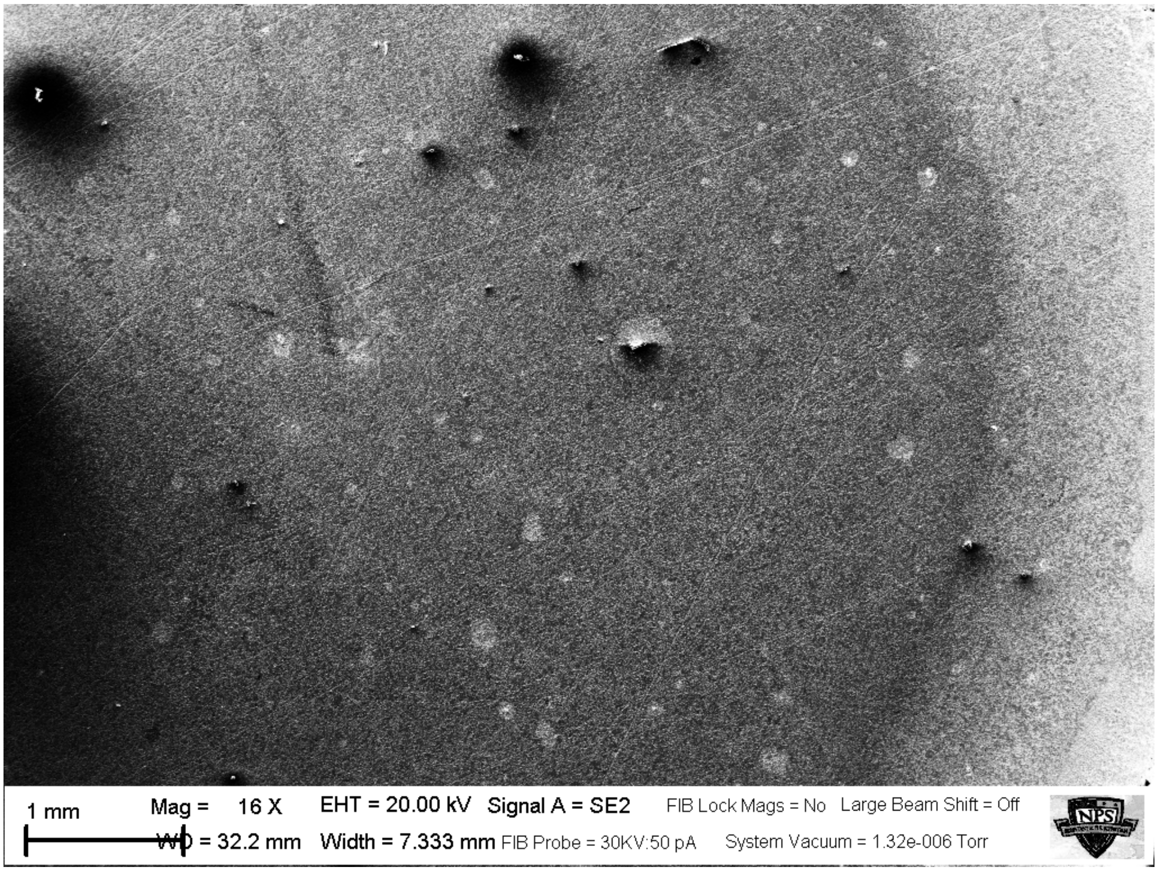

Figure 65. SEM wide field of view of dispenser surface

At this macro scale, we can see dark irregular bumps and small light-colored patches. The light arc at the far right is not cesium, but rather the sintered edge of the tungsten cap. Upon further examination, we came to recognize the dark spots represented various surface contaminants (such as dirt or pollen) while the light spots were cesium that had diffused through the tungsten cap. Further analysis will show that cesium was absolutely localized to these light spots. The dark area that comprises the majority of surface did not merely have a lower cesium concentration, but rather none at all.

The ideal level of surface diffusion for low work function cathodes is approximately 60% [20]. Figure 65 shows a much lower level of coverage than this, and as such, we can say that this cathode effectively failed to activate.

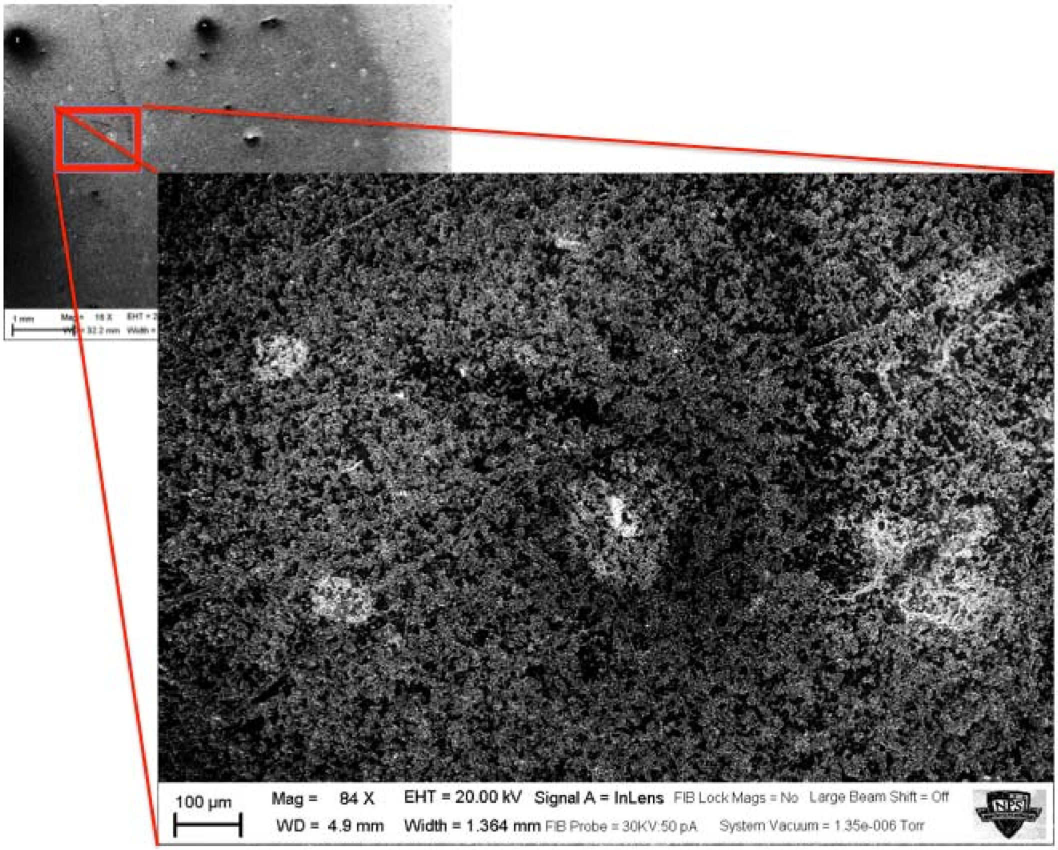

Figure 66. Zooming in on cesium spots

Figure 66 zooms in on a small area of Figure 65. Here, we see four or five light colored spots where cesium has migrated to the surface. At this point, we are also able to start making out the texture of the porous tungsten dispenser surface. The central-most cesium spot had what appeared to be an eruption of material from the surface. Figure 67 takes the image from Figure 66 and shows this ‘eruption’ in greater detail.

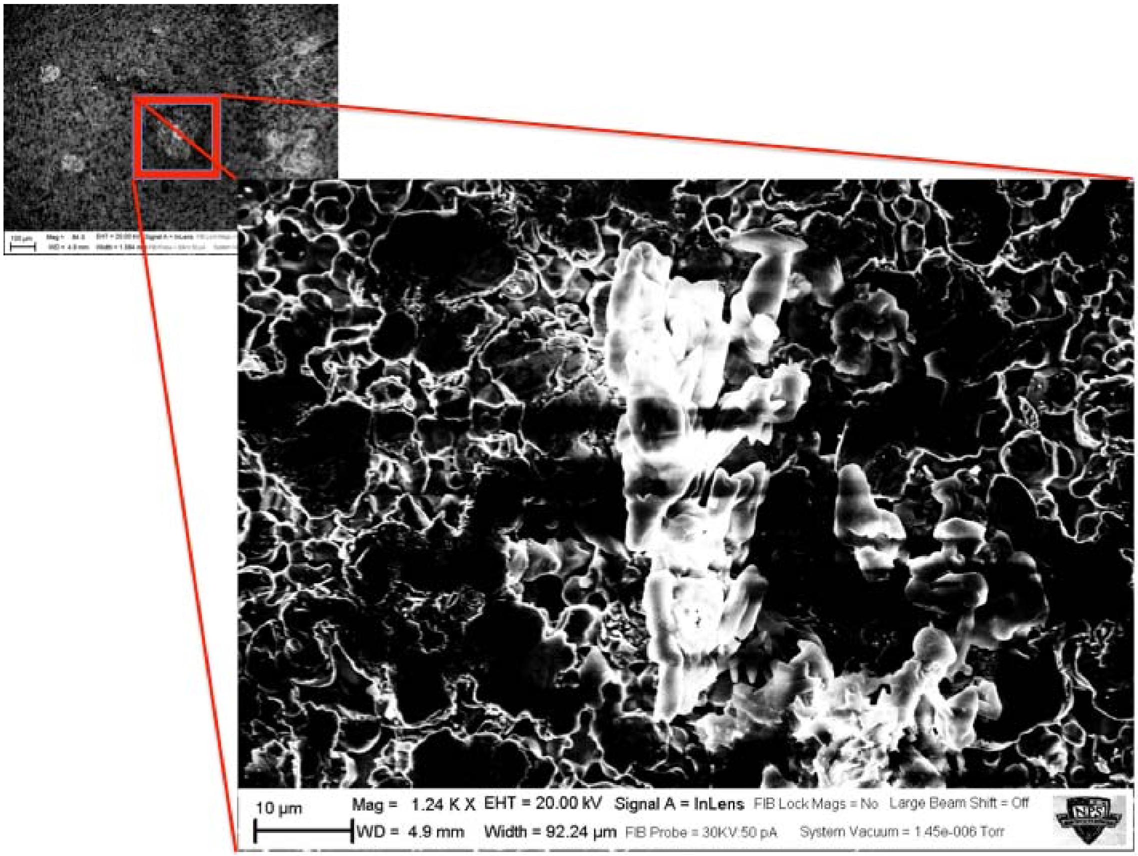

Figure 67. An apparent eruption of cesium from the dispenser surface

The brightest portion of this image is where the cesium appears to have come through to the surface. The intensity diminishes near the edges of the photo—corresponding to the outermost dimensions of the feature as seen in the image. The horizontal lines through the center of the image are artifacts produced by the image processing algorithm. We were unable to discern the height of the peak with the available equipment, but this is a matter of concern due to potential field emission and is being pursued by researchers at the University of Maryland [62].

Figure 68 shows the spectrographic analysis of the cesium spot shown in Figure 67. The spectrograph shows us the spot is mainly composed of cesium oxide, which would have been elemental cesium prior to atmospheric exposure. The three peaks to the right of the main Cs peak are additional structure of the Cs signature. We also notice faint peaks of aluminum (deposited in the vacuum system during PVD testing) and iron (possibly from the steel dispenser casing).

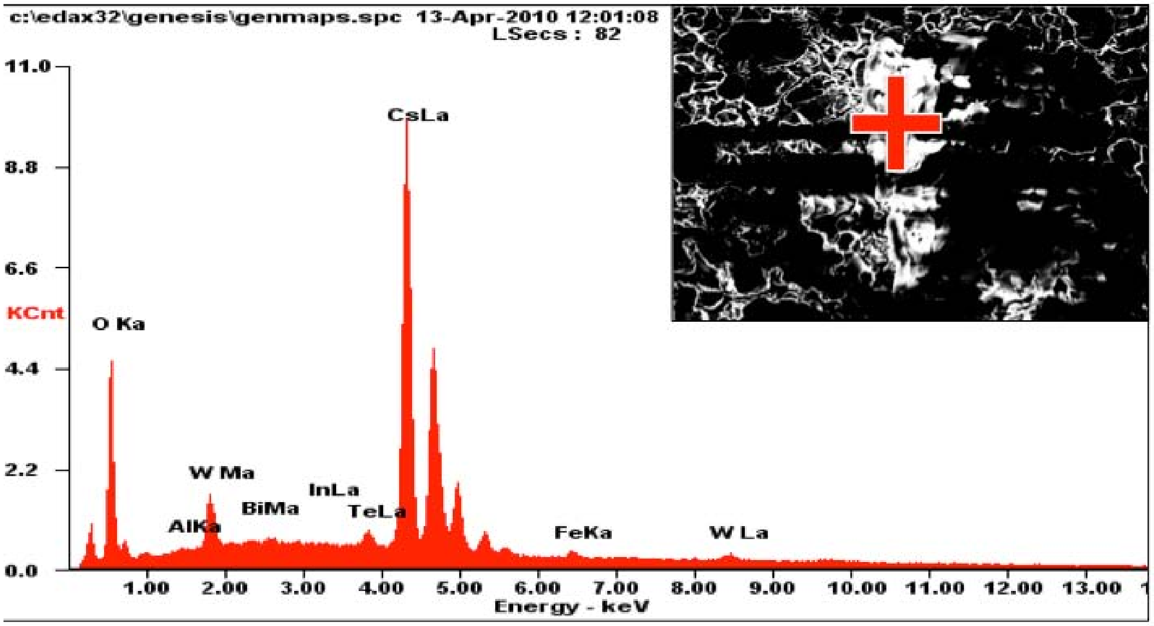

Figure 68. EDS examination of eruption location

A final note on interpretation—the two-letter abbreviations (La, Ka, and Ma) following the elemental abbreviations identify which electron excitation of that element is responsible for the signal.

Figure 69 presents a spectrographic analysis of the uncesiated tungsten surface. While this spectrographic composition is limited to the small area underneath the cross, it represents the analysis of a major portion of the uncesiated tungsten surface.

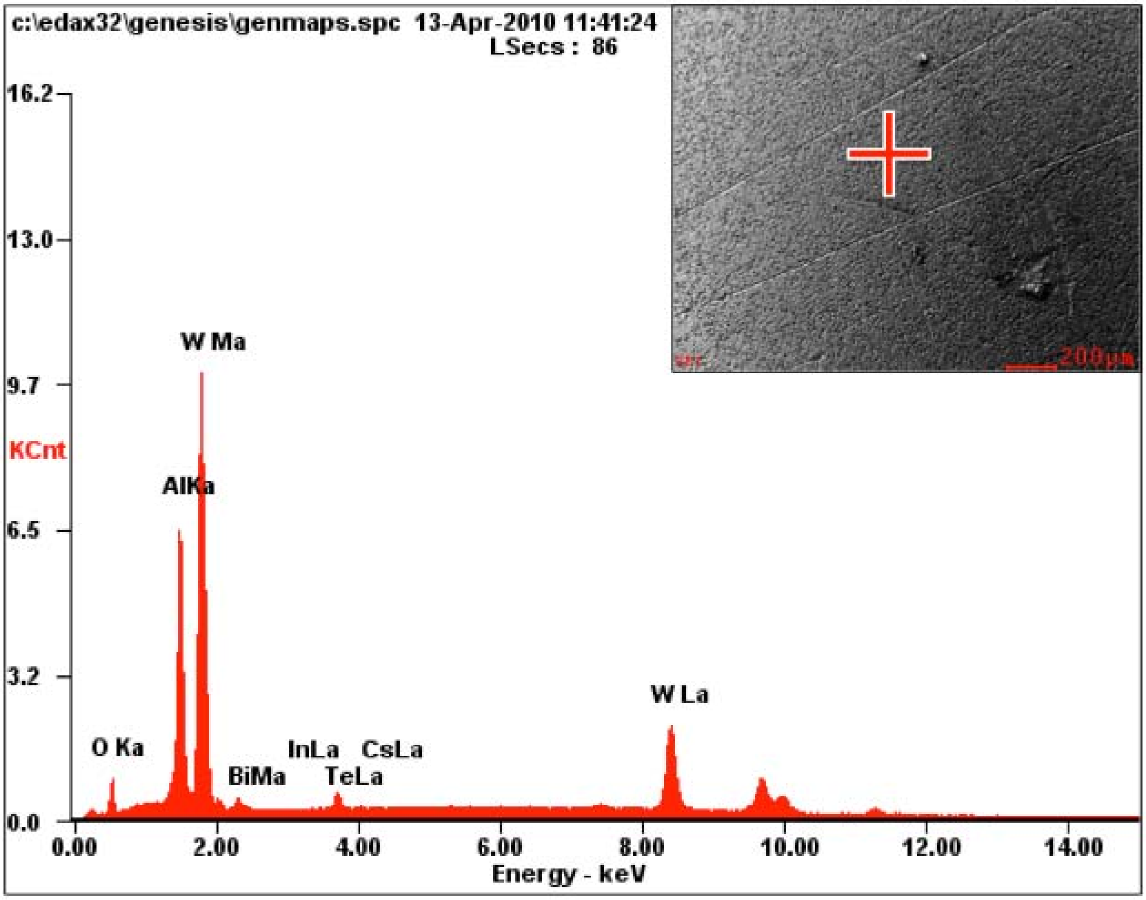

Figure 69. EDS examination of uncesiated dispenser surface

After tungsten, the second strongest signature comes from aluminum. Further testing must be done to determine the origin of the aluminum. One likely source is residual contamination from the aforementioned aluminum PVD test, but that cannot be stated with absolute confidence. Another possible source would be the aluminum foil we used in the lab to cover vacuum components, such as the dispenser and heater, prior to installation.

4. Conclusions from Ti:Cs Chromate Dispenser Test

a. Even simple experiments can easily go wrong by minor inattention to detail.

b. The test stand should be reconfigured to allow for visual verification of QCM placement. Figure 70 details the changes made in the test stand. All other experimental components retained their respective positions as seen in Figure 62, but have been removed for the sake of visual clarity.

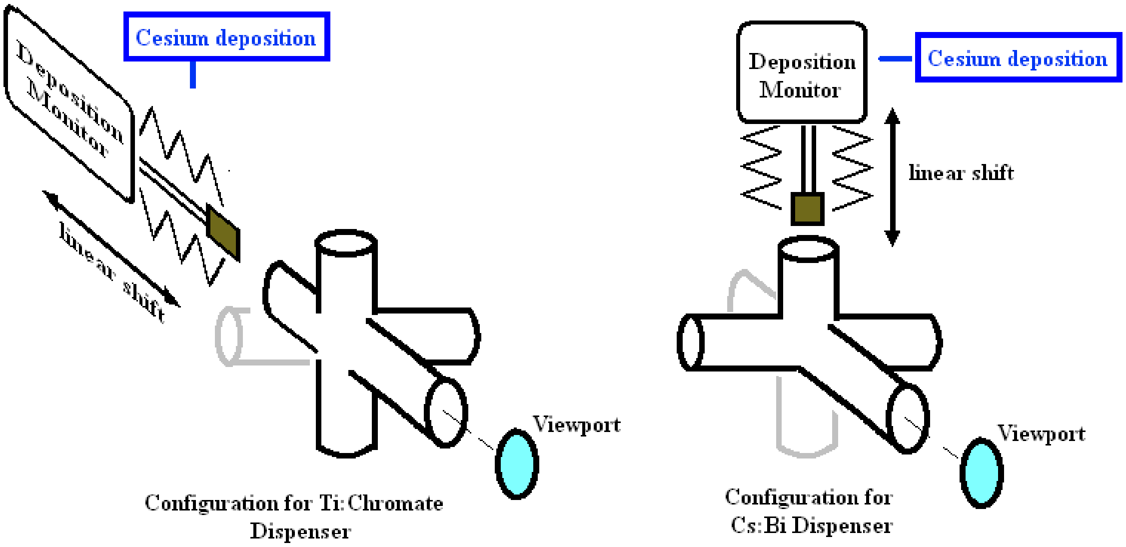

Figure 70. Test stand configuration change after Ti:Cs Chromate test

The viewport is only shown to indicate its position in relation to the other instruments—not to indicate that it was directly bolted to the 6-way cross depicted. With this new configuration, we had a side-view of the QCM in order to visually confirm the proper positioning of the QCM rather than having a view that provided us with no tangible information.

c. EDS examination of the Ti:Cs Chromate dispenser showed evidence of incomplete activation. Additionally, the examination suggests cesium evolved vertically from the surface. This will require further examination to determine its overall effect on photocathode performance.

I. CS:BI DISPENSER PHOTOCATHODE CESIUM EVAPORATION TEST

1. Activation of Cs:Bi Dispenser

The second dispenser photocathode we tested contained an Alvatec cesium source. Without deposition data from the Ti:Cs Chromate dispenser, this was our last chance to properly gather the cesium evaporation data we needed to characterize this style of dispenser cathode.

Figure 71 shows the temperature and pressure history of the test. The system was actively turbopumped during this test as we anticipated a large argon release when the Alvatec cartridge’s indium seal melted. The initial 50 minutes of test record the effects of a gentle bakeout (<100°C) of the heater assembly prior to the actual start of the test. The three pressure spikes seen during this time were caused by unanticipated releases of argon gas. We were not expecting these argon releases, and had not looked for, or observed them, during the previous tests with just the Alvatec cartridges.

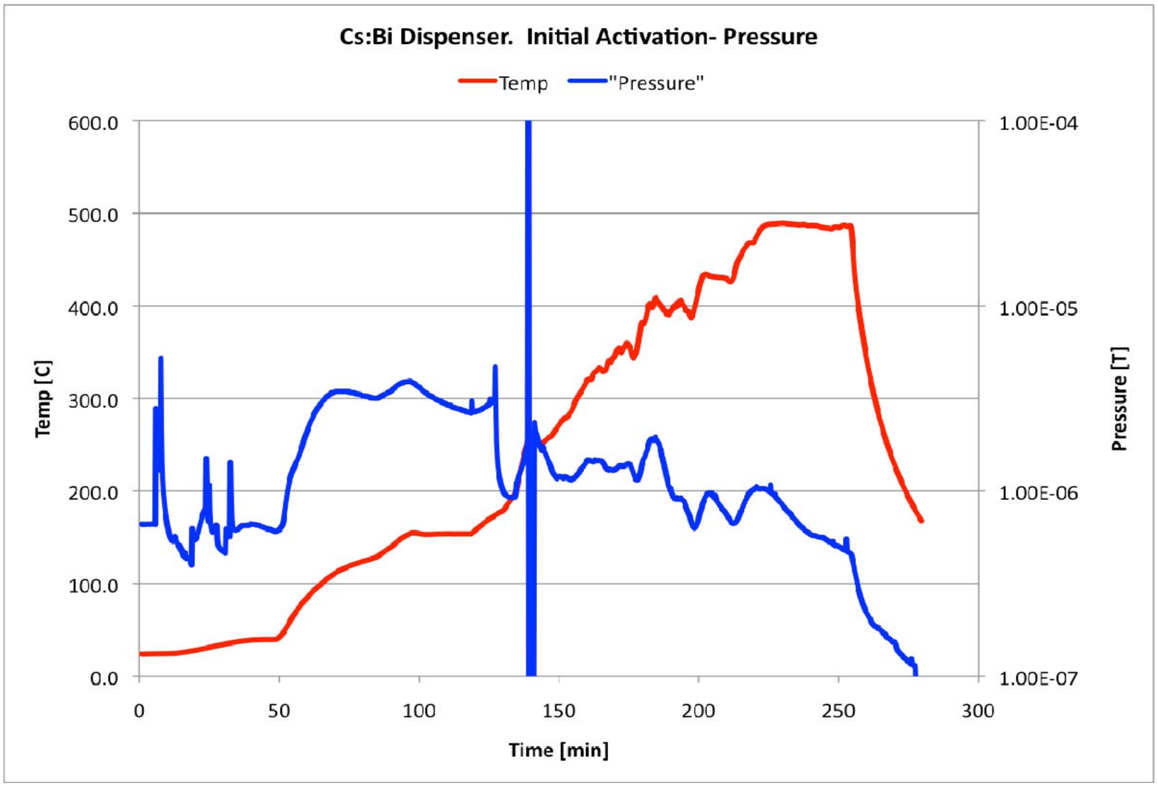

Figure 71. Cs:Bi dispenser pressure and temperature during initial activation

The actual test started at 50 minutes where we see a gentle ramp up to 150°C. With no argon release evident, we steadily increased the heat up to 490°C. At 250°C the argon spiked, indicating the melting of the indium seal. While this is almost 100°C hotter than the temperatures of argon release seen in the Alvatec experiments, it is readily understandable. In the Alvatec tests, the cartridges were firmly clamped to the heater face, which ensured good thermal transfer between the heater and cartridge. In the dispenser cathode test, the cartridge was free to roll around inside the dispenser and would have very poor thermal contact with the dispenser walls. Additionally, the dispenser bottom and sides are made of stainless steel—a poor thermal conductor. A differential of order 100°C is not surprising given these conditions.

We anticipated water outgassing as we started to heat the cartridge, and Figure 72 demonstrates this to be the case. In this graph, we see the partial pressures of various gasses compared against each other during the course of the experiment.

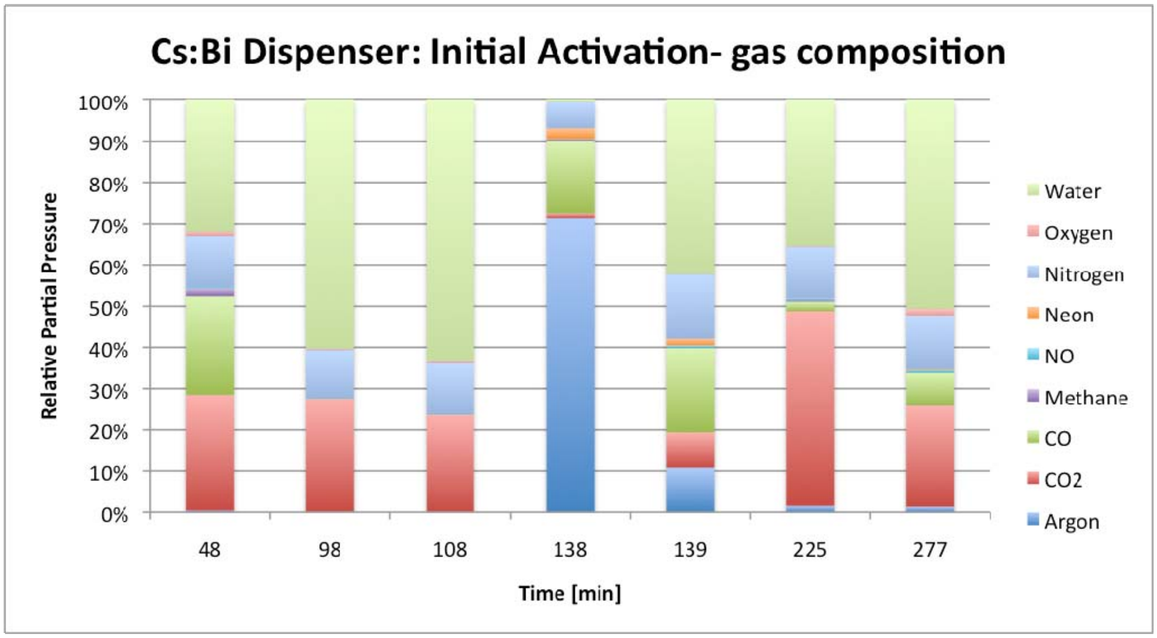

Figure 72. Relative gas composition of the vacuum during initial activation

As a reminder, we mentioned in the Eimac RGA analysis that the percentages shown reflect the ratio of each gas versus the other selected gasses. The percentage partial pressures are not scaled against the total vacuum pressure, which would necessarily consist of other gasses as well.

Going on, we see a successful indium melt (i.e., cartridge activation) at 140 minutes, as indicated by the argon pressure spike seen in Figures 71 and 72. Unlike the Alvatec experiments, the pressure does not start to immediately decrease after the argon spike. The pressure fluctuates up and down for an hour, after which there is a noticeable and gradual decrease in total pressure. This pressure drop roughly coincides with the first signal of significant deposition as recorded by the QCM in Figure 73. Up to this point in time, the thickness had slowly crept up to 10Å, and subsequently dropped to 8Å. We do not know the reason for the initial rise in thickness.

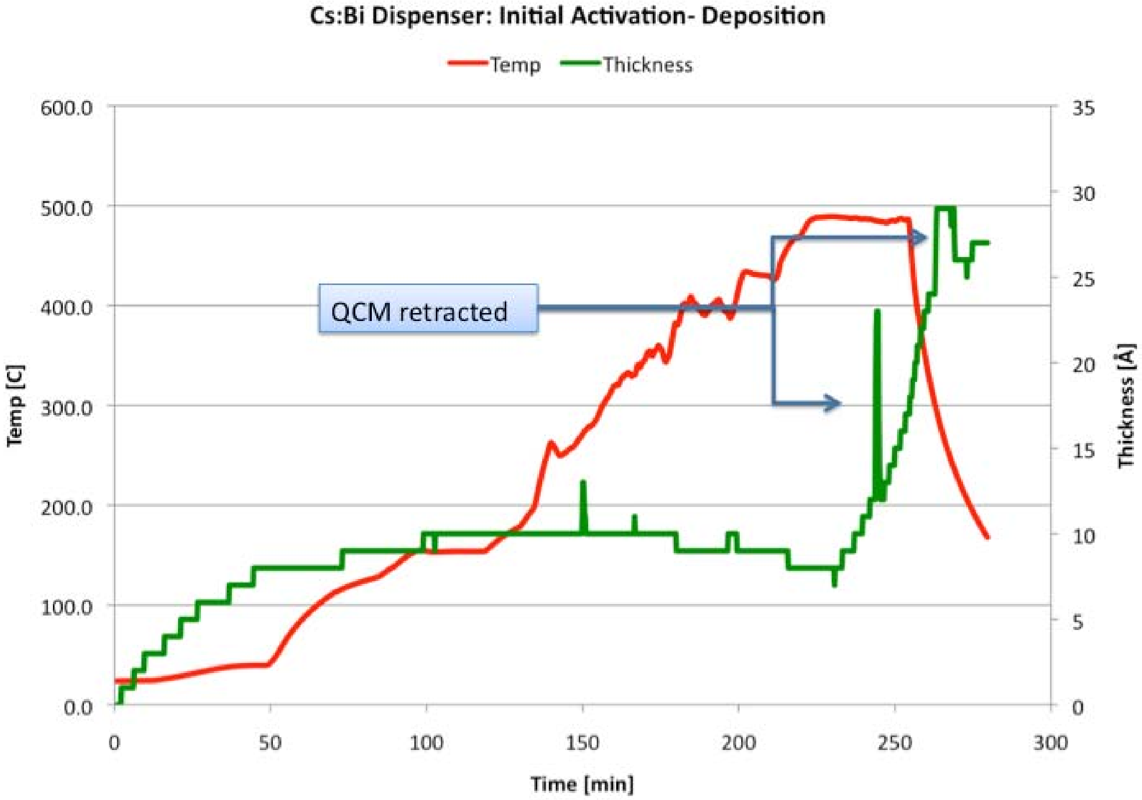

Figure 73. QCM data during initial activation of Cs:Bi dispenser

The subsequent drop back to 8Å is likely due to radiant heating. Regardless, we started recording significant deposition at 235 minutes and a temperature of 410°C. We maintained this temperature until 257 (a duration of 22 min) during which the QCM thickness rose from 8Å to 16Å. Since the diameter of cesium atoms is 5Å, this level of deposition corresponds roughly to 2 monolayers of cesium.

At 250 minutes, we retracted the QCM in order to determine if the RGA would detect Cs^{+2}. It was not able to do so, but nonetheless this caused the first spike as indicated on the plot. Going on, the apparent increase in deposition rate after 257 minutes (corresponding to 16Å) cannot be interpreted as accurate data. This rate increase coincides with the securing of heater power, and is in some part due to crystal cooling rather than actual deposition.

Having reached both our experimental goal as well as the end of the day, we retracted the QCM for five minutes and turned off the heater power. This retraction is indicated on the figure at 257 minutes. After reinserting the QCM, we still noticed deposition, up to a final value of 27Å at which point we ceased data collection.

2. Cs:Bi Dispenser Test Runs 2 and 3

The next day we took the dispenser through a series of temperature steps in order to see how cesium evaporation would change with temperature. During this test run, as well as following test, we disconnected the turbopump and maintained the system vacuum solely via the ion pump. We chose to do this because the risk of exposing the ion pump to argon had passed and the ion pump would allow us to achieve lower pressures than the turbopump.

Figure 74 shows the pressure and temperature history of this test. The pressure started in the mid 10^{-8} Torr but then increased to almost 10^{-6} Torr at 55 minutes—corresponding to the highest temperatures we subjected the dispenser to during the test. After that spike, the pressure gradually decreased to levels observed at the beginning of the test.

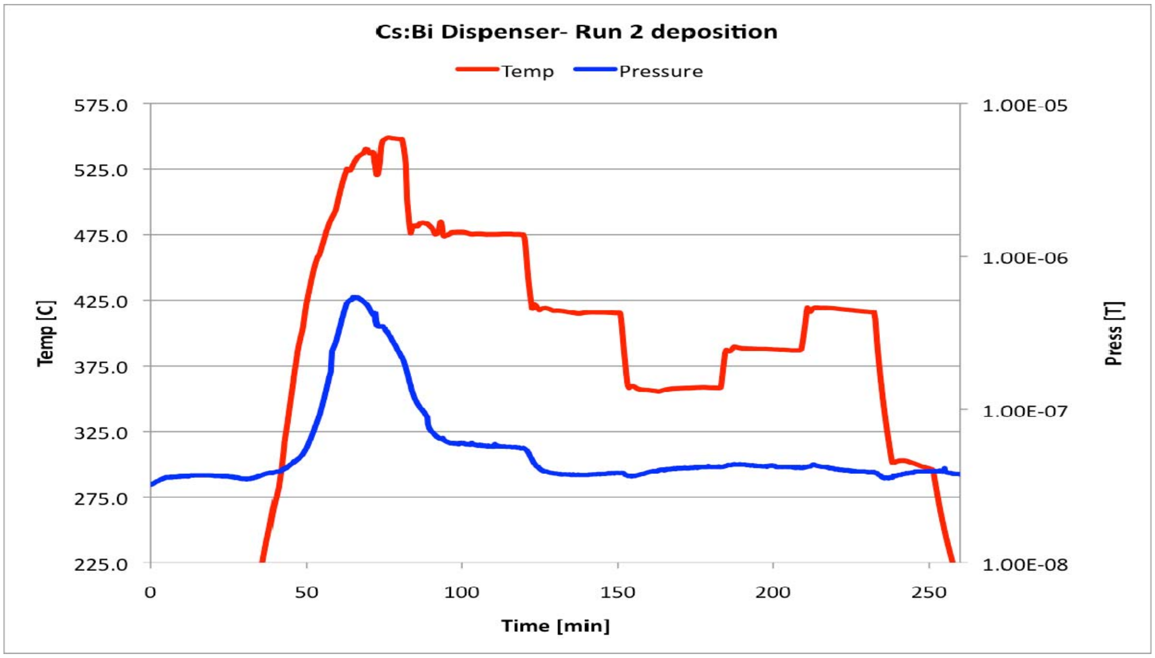

Figure 74. Run #2—temperature and pressure

Figure 75 shows the deposition history during Run 2. From a cold start, we increased the temperature until we saw a definite signal of deposition. This occurred at approximately 525°C.

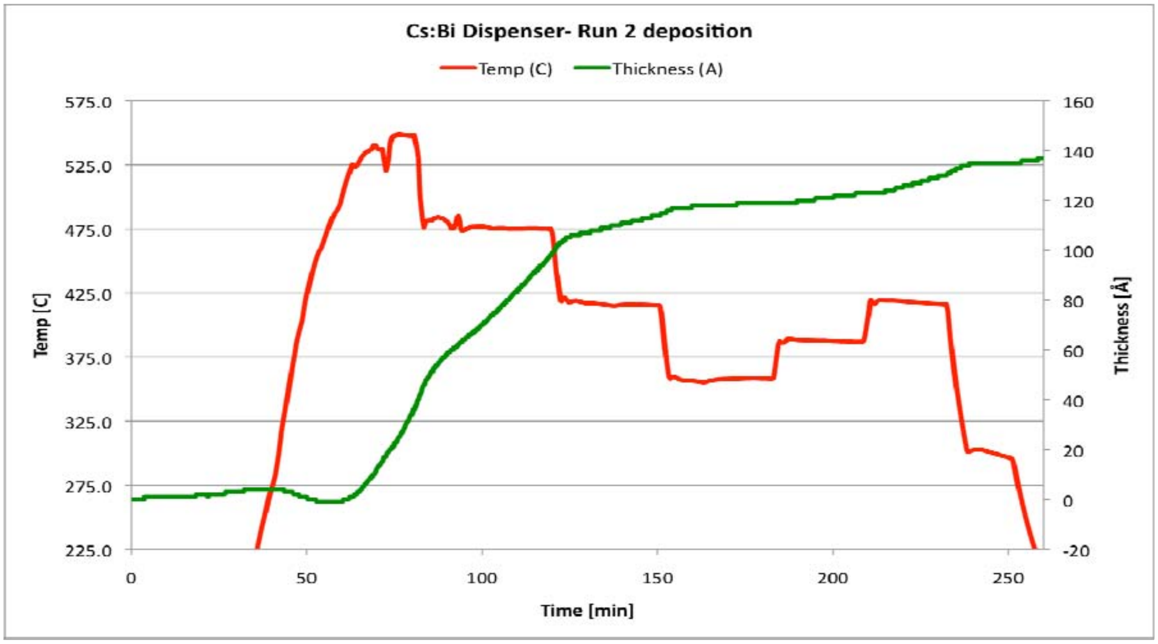

Figure 75. Run #2—deposition history

After holding 550°C for approximately ten minutes, we reduced the temperature in a step-wise fashion until the QCM recorded nearly negligible deposition at 360°C. We increased the temperature to 385°C and then to 420°C, holding steady for at least 15 minutes at each temperature level.

Figure 76 shows the relative gas composition for the gasses listed on the right. The most significant deviation from the norm during the course of the experiment occurred between 60 and 70 minutes, nearly corresponding to the maximum temperature the dispenser was subject to.

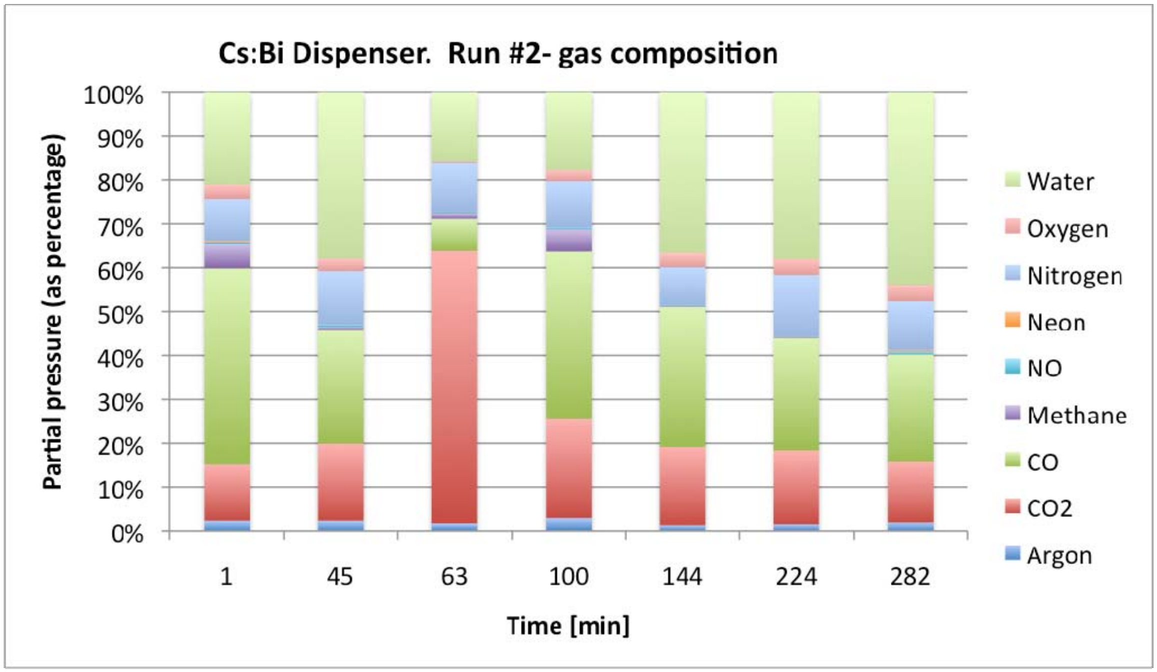

Figure 76. Relative pressures of various gases during Run #2

This spike in carbon dioxide may be attributable to outgassing from the heater and dispenser assembly since we had only taken it up to 490°C during the Activation Run. As the pressure subsided from this maximum, the partial pressure of carbon dioxide also decreased to near its initial level at the beginning of the test, indicating that the source of CO_2 had been exhausted.

The results from Run 2 were very interesting, but were they repeatable? We repeated the test with the same temperature profile, but held the dispenser at each temperature step for a longer period of time (at least 20 minutes). Figure 77 depicts the temperature and pressure history during Run 3. The pressure initially rises from the mid 10^{-8} Torr to above 10^{-7} Torr, but then decreases to low 10^{-8} Torr by the end of the test.

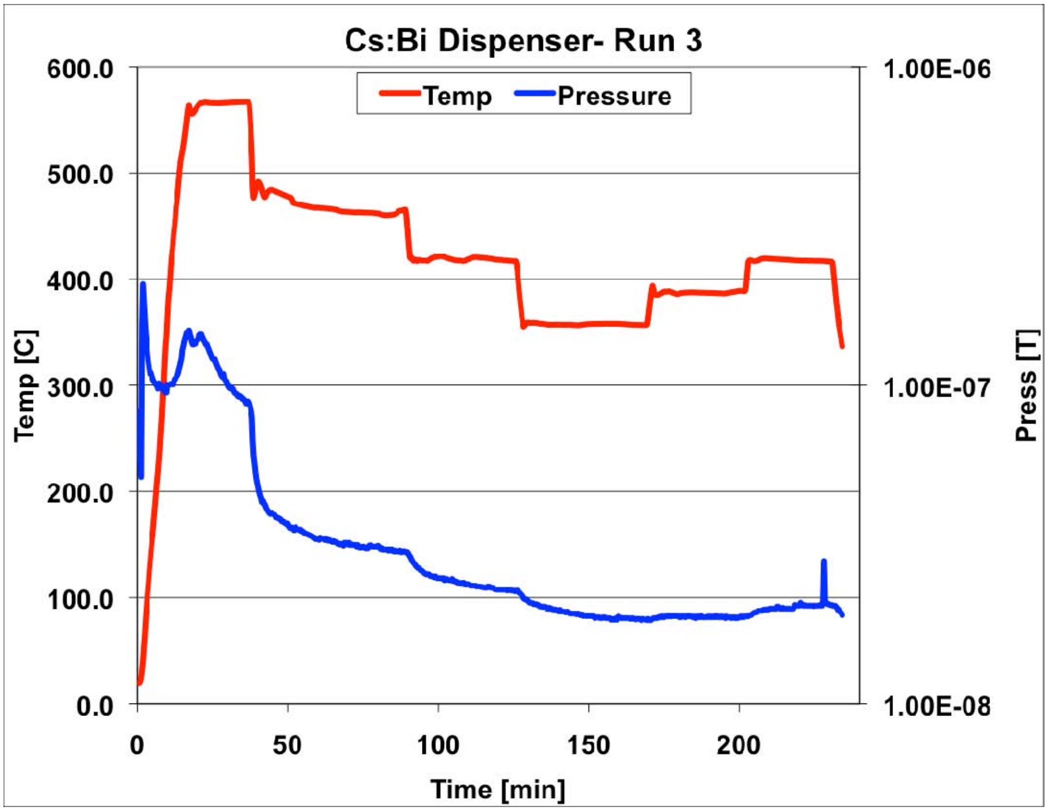

Figure 77. Cs:Bi Dispenser Run 3 Temperature and Pressure Profile

As in Run 2, we chose to use only the ion pump since running the turbopump did not improve the vacuum at these pressures. The decrease in vacuum pressure over the course of the test is attributable to getter pumping via cesium release, and strongly suggests that cesium was evolving from the dispenser face [56]. The QCM data bears this out, as seen in Figure 78. This profile looks very similar to the deposition profile in Run 2—initial deposition starts after the temperature increases above 400°C, and fluctuates according to temperature.

Figure 78. Run #3—deposition data

Though Runs 2 and 3 have similar patterns of deposition, the rate of deposition increased from the second to third run. Figure 79 shows deposition rates at various temperatures for all three runs—Activation, Run 2, and Run 3. For each run, we selected time intervals of relative thermal stability in order to remove errors associated with thermal transients associated with the QCM.

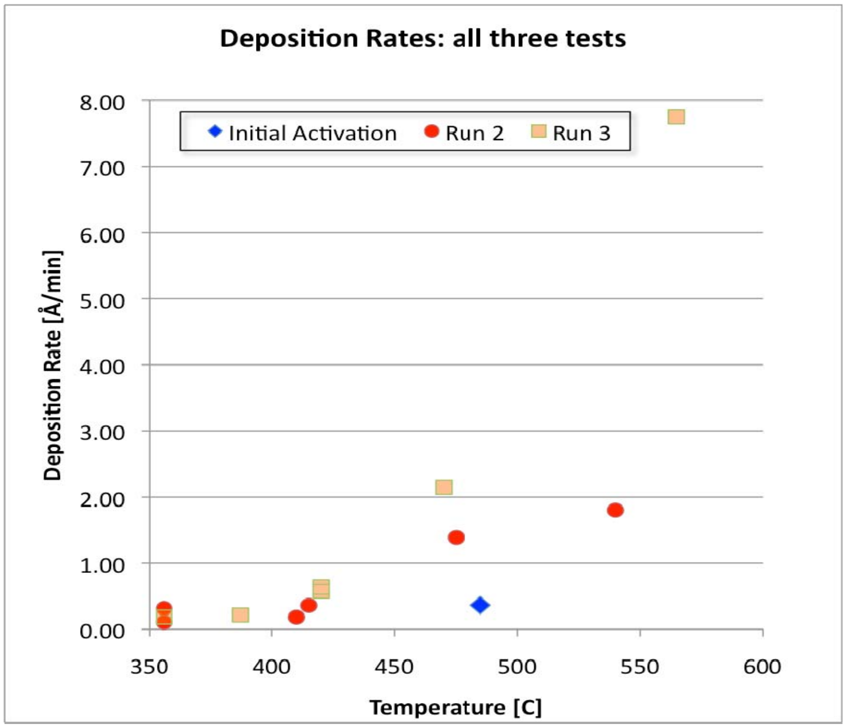

Figure 79. Deposition rates at different temperatures for Activation, Run 2, and Run 3

Along the horizontal axis, we see heater temperature, and the vertical axis shows the corresponding deposition rate on the QCM for that respective run and temperature. This data illustrates several important details, which we discuss individually.

The first notable observation we see from the figure is that the cesium evaporation rate for a given temperature seems to increase with each subsequent run. This is due to an increase in the concentration gradient between the back and the front of the sintered tungsten surface. A higher concentration of cesium inside the dispenser corresponds to a higher evaporation rate off the tungsten face [17]. This internal concentration, in turn, is dictated by the quantity of cesium released from the cesium:bismuth compound in the Alvatec cartridge. The reaction that frees cesium from the bismuth is a sublimation process—it does not happen instantaneously. We conclude that the initial activation may only have released a fraction of the total cesium from the cartridge. Subsequent heating profiles would successively release more cesium, thus increasing the concentration gradient and promoting increased evaporation.

J. HIGH-TEMP SOAK OF CS:BI DISPENSER

Suspecting that the Alvatec source inside the dispenser had not fully released its full supply of cesium during the brief periods at high temperatures, we decided to perform a high constant-temperature soak. Doing so would liberate as much cesium as possible and hopefully lead to a steady cesium concentration within the dispenser and thus a repeatable evaporation profile for given temperatures. If it so happened that we released more cesium during the soak we would expect to see a deposition rate that initially increased before settling down to a constant rate that was greater than what it was at the beginning of the soak. Figure 80 shows the temperature and thickness data for this high temperature soak.

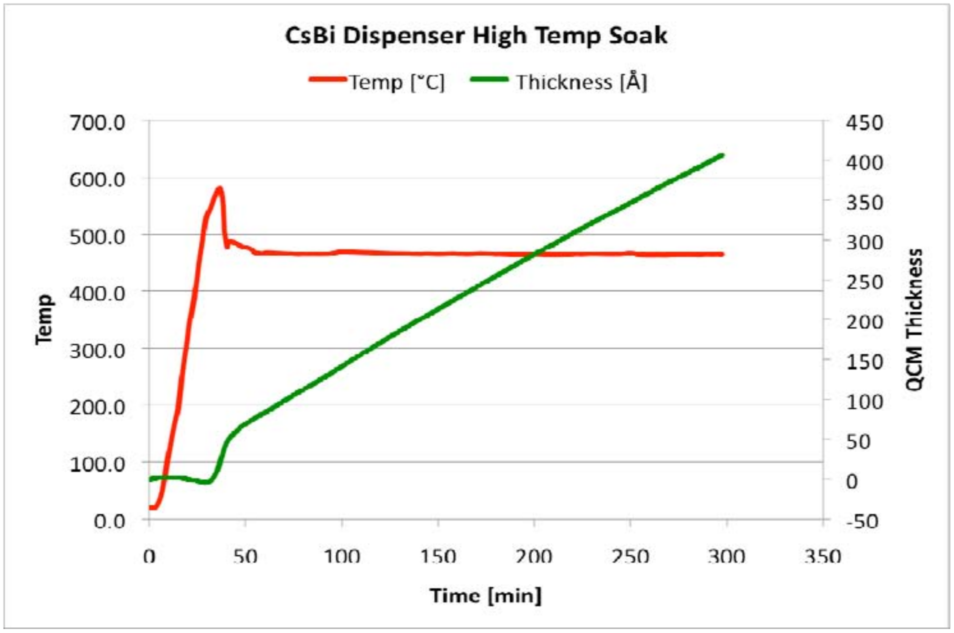

Figure 80. Results from high temperature soak of Cs:Bi dispenser

Ignoring the thermal transients through the first 50 minutes of operation, the dispenser spent four hours at 460°C. The data shows a nearly constant deposition rate of 1.36 Å/min with only a slight decrease in the last half of the test. The deposition rate at 460°C roughly correlates to the rates seen for Runs 2 and 3 (Figure 79). Though unable to verify that the cesium had fully sublimated from the bismuth structure, the constant deposition rate from the data suggests as much.

VI. SUMMARY OF RESULTS FROM TESTING OF CS:BI DISPENSER PHOTOCATHODE

A. INCREASING DEPOSITION RATES ON SUCCESSIVE RUNS

We suspect the deposition rate increased during each successive test due to a failure to liberate all the cesium in the initial activation, and then second run. As we took the dispenser to, and past, 500°C we possibly liberated successively greater quantities of cesium, thereby increasing the concentration gradient, and resultantly the evaporation rate.

The high-temperature soak (Chap. VI.J) demonstrates that, if this were the case for the first three runs, the effect has since been overcome. Of course, in order to verify the full release of cesium we must run another temperature profile. In the future, activation profiles would likely call for subjecting the dispenser to a high temperature soak in the order of hours to ensure the full liberation of cesium from the cartridge contained therein [61]. Another option for improving repeatability of cesium evaporation would be to switch to a mechanism of release that is more absolute than sublimation (pure cesium cartridge or glass capsule).

B. ESTIMATING SYSTEM CONTAMINATION FROM EVAPORATED MATERIAL

The data collected from the Cs:Bi dispenser has an end beyond itself. The reason we plunged down this experimental path was to determine the level of cesium contamination from the cathode.

In order to estimate the rate of cesium contamination from the dispenser, we must estimate the quantity of cesium captured by the QCM. It so happens that material does not evaporate at an equal rate in all directions—experiments have shown that the evaporation rate for small resistance-heated samples is highest normal to the face, and falls off with a cosine dependence as seen in Figure 81 [63].

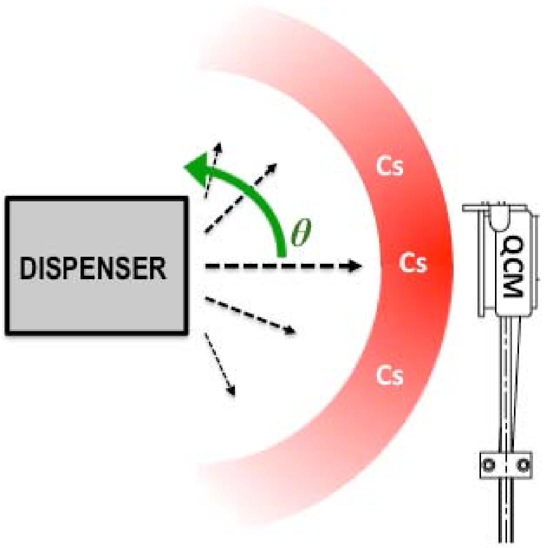

$$\boxed{i(\theta)\, d\omega = cos(\theta)\, d\omega}$$

$i(\theta)$ = evaporated quantity or flux

$d\omega$ = solid angle intercepted

Figure 81. Deposition rate falls off at shallower angles of incidence

The boxed equation and following terms in Figure 81 describes this angular evaporation characteristic. Based upon the geometry of our test stand, we estimated that our QCM was intercepting approximately 4.1% of all cesium evaporating off the cathode surface. In order to determine the total mass rate of cesium evaporating off the cathode we assumed that the deposition rate was effectively constant over the entire surface of the QCM (reasonable given the QCM's position normal to the dispenser face as well as its small solid-angle intercept area at 12 cm). Additionally, we assumed that all cesium, once deposited on the surface of the QCM, remained there. This assumption is not perfect, but it makes the problem tractable. If some cesium desorbed from the QCM then the measured rates are lower bound. The quantity of cesium deposited over a minute on the QCM face is calculated with *D* = QCM diameter, and *h* = Å accrued in 1 minute:

$$\text{Qty deposited Cs} = \left(\pi \frac{D^2}{4}\right) \rho_{Cs} \left(\left[\frac{\text{A}}{\text{min}} \right], h \right). \qquad [5]$$

Figure 82 schematically depicts this calculation as described.

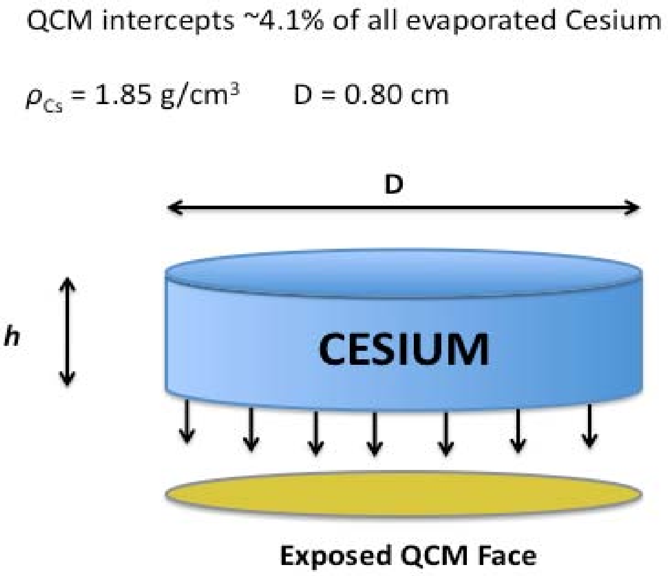

Figure 82. Estimated cesium deposition profile on QCM

Evaporative figures are best calculated in terms of evaporation per unit area. As such, we needed to estimate the effective surface area of the dispenser across which cesium evaporation took place. Without having the assistance of a measurement tool to gauge the evenness of cesium across the cathode face (such as EDS), we chose to model the evaporative flux off the dispenser as a top-hat profile (Figure 83) with a 1.09 cm (0.43 in) diameter.

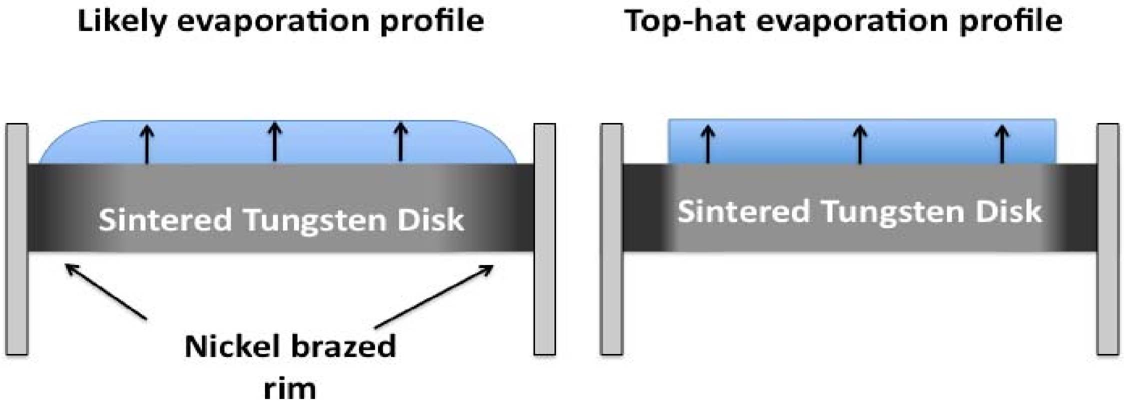

Figure 83. Cesium evaporative profile—realistic versus estimated

This effective diameter is a guess based only upon a visual examination of the EDS data from the Ti:Cs chromate dispenser cathode test. This number is also conservative (small), and should yield a higher flux-per-area than was actually the case. With the QCM intercepting 4.1% of all evaporated cesium, the total evaporation rate has been plotted in Figure 84. The deposition rate (horizontal axis) goes from 0–10 Å/min, and the vertical axis is in units of micrograms/square-centimeter/minute.

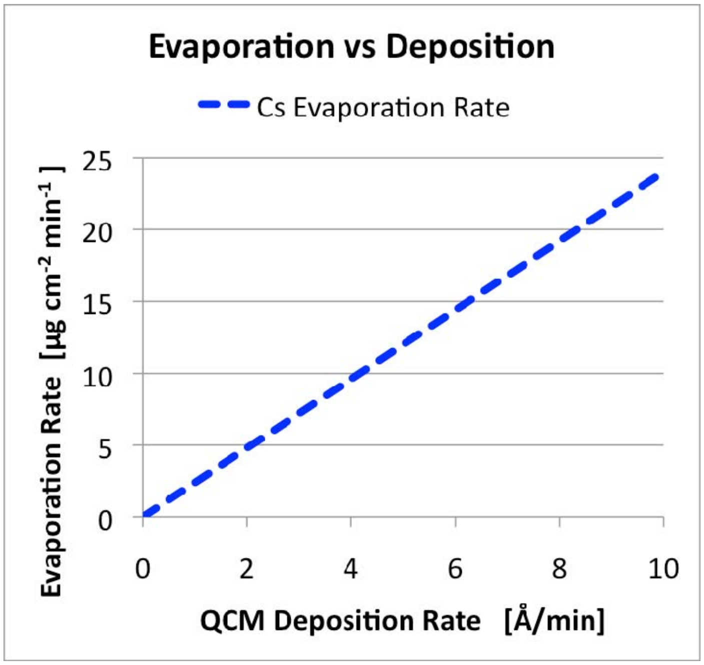

Figure 84. Correlation between QCM deposition and Cs evaporation

For comparison's sake, J. L. Cronin measured the evaporation rate of barium from various thermionic dispenser cathodes and recorded rates of 1-20 μg cm^{-2} hour^{-1} over the range of operational temperatures [16]. Of course, a thermionic cathode will constantly emit low-ϕ material over the entire duration of use whereas it is not the intent to operate the UM dispenser at these temperatures for lengthy periods of time. Rather, the UM dispenser photocathode has several envisioned operational regimes:

1. Photoemission without constant rejuvenation—having once cesiated the surface of the cathode, it could be brought to low/cryogenic temperatures where the evaporation rate of cesium would be effectively zero.
2. Photoemission with constant rejuvenation—gentle levels of heat (as yet undetermined) would be applied to constantly resupply the front face with cesium. Expected evaporation rates would be much lower than those seen in this data.
3. Activation/Rejuvenation—when activating or quickly rejuvenating a cathode it would be subject to high temperature processing in order to quickly recesiate the surface. This might be done in-situ, or in a dedicated chamber.

The data presented in this work most applies to this third operational regime. Further testing must take place in order to determine evaporation rates in the other two operating regimes. Ultimately, a synthesis of data from all regimes is necessary in order to ascertain the viability of this style dispenser photocathode in future systems.

THIS PAGE INTENTIONALLY LEFT BLANK

VII. CONCLUSIONS AND CLOSING REMARKS

The entirety of this work has focused on measuring the performance of two different cathodes with two different fates. The following provides a quick overview of the paths travels and discoveries made.

A. EIMAC Y-845 THERMIONIC CATHODE

The primary motivation for activating the Eimac cathode was twofold. First, we wanted to find out how easy or difficult it would be to activate a cathode in preparation for future experiments. It so happens that the activation of a new cathode was remarkably easy given a properly configured vacuum system. Second, we wanted to determine the thermal performance in preparation for future tests with electron sources. As the cathode contains no integral sensor that provides this information, we now have the necessary data for determining the cathode's operating temperature and subsequent performance. Both bodies of knowledge will assist in future cathode research that takes place at the Naval Postgraduate School.

B. UM DISPENSER PHOTOCATHODE

The joining together of cutting-edge technologies always has its attendant challenges. Fusing the elements of superconducting RF injector cavities with high performance dispenser photocathodes is a subject sitting at the edge of accelerator physicists' current knowledge and experience. The data presented in this body of research must be carried to the next level with theoretical and experimental inquiries as to the effects of monolayer cesium contamination on SRF modules. Gaining an understanding of the ramifications of such contamination will help guide future development efforts in the search for high efficiency-long lifetime photocathodes for research facilities and the Navy FEL program.

C. NEXT STEPS

This marks the end of our formal exploration of the University of Maryland’s dispenser photocathode. In discussions with our collaborators, we have created an outline of future tests to be conducted on the current dispenser cathode before removing it from the vacuum chamber for SEM-EDS analysis. This outline is as follows:

1. Further heating profiles will determine the effectiveness of the high temperature soak by comparing evaporation rates at various temperatures between 350°C and 550°C to the rates observed in Runs 2 and 3.
2. A minimum 24-hour low temperature (~200°C) soak will be executed prior to dispenser removal for SEM-EDS examination. The low temperature soak may reduce the presence of cesium peaks as noticed in the EDS examination of the Ti:Cs chromate dispenser.
3. Given the proven evaporation of cesium from this dispenser, the option should be exercised to create an EDS map of cesium across the dispenser surface. The Ti:Cs chromate examination only focused on distinct points because of the extremely localization of cesium. An EDS map, while more time consuming, will give an accurate 2-D presentation of cesium across a large area of cathode surface.
4. At present, we have no sure means of determining the temperature of the dispenser’s sintered tungsten face. A temperature correlation test should be run, similar to the heater calibration test, where a thermocouple is attached to the front face of the dispenser. This information will allow us to better understand and model cesium diffusion and evaporation according to well tested thermal models of these processes [29], [64].
5. Inquiries should be made with the Technical University of Dresden, in Germany, as they are the first to successfully operate a superconducting RF injector using a cesium telluride photocathode. They, of any group, would have first-hand experience dealing with the critical issues of cathode contamination and its effects on SRF injector performance [52].

LIST OF REFERENCES

[1] J. C. Maxwell, *A Treatise on Electricity and Magnetism*, 3rd ed., Dover Publications, 1954.

[2] F. R. Elder, A. M. Gurewitsch, R. V. Langmuir, and H. C. Pollock, “Radiation from Electrons in a Synchrotron”, Physical Review, Vol. 71, issue 71, pp. 829–830, June 1947.

[3] D. A. G. Deacon, L. R. Elias, J. M. J. Madey, G. J. Ramian, H. A. Schwettman, and T.I. Smith, “First Operation of a Free-Electron Laser,” Physical Review Letters, vol. 38, no. 16, pp. 982–894, April 1977.

[4] W. B. Colson, J. Blau, K. Cohn, J. Jimenez, and R. Pifer, “Free Electron Lasers in 2009,” Naval Postgraduate School. Monterey, CA. 2009.

[5] W. B. Colson, “Introduction to the Free Electron Laser,” PH 4858 Class Notes: Naval Postgraduate School. Monterey, CA: 2009.

[6] F. Horst, “FEL_principle.png,” [Online], Available: http://commons.wikimedia.org/wiki/File:FEL_principle.png (accessed 18 Jan 2010).

[7] “ONR Free Electron Laser,” [Online], Available: www.onr.navy.mil/en/Media-Center/Fact-Sheets/Free-Electron-Laser.aspx (accessed 15 Apr 2010).

[8] Vitae – Prof. Bill Colson. [Online]. Available: http://www.nps.edu/Academics/GSEAS/Physics/faculty.html (accessed 15 Apr 2010).

[9] S. T. Thornton, A. Rex. *Modern Physics for scientists and engineers, 3rd ed.* Thompson, Brooks/Cole, 2006, pp. 104–105.

[10] University of Virginia, Department of Astronomy: http://www.astro.virginia.edu/class/oconnell/astr1230/im/photoelectric-effect-2.jpg (accessed 10 Mar 2010).

[11] O. W. Richardson, *The Emission of Electricity From Hot Bodies*, 2nd ed., Longmans, Green and Co., London. [Online] Available: http://books.google.com/books (accessed 17 Apr 2010).

[12] “Dispenser Cathode Properties,” Spectra-Mat Inc. Technical Bulletin, TB-105 [Online]. Available:www.spectramat.com (accessed 14 Mar 2010).

[13] K. H. Spangenberg, *Vacuum Tubes.* Edited by F.E. Terman. New York, NY: McGraw Hill Book Company, Inc., 1948.

[14] W. Colson, et al., “Free Electron Laser” Class lecture PH4055, Naval Postgraduate School, Monterey, CA, Oct 2009.

[15] V. Vlahos, et al. “Ab initio investigation of the surface properties of dispenser B-type and scandate thermionic emission cathodes.” *Applied Physics Letters*, vol 94, no. 18 (May 2009).

[16] J. L. Cronin, “Modern Dispenser Cathodes.” *IEEE Proceedings* 128, no. 1 (Feb 1981).

[17] J. M. Roquais, et al. “Barium Depletion study on impregnated cathodes and lifetime prediction.” *Applied Surface Science,* vol 215, no. 1-4 (May 2003): 5–17.

[18] S. D. Kovaleski, “Life Model of Hollow Cathodes Using a Barium Calcium Aluminate Impregnated Tungsten Emitter.” Technical Publication, QSS Group, for NASA/CR-2001-211290, 2001.

[19] L. R. Falce, “Dispenser Cathodes: The Current State of the Technology.” *International Electon Devices Meeting 1983. Technical Digest.* Wash, DC: [Online], 1983. 448–51.

[20] E. J. Montgomery, “Characterization of Quantum Efficiency and Robustness of Cesium-based Photocathodes” PhD Thesis, Department of Electrical and Computer Engineering, University of Maryland, Baltimore: [Online], 2010.

[21] CPI Inc. *CPI Electron Gun Activation Schedule*, Communications Power Industry, Palo Alto, Technical Bulletin: [Online], 1999.

[22] J. L. Davidson, W. P. Kang, and A. Wisitsora-At. "Diamond Field Emission Devices." *Diamond and Related Materials* (Elsevier), 2003: 429–433.

[23] E. J. Montgomery, “Characterization of Quantum Efficiency and Robustness of Cesium-based Photocathodes” PhD Thesis, Department of Electrical and Computer Engineering, University of Maryland, Baltimore: [Online], 2010.

[24] J. H. Han, et al. “Dark Current and Multipacting in the Photocathode RF Guns at Pitz.” *Proceedings of 2005 Particle Accelerator Conference.* Knoxville: [Online], 2005. 895–97.

[25] W. E. Nexsen and W. C. Turner. “Poisoning Studies of an osmium-coated dispenser cathode.” *Journal of Applied Physics* (American Institute of Physics) 68, no. 1 (Jul 1990): 298–303.

[26] F. Bieniosek, D. Baca, W. Greenway, M. Leitner, and J.W. Kwan, *Comments on cathode contaminants and the LBNL test stand.* Lawrence Berkeley National Laboratory, Berkeley: [Online], 2006.

[27] R. W. Springer and T. W. Haas, “Auger-Electron Spectroscopy Study of Cathode Surfaces During Activation and Poisoning .1. Barium-on-Oxygen-on Tungsten Dispenser Cathode.” *Journal of Applied Physics* (Amer Inst Physics) 45, no. 12 (1974): 5260–5263.

[28] V. Miltchev, et al., "Measurements of the Thermal Emittance for Cesium Telluride Photocathodes at PITZ." *Proceedings of the 27th International Free Electron Laser Conference.* Stanford: [Online], 2005.

[29] S. D. Kovaleski, "Life Model of Hollow Cathodes Using a Barium Calcium Aluminate Impregnated Tungsten Emitter." Technical Publication, QSS Group, for NASA/CR-2001-211290, 2001.

[30] F. M. Bieniosek, et al.. *DARHT 2 kA Cathode Development.* Accelerator Fusion Research Division, Ernest Orlando Lawrence Berkeley National Laboratory, Berkeley: US Department of Energy, 2009, 8, 34–35.

[31] W. H. Kohl, *Handbook of Materials and Techniques for Vacuum Devices*, American Institute of Physics, 1995 (reprint).

[32] Formula of Hydrate Lab, [Online] http://chem.lapeer.org/Chem1Docs/HydrateLab2.html (accessed 02 Nov 2009).

[33] “Guidelines for Processing of Dispenser Cathodes,” Spectra-Mat Inc. Technical Bulletin, TB-147 [Online]. Available:www.spectramat.com (accessed 11 Nov 2009).

[34] B. E. Newnam, "Free-Electron Laser Sources of Extreme Ultraviolet Radiation and their Vacuum Requirements." *Vacuum Design of Advanced Synchrotron Light Sources.* Chicago: Argonne National Laboratory, 1990.

[35] H. Padamsee, “The Science and Technology of Superconducting Cavities for Accelerators.” *Superconducting Science and Technology* (Institute of Physics Publishing) 14 R28 (2001).

[36] B. Rusnak, “Accelerator Physics – Normal and Superconducting RF Accelerating Structures” Course notes PH4055, Naval Postgraduate School, Monterey, CA, Jul 2009.

[37] M.E. Cuneo, ”The Effects of Electrode Cleaning and Conditioning on the Performance of High-Energy, Pulsed-Power Devices." *Proceedings of 18th International Symposium on Discharges and Electrical Insulation in Vacuum.* New York: IEEE, 1998. 721–30.

[38] B. Bonin, “Field Emission and Surface Conditioning.” *Vacuum* (Pergamon-Elsevier Sci LTD) 46, (Aug–Oct 1995): 907–912.

[39] B. Rusnak, “PH4055 Homework: Normal and Superconducting RF Accelerating Structures” Homework PH4055, Naval Postgraduate School, Monterey, CA, Aug 2009.

[40] Communications Power Industry Inc. *CPI Electron Gun Activation Schedule*. Palo Alto, Technical Bulletin: [Online], 1999.

[41] Operating Manual and Programming Reference: Models RGA100, RGA200, and RGA300 Residual Gas Analyzer, rev. 1.4, Stanford Research Systems [Online]. Available:www.thinksrs.com/downloads/PDFs/Manuals/RGAm.pdf [accessed 14 Nov 2009].

[42] Hiden Analytical. “How a Residual Gas Analyzer works” [Online]. Available: www.hidenanalytical.com [accessed 26 Mar 2010].

[43] Stanford Research Systems. "Hot vs. Cold Ionization Gauges." Available: http://www.thinksrs.com/downloads/PDFs/ApplicationNotes/IG1hotapp.pdf [accessed 12 Jan 2010].

[44] Roughing pump. [Online]. Available: http://en.wikipedia.org/wiki/Roughing_pump [accessed 14 Mar 2010].

[45] Turbomolecular Pump. [Online]. Available: http://en.wikipedia.org/wiki/Turbomolecular_pump [accessed 14 Mar 2010].

[46] Turbomolecular Pump schematic. [Online]. Available:
http://en.wikipedia.org/wiki/File:Cut_through_turbomolecular_pump.jpg.
http://en.wikipedia.org/wiki/File:Turbo_pump_schematic.gif.
[accessed 14 Mar 2010].

[47] Duniway Stockroom Corp. “Ion Pump Operation & Troubleshooting Guide.” *Duniway Stockroom Corp.* Sherman Rutherford. Aug 1997. Available: www.duniway.com. [accessed 23 Jan 2010].

[48] Omega Engineering. iR2 SUPERMETER Ultra-High Performance 2-Color Ratio Fiber Optic Infrared Temperature Measurement and Control System. [Online]. Available: www.omega.com [accessed 14 Jan 2010].

[49] Spectra-Mat Inc., “Guidelines for Processing of Dispenser Cathodes,” Technical Bulletin, TB-147 [Online]. Available: www.spectramat.com [accessed 11 Nov 2009].

[50] FAR Pyrometry. “Tungsten Filament Emissivity Behavior.” [Online]. Available: http://www.pyrometry.com/farassociates_tungstenfilaments.pdf [accessed 01 Jun 2010].

[51] Communications and Power Industries. "EIMAC Planar Cathode/Grid Assemblies." [Online] Feb 7, 2006. Available: http://www.cpii.com/product.cfm/9/22/131 [accessed 15 Nov 2009].

[52] D. Janssen, et al., "First Operation of a superconducting RF-gun." *Nuclear Instruments & Methods in Physics Research A* (Elsevier), 2003: 314–317.

[53] H. Padamsee, "Accelerating Applications of RF Superconductivity – Success Stories." *IEEE Transactions on Applied Superconductivity* 15, no. 2 (Jun 2005): 2432–2439.

[54] J.W. Lewellen, et al., *ERL 2009 WG1 Summary Paper: Drive Lasers and RF Gun Operation and Challenges.* Summary Paper, Energy Recovery Linac Working Group, 2009.

[55] Inficon, “Quartz Monitor Crystals.” *Inficon – Semiconductor & Vacuum Coating Process.* 2009. Available: www.inficonquartzmonitorcrystals.com [accessed 14 Jan 2010].

[56] A Journal of Practical and Useful Vacuum Technology by Phil Danielson, [Online] Available: http://www.vacuumlab.com/Articles/VacLab23.pdf [accessed 01 May 2010].

[57] D. L. Smith, *Thin Film Depostion – Principles and Practice.* New York: McGraw Hill Inc, 1995.

[58] *Chemical Quantities – The Mole.* Available: http://www.eol.ucar.edu/~beaton/ChemWeb/labs/molelabs.html. [accessed 03 May 2010].

[59] Phone conversation between Inficon tech support and author, 03 May 2010.

[60] E. J. Montgomery, e-mail message to author, 25 Jan 2010.

[61] E. J. Montgomery, e-mail message to author, 11 May 2010.

[62] E. J. Montgomery, e-mail message to author, 15 Apr 2010.

[63] M. Szilagyi, “Model for Describing Emission Characteristics of Electron-Beam Evaporation Sources.” *Electrocomponent Science and Technology* 6 (1979): 9–12.

[64] T. Higuchi, O. Nakamura, S. Matsumoto, et al. "Pore Geometry of Dispenser Cathode Surface vs. Emission Characteristics, and Ba Recovery Characteristics after Ion Bombardment." *Applied Surface Science* (Elsevier) 146 (1999): 51–61.

INITIAL DISTRIBUTION LIST

1. Defense Technical Information Center
Ft. Belvoir, Virginia

2. Dudley Knox Library
Naval Postgraduate School
Monterey, California